DYNAMICS AND RELIABILITY OF ACCESS SYSTEM OF HIGH DENSITY MAGNETIC RECORDING

HE ZHIMIN

NATIONAL UNIVERSITY OF SINGAPORE

2006

I dedicate this dissertation to my loving family.

Name: He Zhimin
Degree: Doctor of Philosophy
Department: Mechanical Engineering
Thesis Title: Dynamics and Reliability of Access System of High Density Magnetic Recording

Abstract

To meet the continuous increase in demand for improved performances in the servo mechanical system of magnetic recording access system, several novel structures for the actuators/micro-actuators are proposed and their dynamic performances are characterized through simulation, optimization, prototyping and experimental investigations. These structures include: 1) a force coupled actuator to suppress the lateral translational vibration motion mode; 2) a flexural pivot for use in disk drive actuator to achieve a friction free and potentially cost-low design; 3) an actuator assembly with small skew actuation; and 4) a split electrodes piezoelectric suspension for dual-stage head positioning. This research also addresses the reliability evaluation and lifetime estimation of the piezoelectric actuators by proposing a probabilistic approach, i.e., *P-E-N* curve and the electric load-strength interference model. The reliability model is further extended to a two-dimensional case to take into account both electric driving voltage and temperature effects.

Keywords: magnetic recording, dynamics, access system, piezoelectric actuators, probability, reliability

DYNAMICS AND RELIABILITY OF ACCESS SYSTEM OF HIGH DENSITY MAGNETIC RECORDING

HE ZHIMIN
(M. Eng. NUS)

A THESIS SUBMITTED

FOR THE DEGREE OF DOCTOR OF PHILOSOPHY

DEPARTMENT OF MECHANICAL ENGINEERING

NATIONAL UNIVERSITY OF SINGAPORE

2006

Acknowledgement

The author would like to express his sincere and heart-felt gratitude to his project supervisor, Associate Professor Loh Han Tong from the Department of Mechanical Engineering for his acceptance of the project proposal, his encouragement, support and helps to the author's study, and his invaluable guidance and advice during the course of the research and his amendments on the thesis.

The author is deeply grateful to Associate Professor Xie Min from the Department of Industrial and Systems Engineering, for offering his help voluntarily to the author in the research. His guidance in the overall organization of the dissertation and co-research on the reliability of piezoelectric actuators are sincerely appreciated.

The thanks are extended to Dr. Guo Guoxiao and Dr. Ong Eng Hong from A*Star Data Storage Institute for their support and understanding about the author's research. Appreciation is also given to Mr. Zou Xiaoxin from A*Star, Data Storage Institute for his help in debugging the Matlab programs.

The collaborations from the author's former colleagues, Drs, Lin Huai and Li Qing Hua on the development of force coupled actuator, Ms. Qian Hua on the design of flexural pivot, Dr. Wu Daowei on the control implementation of flexural pivot assembly, Mr. Guo Wei on the development of the split-electrodes piezoelectric actuators are acknowledged.

Finally, the author would thank his wife, Wang Yun for her love, understanding and continuous support through the whole graduate study.

Table of Contents

Summary

This investigation on dynamics and reliability of magnetic recording access systems is motivated by the demand for improved disk drive dynamic systems and the application of secondary stage micro-actuation mechanism in magnetic recording servo mechanical systems. The dynamic performance of servo mechanical systems determines the servo bandwidth and thus the head positioning accuracy that the systems can achieve. The magnetic recording capacity, i.e., areal density increases continuously, so is the track density, which is measured in track per inch (TPI). To satisfy the constantly increased head positioning accuracy, an improved and reliable servo mechanical system is highly desired.

This research investigates the dynamic performance of several novel designs of disk drive head actuator assembly. These designs are proposed to improve the magnetic recording servo mechanical systems from several aspects. The designs include: 1) a force coupled actuator assembly to suppress the disk drive lateral translational vibration mode; 2) a flexural pivot for use in disk drive actuator to achieve a friction free and potentially cost-low design for disk drives; 3) an actuator assembly with small skew actuation to reduce/eliminate the effects of head skew to achievable track density; and 4) a split electrodes piezoelectric suspension for dual-stage head positioning. By the design, simulation, optimization, prototyping, and experimental investigation of these structures, the numerical (finite element modeling) and experimental approaches are described to characterize the dynamic performance of the actuator assembly and pivot bearing system. The force coupled actuator assembly significantly suppresses the actuator lateral translational vibration mode and enhances the first dominant resonant mode, which affects the head positioning accuracy of a disk

drive servo system. The dynamic performance of the flexural pivot is revealed and compared with a conventional ball bearing system. An optimized actuator assembly with absolute small skew actuation is developed and its dynamic performance is evaluated. The analytical, numerical and experimental approaches are employed to characterize the split electrodes piezoelectric actuator and suspensions. An optimized piezoelectric suspension for disk drive dual-stage head positioning system is proposed.

Piezoelectric micro-actuators are being used in disk drive dual-stage head positioning system. These actuators will inevitably experience the repeated load in their daily operation. The reliability and lifetime are the concern for engineers and scientists. This research addresses the reliability and lifetime of the piezoelectric micro-actuators, and proposes a probability approach for reliability evaluation and lifetime estimation of piezoelectric micro-actuator. Based on the lifetime degradation mechanism of piezoelectric actuators and probability theory, the *E-N* curve and *P-E-N* curve are proposed to describe the relationship among the electric strength and lifetime with corresponding to a certain probability. The electric load, electric strength and lifetime of piezoelectric actuators are taken as the random variables and their probability distribution are discussed. Based on the probability of the lifetime, the probability distribution of electric strength is derived. Then an electric load-strength interference model is established to model and quantify the relationship between the reliability and lifetime. The developed reliability model can be generally used to evaluate the reliability of mechatronics devices. Piezoelectric micro-actuators can be used as a typical application. This probability approach is employed to assess the reliability of a piezoelectric micro-actuator utilized in the disk drive dual-stage head positioning system.

To further address the temperature effects on the reliability and lifetime of piezoelectric micro- actuators, the reliability model is extended to a two-dimensional case. The concept of two-dimensional strength vector, which indicates both driving voltage and temperature at a specified lifetime, is proposed. The *N-E-T* surface and *P-N-E-T* surface are presented to describe the relationship among the lifetime, electric strength, and temperature corresponding to a certain probability. The probability distribution function of two-dimensional strength is determined according to the probability distribution of lifetime. The two-dimensional load-strength interference model is proposed to establish the relationship between the reliability and lifetime, taking account of the effects of both the electric load and temperature. The case study of a disk drive dual-stage head positioning systems using a piezoelectric micro-actuator demonstrates the application of this approach.

List of Tables

List of Figures

Abbreviations

DSA	dynamic signal analyzer
FEA	finite element analysis
FRF	frequency response function
GM	gain margin
HAA	head actuator assembly
HDD	hard disk drive
HGA	head gimbal assembly
ID	inner diameter
LDV	laser doppler vibrometer
MD	middle diameter
MEMS	micro-electric-mechanical system
OD	outer diameter
PES	position error signal
PID	proportional integrate-derivative
PM	phase margin
PZT	piezoelectric ceramic
R/W	read/write
TMR	track mis-registration
TPI	track per inch
VCM	voice coil motor

Nomenclatures

$b(E)$	Weibull shape parameter at a specified electric strength
$b(E, T)$	Weibull shape parameter at a specified two-dimensional strength
$[C]$	elastic constant of piezoelectric material
$[c]$	damping coefficient matrix
$\{D\}$	electric displacement of piezoelectric material
E	driving voltage, electric strength
E_3	electric field of split electrode piezoelectric actuator
E_e	electric field of piezoelectric material
$E_{\min}$	minimum value of electric strength
$E_{\max}$	maximum value of electric strength
E_Y	Young's modulus
E-N curve	curve relation between the lifetime and electric strength
(E, T)	two-dimensional strength
e	driving voltage, electric load
$[e_e]$	piezoelectric constant
(e, t)	two-dimensional load
F_A	acting force on the actuator coil
F_R	reaction force on the pivot
$[f]$	force matrix
f	frequency
f_r	undamped natural frequency of the r^{th} mode
$f(N\|E)$	probability density function of lifetime at a specified electric strength
$f(N\|E, T)$	probability density function of lifetime at a specified two-

	dimensional strength
$G_{m,k}(f)$	frequency response between point m and point k
$g(E\|N)$	probability density function of electric strength at specified lifetime
I_0	moment of inertia of the fixed end cross section of split electrodes piezoelectric actuators
I_{tilt}	mass moment of inertia in the tilt direction
J	mess moment of inertia respective to the pivot axis
K	Boltzmann's constant
k_{axial}	stiffness of the pivot bearing in the axial direction
k_{radial}	stiffness of the pivot bearing in the radial direction
k_{tilt}	stiffness of the pivot bearing in the tilt direction
$[k]$	stiffness matrix
L	distance between the pivot center and the magnetic head
L_a	arm length
L_s	suspension length
m_r	r^{th} modal mass (=1 in case of normalized mass)
$[m]$	mass matrix
N	lifetime (life cycles) of piezoelectric actuator
N_{max}	maximum value of lifetime
N_{min}	minimum value of lifetime
$N_0(E)$	minimum value of lifetime (Weibull distribution) at a specified strength
$N_a(E)$	characteristic value of lifetime (Weibull distribution) at a specified strength
$N_0(E, T)$	minimum value of lifetime (Weibull distribution) at a specified two-dimensional strength
$N_a(E, T)$	characteristic value of lifetime (Weibull distribution) at a specified two-dimensional strength

N-E-T surface	a plot of the relationship among the lifetime, electric strength and temperature
P	cumulative probability function
$P(E, T)$	two-dimensional probability distribution of strength
P-E-N curve	curve relation between the lifetime and electric strength corresponding to reliability
P-N-E-T surface	a plot of the relationship among the lifetime, electric strength and temperature with corresponding to reliability
$p_{m,r}$	element value in the excitation direction of point m in the r^{th} eigenvector
$p_{k,,r}$	element value in the excitation direction of point k in the r^{th} eigenvector
p	survival probability
R	reliability
r	coefficient of co-relation
S	nominal critical stress of material of a component or structure
T	temperature strength
t	temperature load
T_{tor}	torque
$w(e)$	probability density function of electric load
$w_e(e)$	probability density function of electric load
$w_t(t)$	probability density function of temperature load
$w(e, t)$	probability density function of two-dimensional strength
$[x]$	displacement matrix
$\phi(N)$	construction function of lifetime
$\psi(E)$	construction function of electric strength
$\mu(E)$	mean of logarithm of lifetime at a specified electric strength

$\mu(E, T)$	mean of logarithm of lifetime at a specified two-dimensional strength
$\{\sigma\}$	stress matrix of piezoelectric materials
$\sigma(E)$	standard deviation of logarithm of lifetime at a specified electric strength
$\sigma(E, T)$	standard deviation of logarithm of lifetime at a specified two dimensional strength
ε	critical strain of material of a component or structure
$\{\varepsilon\}$	strain matrix of piezoelectric material
ξ_r	modal damping ratio of the r^{th} mode
Θ	actuator rotation angle
θ_1	skew angle
β	suspension slant angle

CHAPTER 1

INTRODUCTION

1.1 The trend of magnetic recording technology

The introduction of magnetic disk drive storage devices more than three decades ago marked the beginning of a revolution in information processing. Since then, the magnetic disk drives have been more and more widely used in various kinds of computer systems and contributed as one of the most dominant factors in the dramatic growth in computer technologies. Figure 1.1 shows a general schematic of a magnetic hard disk drive. The major components in a modern rigid disk drive include: 1) device enclosure, which usually consists of a base plate and a cover to provide supports to the spindle, actuator, and electronics card; 2) spindle and motor assembly, which makes the disk rotate at a constant speed; 3) actuator assembly, which contains a voice coil motor (VCM), actuator arm, suspension and gimbal assembly to position the head to a specified track; 4) magnetic disks, and magnetic head/suspension assembly, which contain data and servo address information and 5) electronics card etc.

The progress in the disk drive industry is generally measured in terms of the significant reduction of disk size and increase of data storage densities, disk drive performance such as the faster data transfer rate and data access time, and reduction of production cost **(**Low, 1998**)**. Data storage density is measured by areal density, which is the amount of data stored with a square inch of disk media. It is calculated by the multiplication of track density TPI (track per inch) and linear density BPI (bit per inch). Areal density increases are required to satisfy the demand for ever larger

capacity hard disk drives. Since 1995, it has been growing by 60% per year on average and this trend is likely to continue, if not accelerated (Yamaguchi et al., 2000). The areal density measured in Gigabits per square inch (or Gb/in.^{2}) has reached 100 Gb/in.^{2} by the year 2004 (Kryder et al., 2004). Corresponding to the growth of the disk storage density, the size of the disk drives, however, went down rapidly from 1960's 14" diameter disk drive to 3.5", 2.5", 1.8" and even smaller than 1" disk drives.

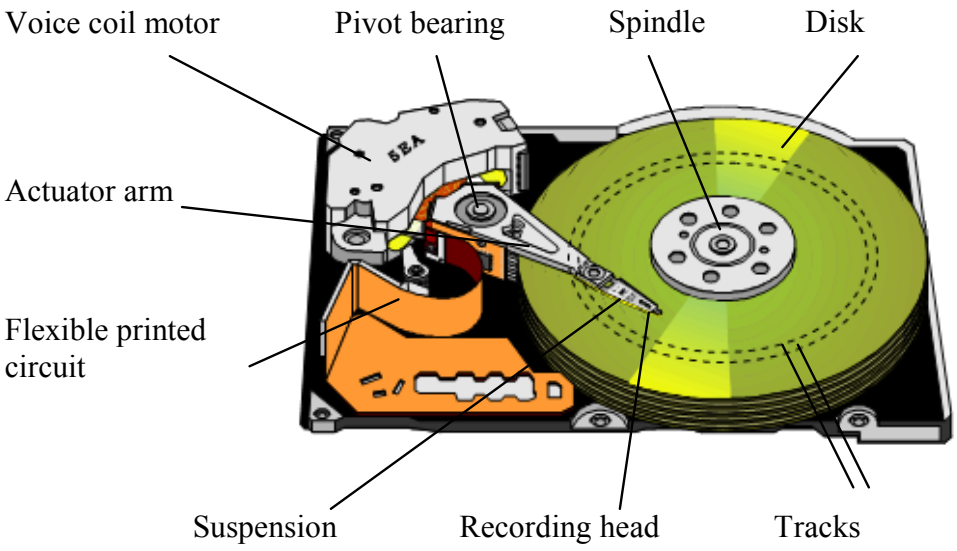

Figure 1.1: Basic structure of a magnetic disk drive.

On the other hand, in addition to the increase of the disk areal density, the performance of disk drives such as average seeking time, data transfer rate has been improved considerably as well, due to the improved technologies applied in the servo mechanical systems as well as electronics. Furthermore, due to the mass production, the cost goes down dramatically for each individual disk drive. Recently small size hard disk drives (like 0.85" and 1" micro drives) are finding new applications in commercial electronic devices, such as digital cameras, I-pod, and MP3 players. Hence, despite the challenge

of rapid development of other storage technologies such as inboard storage devices, disk drives will continue to play a significant role in the data storage industry in the foreseeable future.

1.2 The challenges in a magnetic recording access system

A magnetic recording access system (also called servo mechanical system), is an example of the technologies in a hard disk drive industry. A magnetic disk drive servo mechanical system is shown in Figure 1.2. A head positioning servomechanism is used to position the read/write heads (mounted on the actuator arm) in a disk drive over a desired track with minimum statistical deviation from the track center and re-position the heads from one track to another in minimum time. The system includes the head actuator assembly (HAA) and driver, position error signal (PES) demodulator, timing generation and position control subsystems. As the disk rotates, the recording head is capable of either writing or reading data while following a certain track.

In the magnetic disk track following mode, the servo objective is to place the read/write heads as close to the track center line as possible for reading and writing information. The main difficulty in the mode is caused by the various position error sources existing in the servo channel. The track misregistration (TMR) is used to measure the offset between the actual head position and the track center. It is the standard deviation of PES, $\pm 3\sigma$ actually. The target of servo control system is to minimize the TMR of the actuator position in the presence of noise and disturbance. Generally, this minimization results in a controller of higher bandwidth.

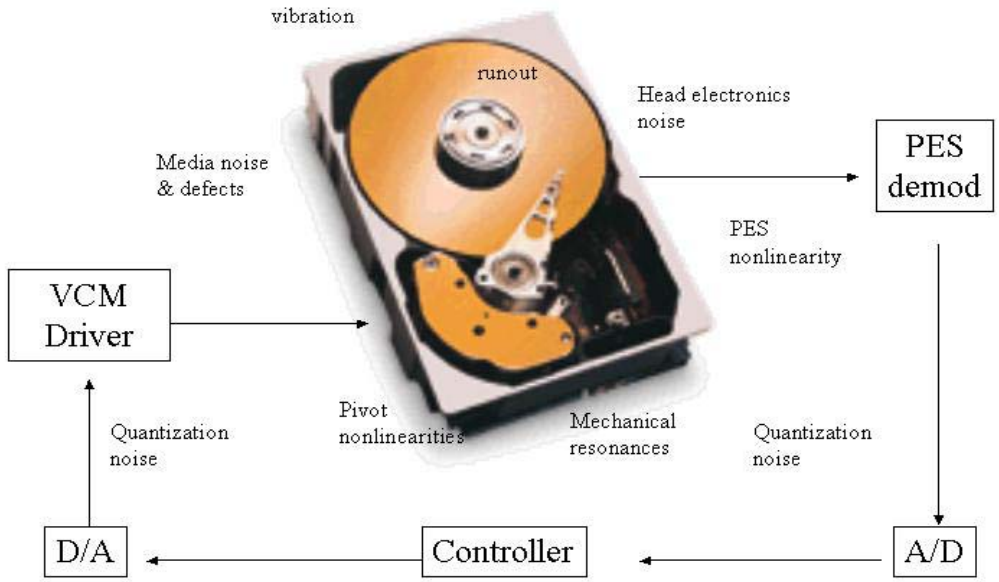

Figure 1.2: A schematic servo mechanical system of a magnetic disk drive.

As the areal density of magnetic recording is to increase to 1 Terabit/in^2 (Wood, 2000) within the next few years, the track density and bit density of magnetic disks will advance accordingly. The track density of a magnetic disk is expected to reach 500,000 to 600,000 tracks per inch (TPI) by the next few years. This places a severe demand on increased tracking accuracy with a very high precision and high bandwidth access system to bring the R/W head to the data track and maintain the head over the track under any internal and external disturbances (Fan, 1996; Guo et al., 2001). Such internal and external disturbances arise from mechanical resonance, spindle motor run-out, bearing hysteresis, flexure cable bias, defects in and inaccuracy of the media, head and servo electronics, external shock/vibration, temperature drifts, and humidity variations. Obviously, to improve the servo performance, we need to improve the mechanical system by designing high bandwidth actuators, reducing the disturbance

and vibrations such as disk fluttering, windage effects, and pivot nonlinearity (Aruga, 1996).

1.3 Motivation of the present study

1.3.1 Dynamics of disk drive access system and the improvement efforts

The areal density of magnetic recording keeps increasing. With the rapid research and development of advanced magnetic media and magnetic head technologies, the areal density of a magnetic disk drive is foreseen to reach 1 Terabit/in.^{2} within the next few years. The track density is expected to be 540,000 tracks per inch (TPI) and the track pitch about 0.047 μm (47 nm) (Wood, 2000). Tracks 47 nm wide will require exquisite control over both the lithography required to produce the head as well as the servo-mechanical system required to follow these tracks. Besides the continuous efforts in advanced control technologies (Guo, et al., 2001; Ratliff et al., 2004), the improvement in mechanical system of head actuator assembly is still the key to enhance the servo performance.

As described in the previous section, numerous research efforts have been made on the servo mechanical systems of magnetic disk drives. There still is room for improvement in systematically studying and improving the servo mechanical systems of head actuator assembly. The present study addresses the dynamics and improvement of a magnetic disk drive servo-mechanical system from several novel structure designs of the actuator assembly to enhance the performance of the system. With respect to the previous research and efforts in the improvement of disk drive access system mechanics, new design improvements are proposed. These design improvements

include 1) a novel design of disk drive actuator structure with generating a coupled force to improve the dynamic performance of the magnetic disk drive access system; 2) a flexural pivot which has the potential to be used in magnetic disk drive actuators; 3) an actuator assembly with small skew actuation to reduce the skew effects to disk drive track mis-registration; 4) a suspension structure with built-in split electrodes piezoelectric micro- actuator for dual stage micro control of the magnetic head. With the proposal of these new designs, their dynamic performances are evaluated and the structures are to be optimized.

FORCE COUPLED ACTUATOR ASSEMBLY

In order to highly suppress the lateral translational vibration mode excited by the reaction force, several designs, including moving-magnet actuators (Chen et al., 1997) and dual and single moving-coil actuators (Aruga et al., 1995; Mah et al., 1999), have been investigated. However, in these designs, the exposure of magnets in a moving magnet actuator leads to significant difficulty in the production and the assembly processes of the actuator. Therefore, we developed a moving-coil actuator with a novel design in voice coil motor (VCM) construction, which can generate a coupled force or pure torque to the actuator assembly. This seems a practical way to realize high servo bandwidth for a head positioning system.

FLEXURAL PIVOT FOR USE IN DISK DRIVE ACTUATOR

Ball bearings are currently used in hard disc drives to provide rotational mechanism for the actuator assembly. Ball bearings operate with friction and damping, causing non-linearity in the actuator response and therefore make the position control more difficult (Prater, 1995; Liu et al., 2000). Flexural bearings, on the other hand, are simpler in

structure and therefore have potential for low cost compared with the current ball bearing systems. Based on this point, we developed a flexural pivot for use in hard disk drive actuator. The dynamics of flexural pivot cum with disk drive actuator have been studied (He et al., 2003).

ACTUATOR ASSEMBLY WITH SMALL SKEW ACTUATION

Currently the utilization of the voice-coil-motor for actuating read/write head elements in magnetic hard disk drives (HDD) results in a skewed actuation, which necessitates an involved micro-jogging process and thus a complicated servo system. A large skew actuation will affect the slider's flying performance and off-track capability, causing an increase in side reading and an offset of written transitions from track center. Especially in self-servo writing and with the recent research and development in perpendicular recording, having zero skew and small skew actuation is highly desired. Therefore an effort is made to develop an actuator assembly with small skew actuation assembly and its dynamic performance has been evaluated (He, et al., 2002).

SPLIT ELECTRODES PIEZOELECTRIC SUSPENSION FOR DUAL-STAGE HEAD POSITIONING

The development of piezoelectric micro-actuators is a hot topic in developing micro-actuators for disk drive dual-stage head positioning system. Guo et al. (1998) proposed a piezoelectric suspension for use in disk drive dual-stage head positioning system. The piezoelectric suspension is actuated via a split electrodes piezoelectric micro-actuator. With the complexity of the suspension structure, which includes the suspension load beam, piezoelectric actuator, bonding material, and head gimbal assembly, analytically it cannot be determined that the proposed planar piezoelectric suspension is an optimized structure. Therefore, an optimization is performed onto the

piezoelectric suspension via finite element modeling. An optimized design is proposed in considering the static and dynamic performances.

1.3.2 Reliability of piezoelectric micro-actuators

As the actuators and micro-actuators are major components used in magnetic disk drive servo mechanical systems, these devices will inevitably bear fatigue loads during their operation. Secondary stage micro-actuators (made of MEMS, piezoelectric material and electrostatic devices etc.) show promise to be used for accurate positioning of read/write head on the disk surfaces. Of these, much more attention has been focused on the development of piezoelectric actuators because of their high resolution, fast response and high resonance frequencies.

For piezoelectric materials, quite a number of studies have addressed their fatigue and durability properties (Mall and Hsu, 2000; Mitrovic et al., 2000), environmental stabilities (Yoshikawa et al., 2000), as well as the fracture behaviors (Wang and Carman, 1998; Dausch and Hooker, 1997). However, as the material/structural fatigue is a very complicated process, the phenomena are dominated by numerous factors such as, the scatter of material properties, material processing, manufacturing, assembling and environments etc. Therefore a “fatigue reliability” approach which deals with the material/structure fatigue using probabilistic method and statistical tool has been widely practiced (Carter, 1997; Sobczyk and Spencer, 1992). In typical fatigue reliability, which deals with the mechanical fatigue and failure of a components/structure, a *P-S-N* curve or *P-*ε*-N* curve is generally used for reliability evaluation and lifetime estimation. The *P-S-N* curve or *P-*ε*-N* curve describes the relationship among the reliability, stress or strain and the number of life cycles for

particular mechanical components or structures. For miniaturized piezoelectric actuators, numerical methods can be used to compute the stress or strain of piezoelectric materials. However, experimentally it is not convenient to obtain the local stress or strain of the critical locations of piezoelectric micro-actuators. Therefore neither the *P-S-N* curve nor the *P-ε-N* curve is convenient to be used for the fatigue life estimation and reliability evaluation for piezoelectric actuators.

As piezoelectric actuators can be looked upon as typical electromechanical devices, the typical relationship between "fatigue life" and "fatigue strength" can be replaced by the relationship between "fatigue life" and "electric strength". Here, the electric strength refers to the driving voltage of piezoelectric devices. The present study proposes to incorporate the theory of mechanical fatigue reliability to electromechanical devices, specifically the piezoelectric micro-actuators, to establish reliability model for piezoelectric micro-actuators (He, et al., 2005). Based on this motivation, the *P-E-N* curve, which describes the reliability, electric driving voltage, and life cycles, is presented. A reliability model, i.e., electric load-electric strength interference model is proposed for reliability evaluation. The probability distributions of lifetime, electric strength, and electric load are discussed. A case study of piezoelectric actuator used for disk drive head positioning system demonstrates the application of this approach. The approach can also be used in general electromechanical devices.

In the practical operation of piezoelectric actuators, temperature plays a significant role in fatigue failure. In general, increasing temperature decreases the lifetime of piezoelectric micro-actuators. Also temperature change is a dominant uncertainty

among the environmental effects. In order to take into account the temperature effects in the reliability model of piezoelectric actuators, we take both electric driving voltage and temperature as the two-dimensional random variables. A *P-N-E-T* surface which describes the relationship among the reliability, lifetime, electric driving voltage, and temperature is presented. A two-dimensional reliability model, i.e., the two-dimensional load-strength interference model is established for the reliability evaluation. The case study of the piezoelectric actuator used in disk drive head positioning system can also demonstrate the application of the model (He et al., 2007).

1.4 Organization of the dissertation

There are two major parts in this dissertation. The first part presents the research methodologies in the investigation of the head actuator dynamics and the development works in improving the dynamic performances of a magnetic recording access system. The second part of the dissertation proposes and discusses the reliability models for piezoelectric micro-actuators, demonstrates the application of the proposed reliability models in the piezoelectric micro-actuators used in magnetic recording dual-stage head positioning system.

Following the thesis introduction, which is in this chapter, previous research and efforts in disk drive head actuator dynamics and the improvement work are reviewed in Chapter 2. Then the first major part, which includes four chapters in the thesis, is presented. Chapter 3 presents the research methodologies in the modeling, simulation and experimental investigation of the head actuator dynamics, as well as a proposed novel actuator structure to suppress the actuator lateral translational resonance mode.

The performances of the actuator structure are characterized. Chapter 4 describes a flexural pivot for use in hard disk drive actuators. A flexural pivot bearing, which has the potential for replacing the existing ball bearing, is proposed. Its dynamic performances are characterized and control application is implemented. Chapter 5 presents a head actuator assembly with small skew actuation. The actuator assembly is optimized with small skew actuation and its dynamic performances are evaluated. In Chapter 6, the development work of a piezoelectric suspension using a split electrodes piezoelectric actuator for disk drive dual stage head positioning system are presented. The planar structure is optimized according to the dynamic and static deflection requirement.

Part II of the dissertation includes two chapters. Chapter 7 presents a probabilistic approach to evaluate the reliability of piezoelectric actuators. The *P-E-N* curve is proposed for lifetime estimation of piezoelectric actuators. An interference model, i.e., the electric load-strength interference is established to evaluate the reliability of piezoelectric actuators. The probability distributions of lifetime, electric load, and electric strength are discussed. A case study of piezoelectric micro-actuators used in disk drive head positioning systems is used to demonstrate the applicability of the reliability model. Chapter 8 further extends the reliability model taking into account temperature effects. The *P-N-E-T* surface and a two-dimensional interference reliability model, which considers both driving voltage and temperature as the random variables, are established. The probability distribution of the two-dimensional strength (driving voltage and temperature) is derived. The case of the piezoelectric actuator used for disk drive head positioning system is employed to demonstrate the approach.

Chapter 9 makes the concluding remarks, summarizes the contributions of the work, and recommends further work pertaining to the improvement of disk drive access systems and the reliability study for piezoelectric actuators.

CHAPTER 2

REVIEW OF MECHATRONICS IN A HARD DISK DRIVE ACCESS SYSTEM

With the rapid progress of magnetic recording technologies, extensive efforts have been continuously made in magnetic recording servo mechanical systems. These include the study of head actuator dynamics, improvement in mechanical structure design and development of advanced control technologies etc. This chapter gives a review of mechanics in hard disk drive access system and previous study and efforts made related to the present research based on an extensive literature search.

2.1 Mechanical performance terms and requirements

A magnetic disk drive is basically a very compact, electronically controlled, rotary-motioned memory device. It includes a spinning disk stack and a set of read/write (R/W) magnetic recording heads positioned swiftly and accurately over the magnetic disk surfaces by a mechatronics subsystem – the head actuator assembly. The head actuator assembly utilizes a voice coil motor to move the head actuator arm over the surface of the disk platters, and a closed loop feedback system to dynamically position the heads directly over the data tracks.

The head actuator assembly needs to position the read/write head elements quickly and accurately to a specified track to satisfy the high track density and the operation requirements of a magnetic disk drive. The basic parameters that are important in the

mechanical performance include: areal density, track density, seek, latency and access system time, form factor and spindle speed etc.

Areal density

Areal density is defined as the number of bits that can be packed into each unit area on the surface of the disk. It is measured in unit of megabits per square inch (10^6 bits/in^2), or gigabits per sqaure inch (10^9 bits/in^2), and will probably be in terabits per square inch (10^{12} bits/in^2) in the next few years. Areal density is the product of track density multipled by bit or linear density on each track. Since 1997 this rate had accelerated by 100% per year.

Track density

Track density refers to tracks per inch (TPI), being one main factor that influences areal density. The achievable track density of a hard disk drive is deterimined by the servo mechanical system, i.e., the mechanical structure performance and control scheme. The principal influence of the mechanical design in the track density is the dynamic performance of the system, which determines the achievable servo bandwidth. Within the servo bandwidth, the external distrubances have to be suprressed, otherwise the disturbances will be amplified.

Seek, latency and access time

Seek time measures the amount of time required for the heads to move between tracks, while latency is the time that the drive must wait for the correct sector to come around to where the heads are waiting for it. Access time is the sum of the seek and latency time.

Form factor

Form factor is the size of hard disk drive, and is getting smaller and smaller. Currently 3.5 inch hard drives dominate the desktop computer industry, while 2.5 inch drives are the standard with mobile computers. Recently a microdrive with a one inch diameter disk and less than 0.25 inch thickness has been widely used in commercial electronics.

Spindle speed

Spindle speed describes how fast the disk rotates in terms of revolutions per minute (RPM), and high spindle speed improves both random-access and sequential performance. Current speed of 5400, and 7200 RPMs are the standard on desktop drives.

The performances described above depend principally on the electro-mechanical system and mechanical structure design. Many dynamical and mechanical issues have become challenging and critical due to the strigent requirements involving the development of future drives. Extensive research and development efforts are being made to improve the technologies used. They are reviewed in the next section.

2.2 Previous study and efforts in magnetic recording access system

2.2.1 Actuator dynamics and improvement efforts in a voice coil motor (VCM) actuator assembly

The servo mechanical system of a magnetic disk drive includes many key components such as actuator arm, head/suspension assembly, pivot bearing and voice coil motor (VCM). The servo bandwidth of a magnetic disk drive actuator is limited mainly by

the inherent mechanical resonance of the head actuator (Aruga et al., 1996; Fan et al., 1995). Many researchers have investigated the head actuator dynamics using finite element modeling and experimental modal analysis (Zeng et al., 2000; Health, 2000; Xu and Guo, 2003). Figure 2.1 shows the frequency response functions or transfer functions of read/write head of typical magnetic disk drive actuators and a high bandwidth actuator (HBX) (Mah, et al., 1999). From the figure it is noted that there are many resonant modes between 4 and 6 kHz, which correspond to the actuator rocking mode and the lateral translational vibration mode of the actuator. The lateral translational vibration mode is primarily caused by the flexibility of the pivot assembly and the mass of head actuator assembly (HAA) (Mah et al., 1999), and is the main factor that limits the servo bandwidth.

Some researchers have recently made efforts to improve the head actuator assembly dynamics, i.e., to increase the resonance frequency and reduce the resonance amplitude, thus to achieve a high servo bandwidth. One approach is to design a new kind of head actuator, which is driven by a coupled force (Chen et al., 1997; Mah et al., 1999). Therefore, only a pure torque is generated to the actuator pivot thus generating no reaction force. It is proven that this type of actuator can achieve a high resonance frequency of in-plane vibration mode, as shown in Figure 2.1 (Mah et al., 1999; Lin et al., 2001). However, owing to cost issues, these designs are far from commercialization. The second approach is to add passive damping into the head actuator assembly (Liang et al., 1999; Zeng et al., 2000). It has been shown experimentally that the dynamics of the head actuator are improved greatly. The third approach is to introduce an active damping system (Huang et al., 2001) and an instrumented suspension (Huang et al., 1999) to sense the resonance modes of actuator

arm and suspensions and then a feed back control loop is designed to eliminate the resonance amplitude.

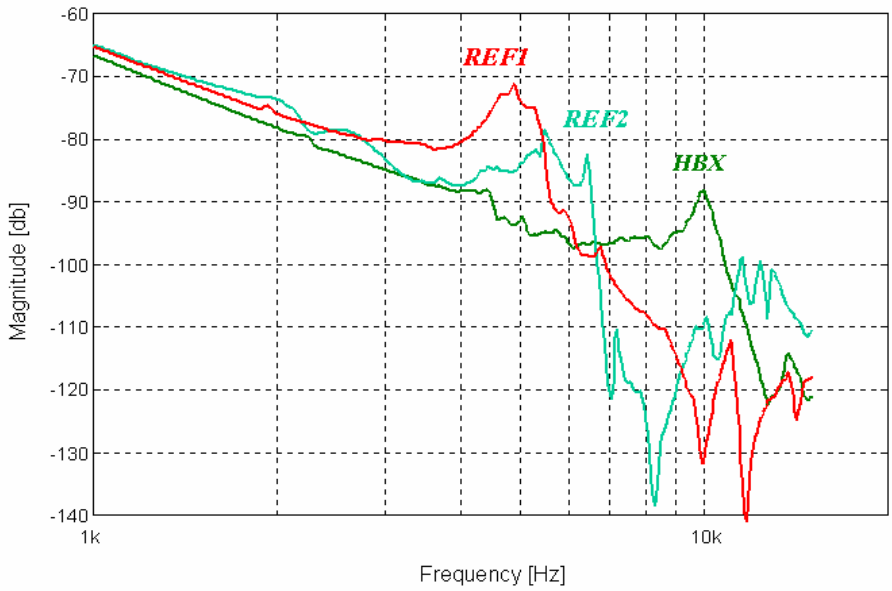

Figure 2.1: Frequency response functions of conventional actuators and high bandwidth actuator (HBX).

In addition to the above efforts to enhance magnetic disk drive actuator dynamic performance to improve the disk drive servo performance, a lot of research has been performed on other issues of disk drive head actuator assembly. Those include disk drive head actuator assembly pivot friction modeling (Liu et al., 2000), shock resistant capability evaluation and shock prevention (Lee et al., 2001) head skew effects to disk drive servo (Liu et al., 1996; Wei et al., 1998 and 1999) and the effects of disk drive actuator arm to the air flow pattern due to disk rotating and thus the contribution to head track mis-registration (TMR) (Imai et al., 1997; Ong et al., 2000).

2.2.2 Magnetic disk drive pivot friction and the effects on head mis-registration (TMR)

In the magnetic disk drive application, the actuator is supported by a pivot cartridge consisting of two preloaded ball bearings. Friction torque hysteresis exists in the bearings, and it is believed to adversely impact the actuator performance and becomes a hindrance to achieve the desirable actuator control with high track densities. The hysteresis torque behavior of rolling bearings has been investigated by Dahl (1968). The drive operates under two conditions, track seeking and track following. Most of the work thus far has concentrated on the track-seek mode. Eddy et al., (1997) showed the effect of friction of pivot bearing during track seeking and compensated for it based on the Dahl friction model. Takaishi et al. (1996) showed the effect of pivot bearing in the form of the transfer function and concluded that it made the settling characteristics worse. The same experiment was performed by Hurst et al. (1997), in which low frequency gain loss caused by ball bearing friction torque was illustrated. The effects of friction torque on TMR in track following was investigated by Liu et al. (2000) who proved that the friction torque of the pivot bearing contributes to track mis-registration (TMR).

2.2.3 Study of shock-resistance of head actuator assembly

As a magnetic disk drive becomes widely used in portable environments, the most important requirement for disk drive design is its reliability under severe environmental condition, especially, resistance to mechanical shock. Some previous researchers (Lee et al., 2001; Jayson et al., 2003a, 2003b) have investigated the head slap phenomenon analytically, numerically and experimentally. Several insights into the dynamic behavior due to shock of the head actuator assembly and the disk have

been observed. Head lift-off depended on dynamic behavior of the suspension at non-operating condition. On the other hand, the dynamic response of the head was controlled by shock response of the disk when the head was at the middle or outer diameter of the disk. The suspension geometry design was found to be very important to improve the shock performance of head disk interface. In Lee's work (2001) a theoretical model was built for predicting the shock behavior of the suspension in order to get a shock-resistant improved design. It also indicates that the shock performance cannot be fully determined without evaluating the system as a whole.

2.2.4 Head skew effects on magnetic disk drive track mis-registration (TMR)

Currently, the utilization of the voice-coil-motor (VCM) for actuating read/write head elements in magnetic hard disk drives results in a skewed actuation. A skew angle is geometrically defined as the angle between slider's longitudinal axis and track direction. The head skew significantly affects the magnetic disk drive servo performance, thus contributing to head track mis-registration (TMR). The studies by Hu et al., (1997); Liu and Soh, (1996); and Wei et al., (1997), (1998) showed that the increased skew actuation affects the head flight performance, off-track capability and signal to noise ratio. This complicates the position error signal calibration process on the hard disk drive servo loop, as well as the self-servo track writing process. In a recent development in perpendicular magnetic recording, an involved read sensor pole trimming is necessary to relax the side reading effect due to skew angle variation (Wood, 2001; Jayson et al., 2003a, 2003b).

IBM proposed a parallel flexural in-line actuator for magnetic recording disk drives which has a small skew actuation (Chainer, et al., 1991). However, this design exhibits

a resonance frequency about 1.5 kHz. It is much lower than 4~6 kHz, the resonance frequency of the existing actuator assembly with a ball bearing structure. The low resonance frequency limits the achievable servo bandwidth. Toshiba researchers proposed a magnetic disk drive with an increased actuator arm length to achieve a small skew angle change (US Patent 6,021,024, 2000). But its dynamic performance has not been revealed publicly.

2.2.5 Effects of head actuator assembly on the airflow of magnetic disk and track mis-registration

The effects of airflow in hard disk drives (HDDs) has been an important area of research, as inhomogeneities in flow in a typical hard disk drive can give rise to impaired data transmission. Some of the research on airflow in HDDs carried out previously involved co-rotating disks in a cylindrical enclosure (Abrahamson et al., 1989; Chang et al., 1990). In other studies, a dummy obstruction to simulate the existence of the actuator in hard disk drives was included (Schuler et al., 1990; Tzeng et al., 1991). Usry et al., (1990) is one of those who studied the effect of rotary arms on co-rotating disk flow. Recently, much effort has also been made to curb disk vibration by manipulating the airflow (Girard et al., 1995; Bittner and Shen, 1999; Imai et al., 1997). Ong et al., (2000) have attempted to reduce the track mis-registration (TMR) of hard disk drives by modifying the actuator arms. A systematic way of estimating the optimal arm length is presented and two unconventional cross sections are suggested for the actuator arm of two actuators, with both actuators capable of achieving high bandwidth with the optimal arm length.

2.2.6 Development of secondary stage micro-actuators

In addition to the effort to push the VCM actuator servo bandwidth higher while increasing the resonance frequency of the actuator in plane lateral mode and reducing the vibration amplitude, the noise and disturbance in the servo loop, another promising solution is to use a dual-stage servo control system, which includes a secondary-stage micro-actuator. That is, the VCM acts as the primary stage actuator and a micro-actuator as the secondary stage actuator to provide fine tracking of the read/write element. A push-pull piezoelectric micro-actuator developed by Nakamura, et al., (2001) is shown in Figure 2.2. The objective to utilize a micro actuator in disk drive servo mechanical system is to push the close-loop servo bandwidth much higher than in a single stage VCM actuator system. Since the bandwidth of the secondary micro-actuator is generally high, it would be easier to extend the servo bandwidth and maintain a better TMR with this approach than with the single stage approach. Obviously, a secondary micro-actuator must have a high natural frequency, adequate stroke output capability, easy controllability, and a simple structure.

From the viewpoint of the actuation mechanism, there are three main categories of secondary micro-actuators: piezoelectric, electromagnetic (Koganezawa et al., 1996; Temesvary et al., 1995; Takaishi et al., 1996) and electrostatic (Fan et al., 1999; Chen et al., 2001; Kim and Chun, 2001). The excellent features that a piezoelectric micro-actuator possesses, such as being small in size, simple in structure, high in frequency response and yet capable of producing sufficient displacement with a reasonable low drive voltage, make it one of the best options as secondary actuator (Aruga et al., 1996; He, et al., 1999; Wang et al., 2001; Kuwajima et al., 2002; Budinger et al., 2004). The piezoelectric micro-actuators can be mounted at various locations, such as on the arm

(Takaishi et al., 1996), suspension (Guo et al., 1998; Niu et al., 2000), and between the suspension and the slider (Hirano et al., 1999).

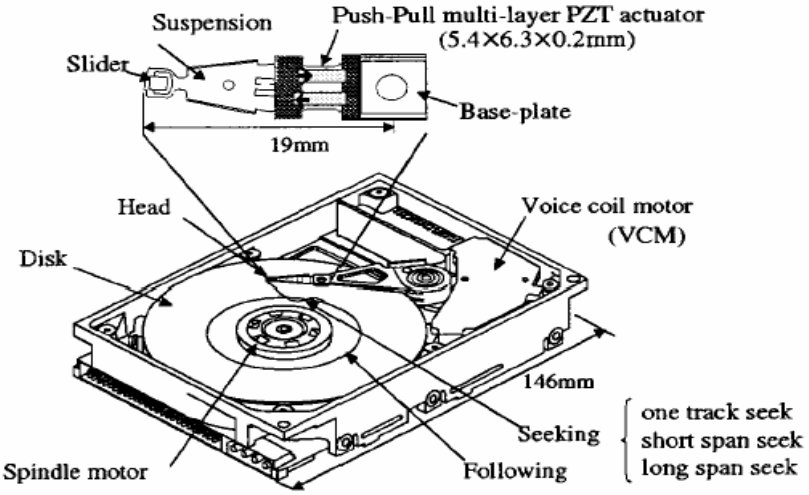

Figure 2.2: A push-pull multi-layer piezoelectric micro-actuator for dual stage servo system (Nakamura, et al., 2001).

2.3 Reliability of piezoelectric micro-actuators

With the application of piezoelectric micro-actuators in disk drive dual stage servo positioning system, the reliability of piezoelectric micro-actuators will become of concern to scientists and engineers. In the fine tracking operation, the piezoelectric actuator will experience repeated loads during its operation. The fatigue failure and the life cycles issues become important. So far, there is existing research on the fatigue behavior and mechanism of the piezoelectric actuators and the improvement methods. In general, the research can be categorized into life cycle of the multi-layer ceramic actuator (Thongrueng, et al., 1998; Nakamura, et al., 2001), actuator environmental stability (Yoshikawa and Farrell, 2000), and fracture/crack growth of piezoelectric

ceramics (Mall and Hsu, 2000; Mitrovic, et al., 2000; Wang and Carman, 1998; Dausch and Hooker, 1997).

Probabilistic reliability analysis has been widely practiced in the fatigue design and life cycles estimation of mechanical components and structures due to the scatter of material properties and environment uncertainties (**S**obczyk K, and Spencer J.B.F. 1992). According to previous research (Nakamura, et al., 2001; Thongrueng, et al., 1998; Yoshikawa and Farrell, 2000), the performances and lifetime of piezoelectric actuators are sensitive to the operation environment and external mechanical and electric loads. Experimental data shows the variation and diversity of the material properties and the actuator performance. Therefore, it is also necessary to introduce probabilistic approaches and statistical tools in the reliability evaluation of piezoelectric micro-actuators. Further, the reliability model based on probabilistic approaches and statistical tools may not be limited to the piezoelectric actuators in the micro positioning system in a magnetic recording disk drive. It can be extended to other piezoelectric actuators/sensors and mechatronics devices.

2.4 Summary

It is obvious that the vibration of the head actuator assembly is one of major mechanical problems that affect the performance of the hard disk drives, and it is essential to suppress the vibration for achieving high accuracy and fast head positioning. The lateral translational vibration mode is one of the most significant modes that limit the servo bandwidth. Pivot friction and head skew actuation have adverse effects on the head positioning accuracy and limit the performance of access

system. A dual-stage micro-actuator can be utilized in access system to increase the servo bandwidth. However, the designed micro-actuator must have a satisfactory dynamic performance and static deflection at a specified power input. The problems above motivate the present research.

As piezoelectric micro-actuators are experiencing fatigue load in their operations in the dual-stage micro positioning system in a magnetic disk drive, lifetime issues are becoming of increasing importance. The fatigue performance of piezoelectric micro-actuators is also sensitive to external environments and variation of material properties. Therefore, using probabilistic methods and statistical tools is necessary in the reliability analysis of piezoelectric micro-actuators. This motivates the author's research in proposing a probabilistic reliability model in piezoelectric actuators.

PART I

DYNAMICS OF ACCESS SYSTEM OF A MAGNETIC DISK DRIVE

CHAPTER 3

MODELING OF ACTUATOR MECHANICS AND DEVELOPMENT OF AN ACTUATOR WITH FORCE COUPLED ACTUATION

This chapter proposes the basic mechanics models and dynamic characterization approaches of a magnetic disk drive access system. It presents a novel high bandwidth actuator assembly for the applications in high track density magnetic recording in hard disk drives. This novel design in voice coil motor (VCM) construction, with flat moving-coil, is as simple as a conventional one. The VCM generates a coupled force or a pure torque to the actuator assembly and therefore, the translational resonance mode of the actuator in the tracking direction can be suppressed. This results in a significant improvement in actuator dynamic performance and thus increases the servo bandwidth of hard disk drives. A 3-dimensional finite element analysis (FEA) is conducted to predict the dynamic performance. The design has been prototyped and experimentally investigated. Studies show that the lateral translational vibration mode, which limits the servo bandwidth in a conventional actuator, has been substantially suppressed.

3.1 Introduction of a magnetic disk drive actuator

Figure 3.1 shows the basic structure of a magnetic disk drive. In magnetic recording, digital information is recorded in concentric tracks on rotation disks by means of miniaturized read/write (R/W) heads. R/W heads are mounted on self-lubricated flying sliders. These sliders are connected to stainless-steel suspensions that are in turn

connected to a guide arm. In magnetic disk drives, the guide arm is rotated by a voice coil motor with a pivot bearing support. These setups allow cross track seeking and track following of the R/W heads.

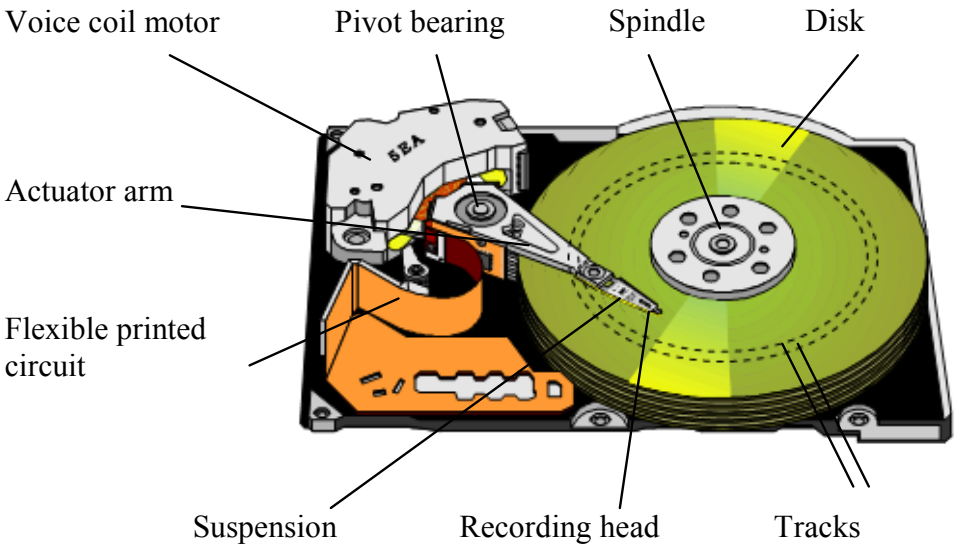

Figure 3.1: Basic structure of a magnetic disk drive.

The areal density for magnetic recording media is expected to reach 1 Terabits/in^2, corresponding to the track density 500~600 kTPI in next few years. To realize such a high track density, a sufficiently high servo bandwidth of a head positioning system is needed. The problem preventing a high servo bandwidth is the mechanical resonance of actuator and head assemblies. Researchers and designers for a head positioning system hope to develop a highly improved actuator system for advanced single-stage positioning in order to support as high a track density as possible, as this is cost effective and reliable to manufacturing and assembly. Much effort has been made to increase the servo bandwidth of the magnetic recording head positioning system such as introducing secondary stage servo systems, improvement in control scheme and applying active and passive damping to actuator structure to reduce the vibration

amplitude. However, an obvious way is to increase the mechanical resonance frequency of a conventional single stage actuator (Aruga et al., 1996; Chen et al., 1997). For a VCM-based actuator, to produce a coupled force or pure torque is an effective approach to increase the mechanical bandwidth (Chen et al., 1997; Mah et al., 1999).

Mid-band resonance modes inherent in conventional actuators have significantly limited the servo bandwidth (about 20% of the primary resonance frequency of an actuator) and make R/W head tracking systems incapable of meeting the stringent demands for high TPI recording. Among these unexpected mid-band resonance frequencies, the lateral translational resonance mode, caused primarily by the elasticity of the pivot bearing and the mass of the movable parts of the actuator, is the major factor to limit the servo bandwidth of head positioning system. For the conventional actuators, the lateral translational mode is usually located at a mid-band frequency of about 3-5 kHz. The first in-plane bending mode is another major factor that affects the servo bandwidth, which is usually located at about 7-10 kHz. The servo bandwidth of the servo system supported by a conventional actuator assembly is substantially limited due to the lower frequency of the lateral translational vibration mode. To significantly reduce or completely eliminate the lateral translational mode is therefore the key to increase the servo bandwidth of the head positioning systems.

An effort in developing a high bandwidth planar moving-coil actuator with novel configurations in coil and magnets to produce coupled force and pure torque has been made (Lin et al., 2001). The actuator is constructed as a simple moving elongate flat coil and is as simple as a conventional moving-coil actuator used by hard disk drive

manufacturers today. The study shows that the unexpected mid-band lateral translational resonance due to pivot bearing and shaft has been substantially suppressed using this design. This leads to the achievement of the primary resonance frequency of about 11 kHz and up to 15 kHz if material of high stiffness is used to make the E-blocks.

3.2 Basic mechanics of a magnetic disk drive actuator

Figure 3.2 shows a conventional rotary actuator assembly with one flat coil. This type of rotary actuator is widely used in recent magnetic disk drives. When positioning the read/write head element, the actuator is actuated by a servo system through injecting a current to the voice coil motor (VCM) to perform a track-to-track seek or to follow a registered track on a disk. The recording head continuously reads a prewritten servo pattern on the track for close-loop feed back positioning control of the read/write head. It is observed that the driving force (F_A) produced by the conventional voice coil motor (VCM) has a large component in the cross-tracking (lateral) direction. This generates a substantial reaction force (F_R) on the pivot bearing assembly.

The structural (mechanical) resonance modes of the actuator impact the performance of the servo. Conventional rotary actuators have two mechanical resonance modes, which affect the servo performance significantly. The two resonance modes are shown in Figure 3.3 (Li, 1997). One is elasticity bending vibration mode (at about 7~10 kHz). The other is the lateral translational mode (at about 3~5 kHz), which is mainly influenced by the mass of the actuator's moving parts and spring constants of the support pivot bearing. The corresponding frequency response is shown in Figure 3.4. It

is observed that there are two peaks, corresponding to the lateral translational mode and the first lateral in-plane elastic bending mode, in the frequency response characteristics of the conventional actuator. Usually this lateral translational mode decides the low and middle band resonance frequencies in the seek direction (3~5 kHz) for the 3.5-inch drive. The reaction force (F_R) can potentially excite the lateral translational resonance mode in the cross-tracking direction, impacting the accurate tracking of head positioning system.

The existing mechanical resonance modes can cause degradation of stability in the disk drive servo loop and lead to poor noise rejection, resulting in an increased track mis-registration (TMR) of the magnetic head. One possible solution to the problem would be to push the resonance mode of the actuator as far right in the frequency domain as possible. This will reduce the possibility of the resonance mode interfering with servo loop dynamics. The other possibility is to re-configure the activation force of the actuator such that these resonance modes are not excited. Both concepts are applied towards creating an actuator with high bandwidth.

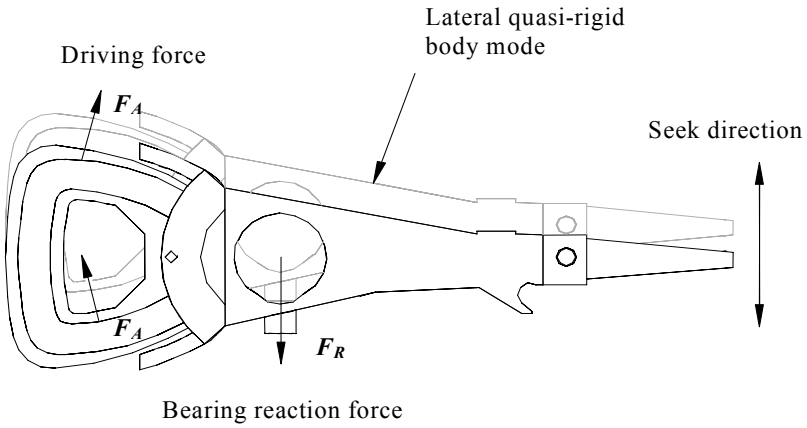

Figure 3.2: A conventional rotary actuator.

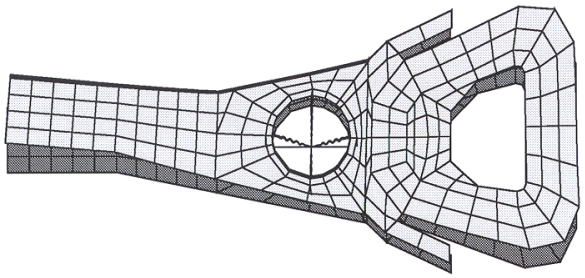

(a)

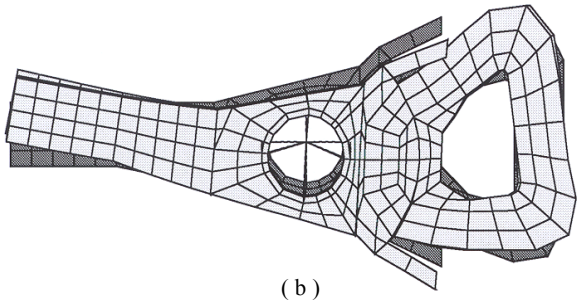

(b)

Figure 3.3: The mode shapes of the two typical resonance modes of a conventional actuator. (a) lateral translational mode at 4.3 kHz. (b) lateral in-plane bending mode at 8.6 kHz.

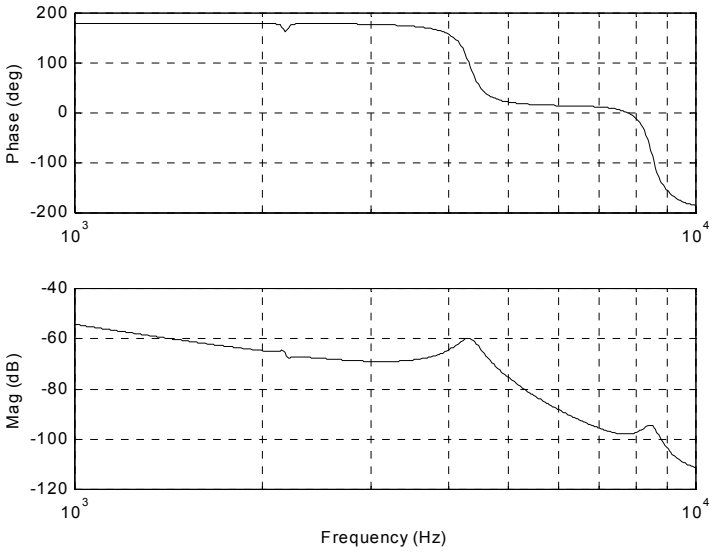

Figure 3.4: Frequency response of a conventional actuator.

A mechanics model for the actuator for disk drive actuator structure is shown in Figure 3.5. If the longitudinal vibration (which is not in the seek direction) is ignored, the

model can be further simplified as shown in Figure 3.6. The model includes the pivot bearing lateral translational mode and actuator arm lateral bending resonance modes. The equation of motion can be described as follows.

$$[m]\ddot{x} + [c]\dot{x} + [k]x = [f] \tag{3.1}$$

where,

$$[x]=\begin{Bmatrix} x_1 \\ x_2 \\ \theta \end{Bmatrix},\quad [m]=\begin{Bmatrix} m_1 & 0 & 0 \\ 0 & m_2 & 0 \\ 0 & 0 & J \end{Bmatrix},\quad [k]=\begin{Bmatrix} k_1+k_2 & -k_2 & -k_2 r_2 \\ & k_2 & k_2 r_2 \\ sym & & k_2 r_2 \end{Bmatrix},\quad [f]=\begin{Bmatrix} F \\ 0 \\ T_{tor} \end{Bmatrix},\quad T_{tor}=F r_1, \tag{3.2}$$

m_1 stands for the actuator arm mass, m_2 stands for the moving mass due to the actuator arm bending mode, J stands for the mass moment of inertia respective to the pivot axis. k_1 stands for the bearing radial stiffness and k_2 is an assumed stiffness linking the actuator arm and the moving portion due to bending, and $[c]$ is the damping coefficient.

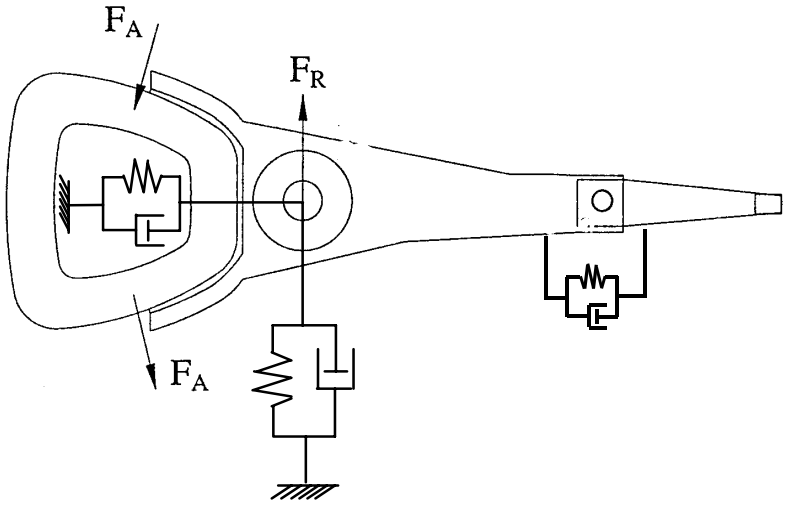

Figure 3.5: Basic mechanics of a conventional disk drive actuator.

If we make an actuator with a wider arm structure, the actuator will be heavier and more rigid. We can obtain higher in-plane elasticity mode frequencies. However, this decreases the resonance frequency of the lateral translational mode. As long as the

pivot bearing is used here, this lateral translational mode cannot be eliminated. Therefore it is meaningful to develop disk drive actuator assembly to suppress the lateral translational mode.

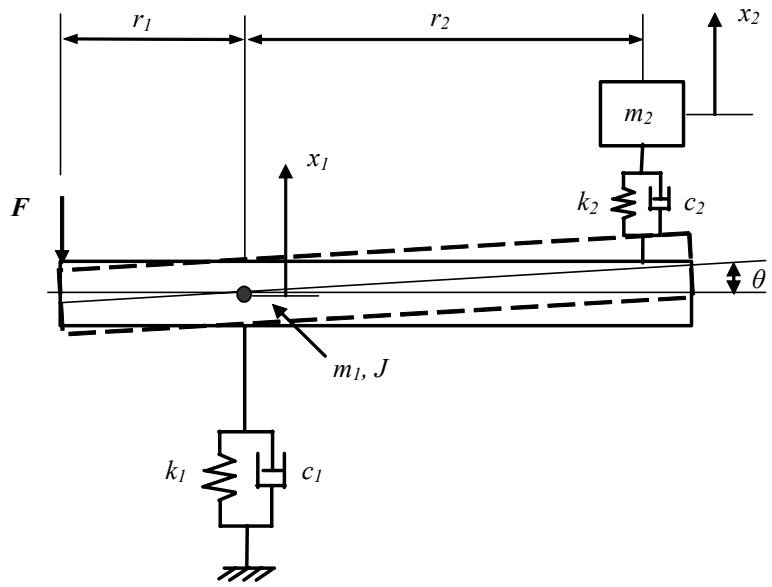

Figure 3.6: A simplified model of a conventional disk drive actuator.

3.3 Characterization of head actuator dynamics

3.3.1 Finite element modeling

Finite element analysis has been successfully used to study the dynamics of the actuator assemblies in hard disk drives. Generally, the finite element analysis is applied to predict the natural frequencies and their respective mode shapes of the actuator assembly. The boundary condition is the most important consideration in finite element modeling, so that correct and meaningful results can be obtained. In finite element modeling of an actuator assembly, the bearing elements are simulated using the spring system with the stiffness equivalent to an existing ball bearing. The bearing stiffness can be characterized via experimental dynamic measurement, which will be described later. It is obvious that rotational stiffness for the ball bearing is

almost zero. Therefore the spring elements as shown in Figure 3.7 can simulate the bearing system very well as long as we set the proper stiffness values to the springs.

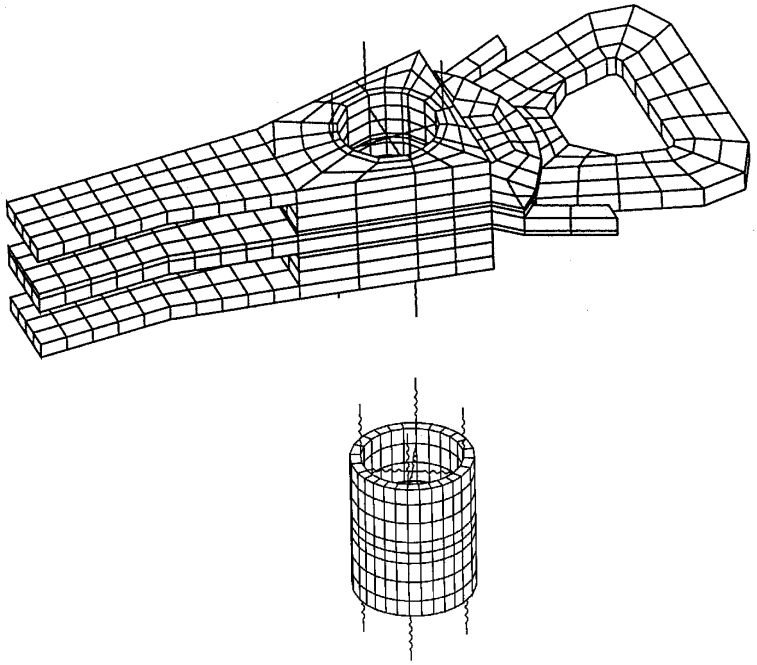

Figure 3.7: Finite element model of a HDD actuator and the pivot bearing.

The finite element model of the reference HDD actuator actuator assembly is shown in Figure 3.7. In the finite element modeling, the pivot ball bearing is modeled as a combination of a steel cylinder and a total of 16 node-node springs. Among them eight are in the radial direction (four in the lateral direction and four in the longitudinal direction, respectively) and eight in the axial direction. All springs are distributed symmetrically about the center of the bearing and about the pivot axis of the actuator. One end of each spring is fixed while the other end is connected to the cylinder. The measured values of the bearing stiffness are 20. MN/m in the radial direction and 5.33 MN/m in the axial direction, respectively. This works out to 5.0 MN/m for the stiffness of each of radial springs and 0.67 MN/m for the stiffness of each of the axial bearings. MSC/Patran is used in the pre- and post-processing of the model while MSC/NAStran

is employed in the frequency analysis of the model. Both 8-node hexhedron and 6-node wedge solid elements are used in discretizing the actuator, which is made of aluminum alloy. The material and sturctural properties used in the finite element model are shown in Table 3.1. Some of the typical resonance modes of the actuator are shown in Figure 3.8. The resonance frequency for arm rigid rotation mode along the pivot axis is zero, which is equivalent to implying that a ball bearing can freely rotate along the rotating axis. The resonance mode at 0.95 kHz is the actuator pitch mode, coupled with coil out-of-plane bending, which is due to the actuator mass and pivot bearing tilt stiffness and the coil stiffness. The most important mode which impacts the servo performance, i.e., the lateral translational mode and the actuator arm in-plane bending mode (also called butterfly mode) are at 4.3 kHz and 8.6 kHz respectively.

The frequency response can also be determined by finite element modeling. Generally, modal superposition is used to compute the frequency response function of a measurement point. The eigenvalues (natural frequencies) and eigenvectors (mode shapes) are obtained through the finite element modeling. The frequency response between an excitation point m and a response point k can be calculated using the first n modes (Li, 1999), as

$$G_{m,k}(f) = \sum_{r=1}^{n} \frac{p_{m,r} p_{k,r}}{m_r (2\pi)^2 (f_r^{\,2} - f^2 + j2\xi_r f_r f)} \tag{3.3}$$

where,

$G_{m,k}(f)$: frequency response between point point m and point k

$p_{m,r}$: element value in the excitation direction of point m in the r^{th} eigenvetor

$p_{k,r}$: element value in the excitation direction of point k in the r^{th} eigenvetor

m_r : r^{th} modal mass (=1 in case of normalized mass)

f_r : undamped natural frequency of the r^{th} mode

ξ_r : modal damping ratio of the r^{th} mode

f : frequency

Table 3.1: Material properties and pivot bearing stiffness used in the finite element modeling of an actuator assembly.

Material	Young's Modulus (MPa)	Density (kg/m^3)	Possion's Ratio
Aluminum	69000	2700	0.33
Steel	210000	7800	0.32

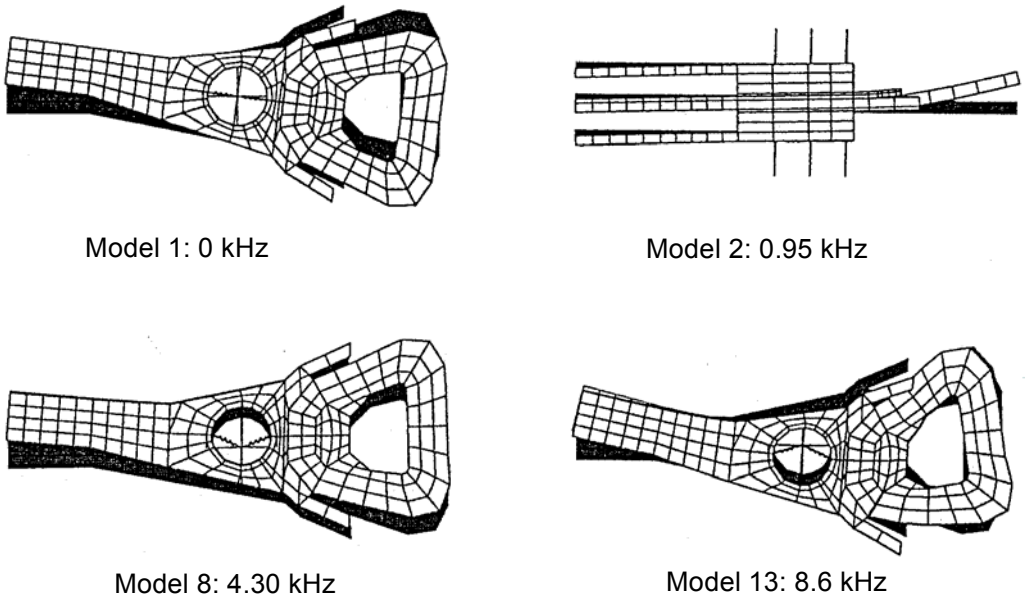

Figure 3.8: Mode shapes of a HDD actuator.

3.3.2 Experimental dynamic analysis

The purpose of the experimental dynamic analysis is to identify the actuator dynamics in terms of the mode shapes and the corresponding natural frequencies. Figure 3.9 shows the block diagram of the experimental setup of a voice coil motor excitation at the disk drive level. The experimental setup is used to measure the frequency response

function of head actuator assembly in the tracking direction. The head actuator arm is mounted on the pivot shaft and secured with a c-clip or side screw. It consists of a Laser Doppler Vibrometer (LDV) serving as the non-contact vibration measurement device with sub-micron resolution, and a Dynamic Signal Analyzer (DSA) serving as an excitation generator and a monitor of frequency response. In the experiment of characterizing actuator dynamics, a sweeping sinusoidal excited voltage/current from a wave form generator is fed into the VCM, and the response is measured by LDV. The LDV can measure both velocity and displacement of any point on the actuator. The frequency response function (FRF) is obtained and then passed to a post testing software so that a curve-fitting method can be applied to obtain the natural frequency, and damping ratio of the system. Figure 3.10 shows the measured frequency response of a conventional actuator. It can be seen that there exists many resonance peaks in the frequency region of interest. The resonance may correspond to the various modes of the head actuator assembly, for example torsion mode, the lateral translational mode, and the sway mode.

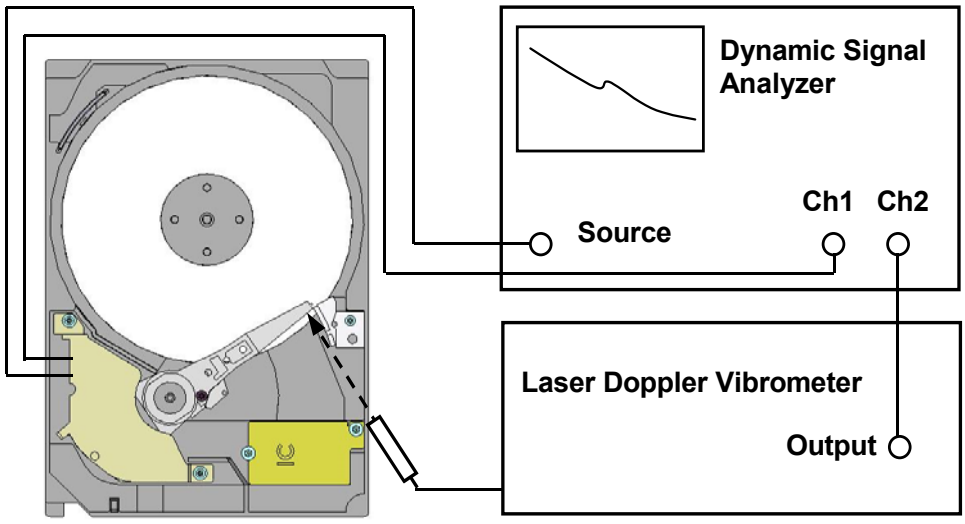

Figure 3.9: The block diagram of the experimental setup.

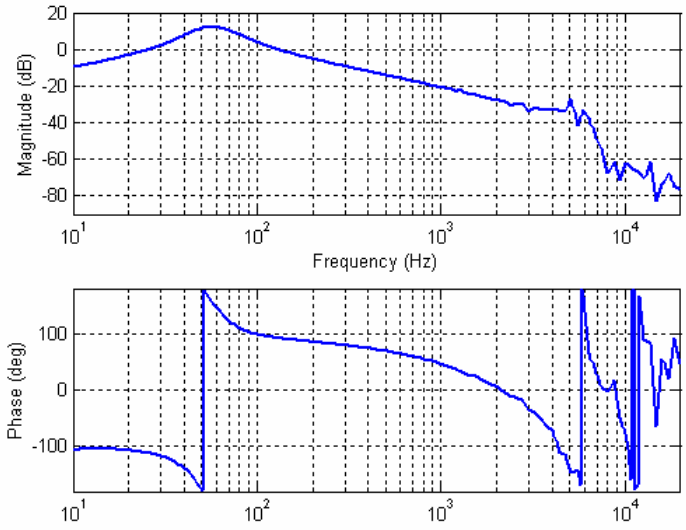

Figure 3.10: Measured frequency response of a disk drive actuator assembly.

3.3.3 Pivot bearing characterization

Pivot bearing plays a key role in the dynamic characteristics of an actuator assembly. The basic measures for a pivot bearing are the stiffness along the axial, radial and tilt direction. Generally the stiffness of a structure is characterized by a force and deflection relationship. However, for a pivot bearing, as the stiffness is high and the displacements of the pivot bearing along radial, axial, and tilt direction with a certain force is as small as in the micro level. This displacement may not be easy accurately measured. Therefore, an experimental approach is presented to characterize the stiffness of a pivot bearing by measuring the pivot bearing dynamics. Figure 3.11 shows the block experimental setup used to characterize the pivot bearing stiffness. The pivot bearing can be mounted to a base plate and fitted with a hollow mass cylinder. The base plate is mounted onto an adapter which is rigidly attached to a shaker. A Laser Doppler Vibrometer (LDV) with double splitter beams is used to sense the vibration signals of the base and the sample, which is an assembly pivot bearing

and the hollow mass cylinder. The shaker is excited using the Dynamic Signal Analyzer (DSA). In this experiment, a brass mass is used as the hollow mass cylinder. The pivot bearing is mounted in a U shape base by a shaft with two ends fixed. This can push high the resonance frequency of the shaft and make the resonance frequency due to the mass and the stiffness of the pivot bearing to be readily calculated.

To obtain the radial, axial, and tilt stiffness of the pivot bearings, the natural frequencies associated with bearing radial (f_{radial}), axial (f_{axial}) and tilt (f_{tilt}) vibration modes are identified from the measured frequency response. The bearing stiffness can be calculated using the following formula:

$$\left.\begin{aligned} k_{radial} &= m\,(2\pi f_{redial})^2 \\ k_{axial} &= m\,(2\pi f_{axial})^2 \\ k_{tilt} &= I_{tilt}\,(2\pi f_{tilt})^2 \end{aligned}\right\} \tag{3.4}$$

where, m is the mass of the hollow brass cylinder, I_{tilt} is mass moment of inertia calculated by

$$I_{tilt} = \frac{1}{4}m(R_1^2 + R_2^2) + \frac{1}{12}mh^2 = \frac{1}{16}m(D_1^2 + D_2^2) + \frac{1}{12}mh^2 \tag{3.5}$$

Here, D_1 and D_2 are the inner and outer diameters of the hollow brass cylinder respectively. h is the height of the cylinder. f is the resonance frequency obtained by frequency response measurement. This approach is applied to characterize the tilt stiffness of a conventional disk drive actuator pivot bearing. The cylinder mass and tilt inertia used for the experiment are 0.0417 kilogram and 2.66×10^{-6} kgm^2 respectively. The measured resonance frequency and the calculated pivot bearing stiffness are listed in Table 3.2. These stiffness values are those spring stiffness used in the finite element modeling of the pivot actuator assembly.

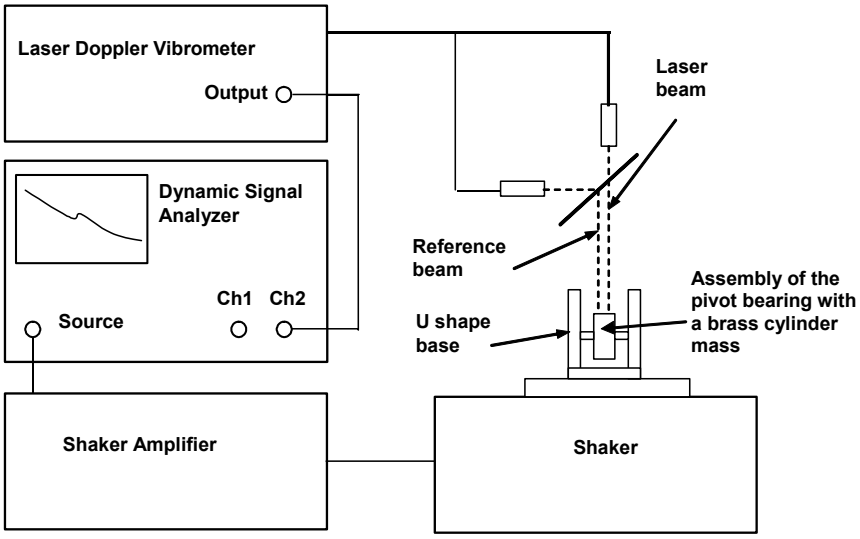

Figure 3.11: Experimental setup for characterization of a pivot bearing.

Table 3.2: Characterization of a conventional ball bearing stiffness.

Radial	Resonance frequency (Hz)	3500
	Stiffness (N/m)	20.20×10^6
Axial	Resonance frequency (Hz)	1800
	Stiffness (N/m)	5.33×10^6
Tilt	Resonance frequency (Hz)	2100
	Stiffness (Nm/rad)	463

3.4 Design of an actuator assembly with force coupled actuation

In order to suppress the lateral translational vibration mode excited by the reaction force, several approaches, including moving-magnet actuators (Chen, et al., 1997) and dual as well as single moving-coil actuators (Aruga, et al., 1996; Mah, et al., 1999), have been investigated. However, it is noted that there are significant bias force and

hysteresis with a moving-magnet actuator. Also, extra magnets attached to the actuator moving part increase the total mass and inertia of the actuator arm. This will degrade dynamic performance and increase the access time of the read/write head. In addition, the exposure of magnets in a moving magnet actuator leads to difficulties in the production and assembly processes of the actuator. Therefore, a moving-coil actuator with a novel design in VCM construction, which can generate coupled force or pure torque, seems a practical way to realize high servo bandwidth for a head positioning system.

3.4.1 Structure design

Efforts have been made to develop a novel moving-coil actuator. Figure 3.12 and Figure 3.13 show the construction of the newly developed moving-coil actuator. Its construction is different from a conventional moving-coil actuator, especially in the coil structure and magnet arrangement. The coil is constructed to be a simple movable elongate planar coil. The permanent magnet/magnets is/are constructed to have four alternative polarities in-turn rigidly located on yoke plate/plates, which can be interpreted as a single magnet with four poles or two magnets with two poles each. The provision of the particular construction of the single planar driving voice-coil and the magnet member with the help of the yoke member can generate forces F_1, F_2, F_3 and F_4, in the four portions of coil. These forces generated are orthogonal to the track-crossing direction so that the reaction force in that direction, exerted on pivot bearing and shaft, can be substantially suppressed. Hence, the resonance due to the pivot bearing and the actuator mass at the mid-band frequency can also be eliminated in an ideal case. Also, the planar coil, permanent magnet and yoke plates used here are almost as simple as those in a conventional voice coil motor (VCM) so that the

manufacturing and assembling processes can be as simple as that in the case of a conventional actuator.

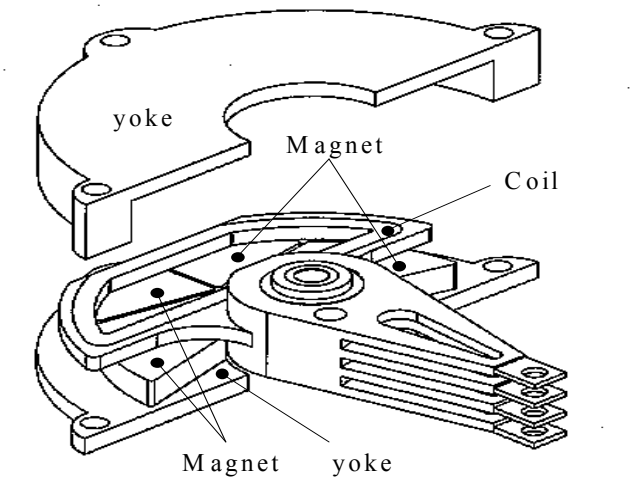

Figure 3.12: The proposed actuator assembly for force coupled actuation.

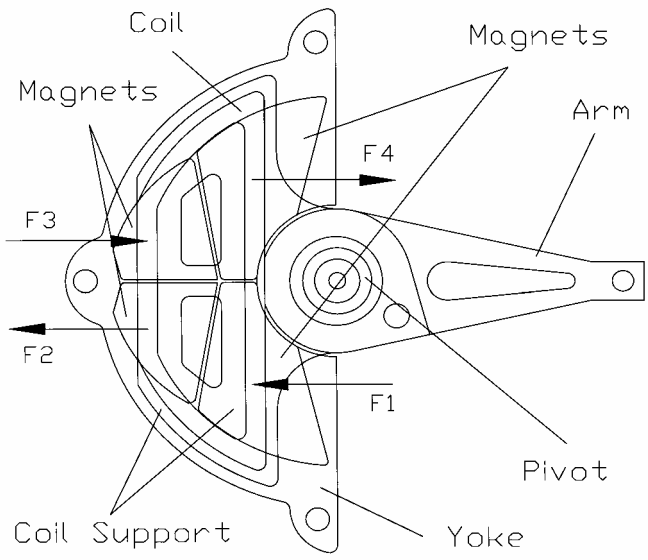

Figure 3.13: Top view of the proposed actuator assembly with coupled force generation.

3.4.2 Electromagnetic design and optimization

The electromagnetic design and optimization are performed to the proposed force coupled actuator assembly to maximize the torque or motor constant with smallest motor size and less material (Lin, et. al., 2001). Also, it is crucial for the actuator to produce sufficient force or torque to move a certain load (coil and coil support, arm, suspension, slider and Read/write heads) over a certain angular displacement with minimal seeking time and power dissipation. The electromagnetic finite element modeling is employed to decide some critical dimensions and electromagnetic parameters, including motor height, magnet shape and size, air gap flux strength, and air gap length. Parameters in motor magnetic circuit and coil design had been optimized and adjusted to maximize torque and motor constant. Some parameters of the actuator predicted in electromagnetic design, in comparison with a reference conventional actuator used in a commercial HDD, are shown in Table 3.3. The proposed force coupled actuator assembly leads to a better electromagnetic performance compared to a conventional actuator used in a hard disk drive.

Table 3.3: Parameters of the force coupled actuator and a reference actuator.

Electromagnetic properties	Force coupled actuator	Reference actuator
Coil resistance (DC) (Ω)	26	37
Coil inductance (mH)	7.8	10.3
Torque constant K_t (N.m.Amp^{-1})	0.118	0.121
Motor constant (N.m. W$^{-0.5}$)	0.023	0.018
Moment of inertia J_m (kg.m^2)	4.67×10^{-6}	5.7×10^{-6}
Electrical time constant (ms)	0.3	0.28
Mechanical time constant (ms)	8.7	14

3.5 Dynamic characteristics analysis and measurement of the force coupled actuator assembly

3.5.1 Finite element analysis

The dynamic performance of high bandwidth actuator assembly is predicted using a 3-dimensional finite element analysis. In the finite element modeling, the arm assembly is modeled using a number of eight-node hexahedron and six-node wedge elements. Linear spring elements were used to model the radial and the axial stiffness of the pivot bearing. The actuator resonances and the corresponding mode shapes with natural frequencies excited due to pivot and arm assembly were identified. The design of the carriage arm assembly is optimized to enhance the structural stiffness of the actuator.

Figure 3.14 shows two typical resonance modes. They are the lateral translational resonance mode at 5.25 kHz and the first lateral in-plane bending mode at 11.5 kHz. The lateral translational vibration mode is along the tracking direction. It is due to the spring constant of the pivot bearing and the movable masses of the actuator assembly. The in-plane bending mode is primarily from the bending of the arm in the lateral direction and the bending of the coil in the longitudinal direction.

Using the mode superposition of the first 20 modes, the frequency response of the arm tip displacement over an orthogonal driving force generated by the coil was obtained. In the calculation, the damping ratio of the lateral translational mode is set to be 0.04 and that of the in-plane bending mode is 0.03. The result is shown in Figure 3.15. It is noted from the result that the lateral translational vibration mode is at 5.25 kHz with a

very small peak and the lateral in-plane bending mode located at 11.5 kHz becomes the primary resonance with a peak of about 10 dB.

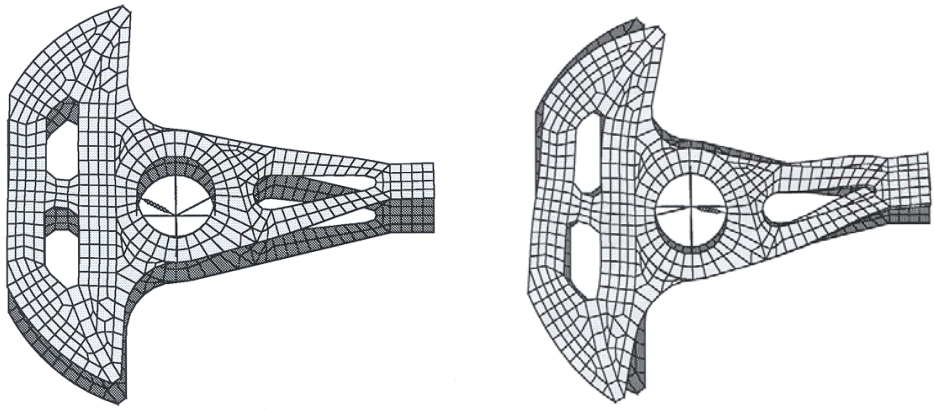

(a) (b)

Figure 3.14: The mode shapes of some typical resonance modes. (a) Lateral translational mode at 5.23 kHz. (b) Lateral in-plane bending mode at 11.5 kHz.

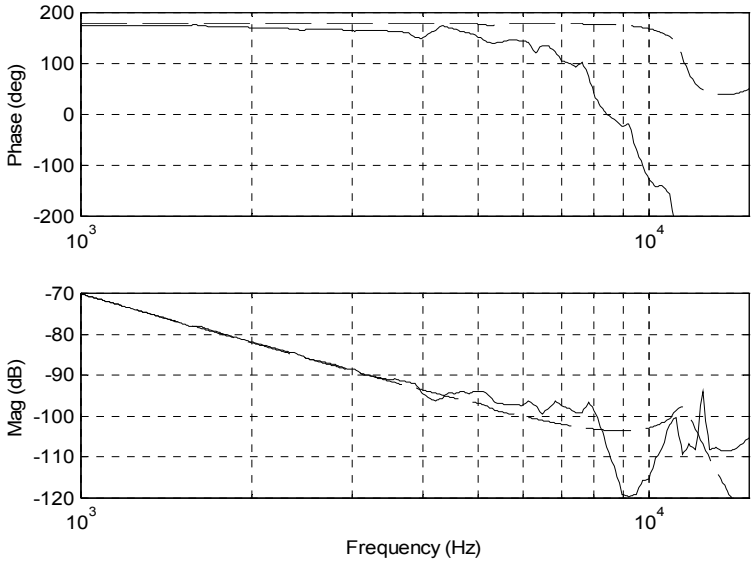

Figure 3.15: Frequency response of the actuator assembly obtained by FEA (dashed line) and by measurement (solid line).

3.5.2 Frequency response measurement & discussion

The actuator is prototyped and the frequency response of the actuator assembly is measured using a Laser Doppler Vibrometer (LDV). In the measurement, the actuator

assembly is mounted on a rigid base plate and the top end of the pivot was rigidly supported. Figure 3.15 also shows the measured frequency response of the displacement of the top arm tip over VCM driving current. From the result, we can see that the lateral translational mode around 5.3 kHz is almost suppressed.

It is observed from the measurement results that the primary resonance mode in the frequency response measured is around 8 kHz. This mode is the first lateral in-plane bending mode and is much lower than the result predicted by finite element analysis (FEA) (11.5 kHz). This is due to the prototyping of the actuator. As the coil of the prototyped actuator is made manually and its attachment to the coil support part is not so rigid so that the stiffness of the VCM part of the actuator is much lower than that in the commonly-used case, as used in the FEA. This will lead to lowering the stiffness of the whole structure so that the frequency of the lateral in-plane bending mode becomes lower. This can be verified using FEA. If we lower the values of the Young's modulus of the coil and the coil support (plastic) to one fifth of their original values, respectively, then the frequency of the lateral in-plane bending mode becomes approximately 8 kHz, as shown in Figure 3.16. This can explain the reason why the experimental result shows difference from the result predicted by the FEA.

If the actuator is manufactured and assembled by a production line, it is believed that the above-mentioned problem will be solved. The stiffness of the VCM part will become as rigid as that of a commercial actuator. The frequency of the lateral in-plane bending mode will match the result obtained by FEA. Furthermore, if we use materials with high stiffness instead of aluminum for the E-blocks of the actuator, we can obtain a much higher frequency of the lateral in-plane bending mode. For example, aluminum

boron carbide has very high stiffness (Young's modulus is 280 GPa, vs. 70 GPa for aluminum), while it is very light (density is 2680 kg/m^3, same as aluminum) (Adley, et al., 1998). We can again verify this by FEA, using aluminum boron carbide instead of aluminum for the actuator arm. The frequency of the lateral in-plane bending mode becomes 15.7 kHz, which is much higher than 11.5 kHz, as shown in Figure 3.17.

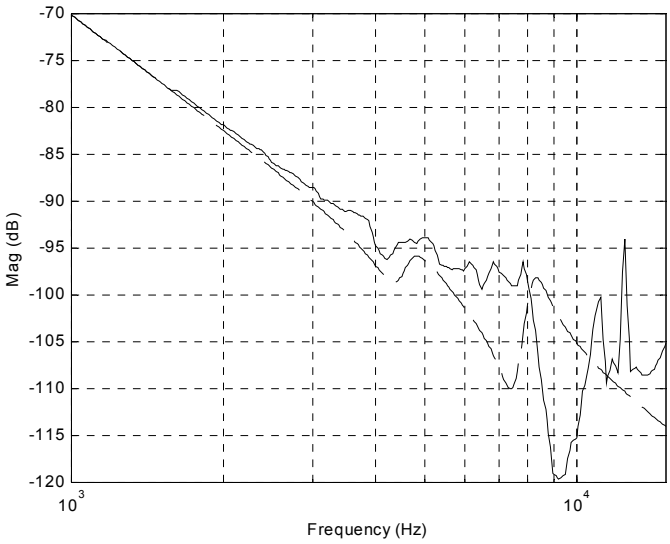

Figure 3.16: Frequency response obtained by FEA (dashed line) by using 1/5 stiffness of original values for the coil and the coil support (plastic) compared with that measured (solid line).

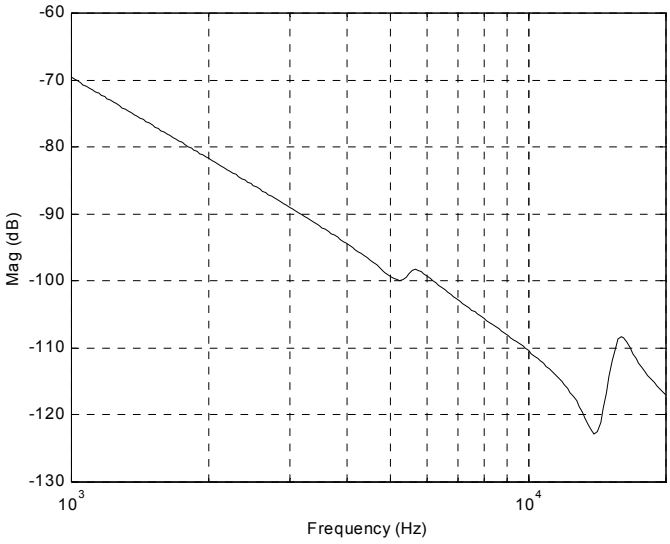

Figure 3.17: Frequency response obtained by FEA using aluminum boron carbide instead of aluminum for E-blocks.

3.6 Summary

The basic dynamics of the head actuator assembly and the dynamic characterization methods are described. A pivot bearing stiffness characterization approach via dynamic testing is presented and it is effective in measuring the pivot bearing stiffness. A novel high bandwidth moving-coil actuator has been designed and fabricated. With the unique construction of voice coil and the arrangement of magnet, the force produced by the novel actuator assembly is orthogonal to track-crossing direction so that pure torque can be obtained. The reaction force exerted on the pivot bearing and shaft can be significantly minimized. The dynamic performance of actuator assembly has been evaluated using 3-dimensional FEA. The frequency response characteristics of the actuator assembly show the unexpected lateral translational resonance mode is substantially suppressed. It is believed that the servo system supported by the novel actuator assembly can achieve higher bandwidth for high TPI magnetic recording.

CHAPTER 4

DEVELOPMENT OF A FLEXURAL PIVOT FOR USE FOR HARD DISK DRIVE ACTUATOR

A cross leaf flexural pivot is proposed and designed for use in disk drive actuator to replace the current ball bearing system. The static and dynamic performances of the proposed design are investigated using finite element analysis. It is shown that a flexural pivot can achieve a translational stiffness comparable to current ball bearing system and lower tilt stiffness. The design is prototyped and its dynamic characteristics are experimentally investigated. Control implementations show that the actuator assembly with the flexural pivot has the potential to be used in hard disk drives.

4.1 Introduction of flexural bearings in disk drive actuators

To stay competitive in the highly volatile HDD industry, cost cutting is a must. Currently, ball bearings are used in hard disk drives to provide the rotational mechanism. However, they operate with friction and damping, causing non-linearity in the actuator, and therefore, this makes the position control more difficult (Prater, 1995 and Liu et al., 2000). Flexure bearings, on the other hand, are simpler in structure and therefore have potential for lower cost. The objective of the research involved in this paper is thus to design a flexural pivot, which can replace the ball bearing system currently used in hard disk drives without sacrificing performance.

An actuator comprised of a parallel pair of steel leaf springs which support a moving coil in a voice coil motor (VCM) has been proposed by IBM Research Division,

(Chainer et al., 1991; Sri-Jayantha et al., 1991). In the design, the actuator translation is produced by the bending of the flexible ends. The motion is generated without any metal contact typical of conventional ball bearing based actuator systems. Therefore, the system does not generate any particulate debris or require any lubrication, resulting in very clean operation. The absence of metal contact eliminates friction forces, offering potential for very fine motion control. In addition, the translational motion of the actuator produces a small ±1.0 degree skew angle at the recording head, much lower than conventional rotary designs. Investigation also indicates the presence of the significant bias forces and low-frequency modes, which are the hindrances to achieve high servo performance in the flexural actuator. In the work reported by He et al. (2002), the disk drive actuator can be designed with a slant suspension, which achieves ± 2.0 degrees skew angle. The dynamic performance of the slanted actuator does not change significantly from that the un-slanted actuator. However, as the design of the slanted actuator increases in the arm length, this will cause the resonance frequency to drop by 20 ~ 30%.

This chapter presents a cross leaf flexural pivot for use for hard disk drive actuator. The static and dynamic performances of the flexural pivot are investigated using finite element analysis. The design is prototyped and further characterized experimentally. Frequency response measurement on the different positions (inner track, neutral track and out track) of the actuator with flexural pivot are measured. Dynamic frequency responses are measured before and after a certain period of life cycling test. The servo control application using the flexural pivot in a disk drive as a single stage servo and the application of the flexural pivot *cum* with a micro-actuated suspension as a dual stage servo have been implemented.

4.2 Design and simulation

The design configuration of the cross leaf flexural pivot is shown in Figure 4.1 and Figure 4.2. The pivot consists of a shaft (the fixed part), a housing race (the moving part) and 4 flexure leaves. Figure 4.1 shows the configuration of monolithic flexural pivot, which can be fabricated by machining the pivot as a whole part using an electric discharge machine. Figure 4.2 shows the flexural pivot as an assembly, which is fabricated by mounting the 4 flexures to the housing and the shaft. The assembly of the flexural pivot to the disk drive actuator arm is shown in Figure 4.3. The central shaft is the fixed part and used to fix the actuator to the disk drive base or cover as shown in Figure 4.4. In the application, when a magnetic force is induced by the voice coil motor acting on the coil, the actuator will rotate along the rotation center, roughly the cross center line of the 4 leaf flexures, as shown in Figure 4.1.

According to the specifications of a hard disk drive, the proposed flexural pivot design should meet the requirements as (1) sufficiently high translation stiffness and tilt stiffness (for pitch and roll); (2) sufficiently low rotational stiffness (rotation angle > ±12 degrees at a specified torque); (3) sufficiently low stress in the flexures and long fatigue life; (4) high shock resistance and (5) high capability to withstand thermal stress. Therefore, the design dimension and material selection are the important issues for the design consideration. As stainless spring steel sheet are widely used in flexure design, it is suggested that the material with high fatigue strength (such as fully hardened stainless steel 420) be selected as the flexure material as its fatigue limit may reach 1000 MPa (Lampman, 1989). After a lot of trial computation, the effective length, width, thickness and the space between the flexures are selected as 8.0 mm, 2.25 mm, 0.01 mm and 1.0 mm respectively.

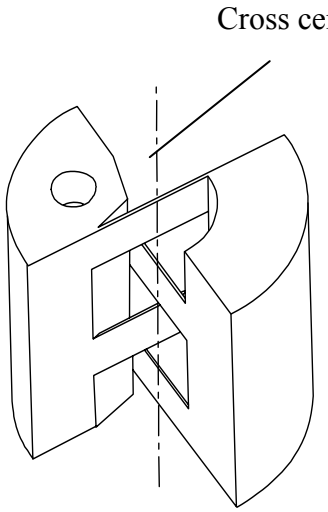

Figure 4.1: A monolithic flexural pivot.

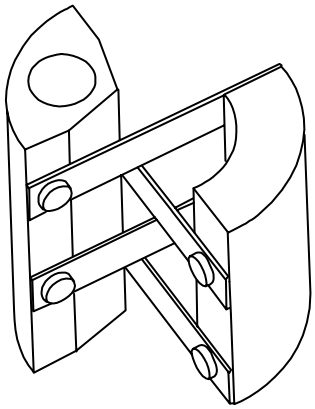

Figure 4.2: An Assembled flexural pivot.

Finite element modeling is employed to investigate the static and dynamic performance of the assembly of the flexural pivot to actuator. The housing, central shaft and the flexures of the flexural pivot are given the material properties of stainless steel while the actuator arm is given the material properties of aluminum. The central shaft hole surface is fully constrained, as in the design, it would be fixed to the disk drive base and cover. For static analysis, a uniform force, equivalent to the maximum force induced by the voice coil motor, is applied onto the coil surface so as to produce a torque along the actuator rotation center. The maximum calculated rotation angle is

14 degrees, which is greater than the specified 12 degrees. The maximum principal stress exists in the flexures is found to be 847 MPa, which is less than the material fatigue limit for fully hardened stainless steel AISI 420. Hence, for the 12 degrees stroke, the maximum principal stress should be lower than 847 MPa.

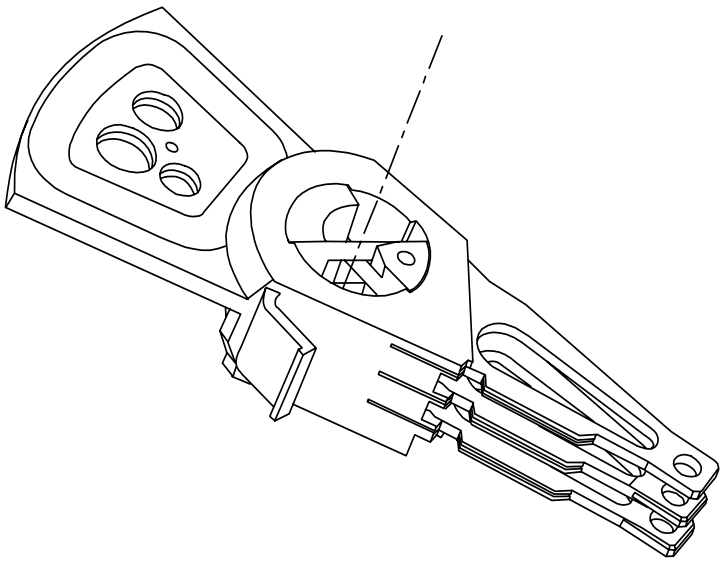

Figure 4.3: Assembly of magnetic disk drive actuator with flexural pivot.

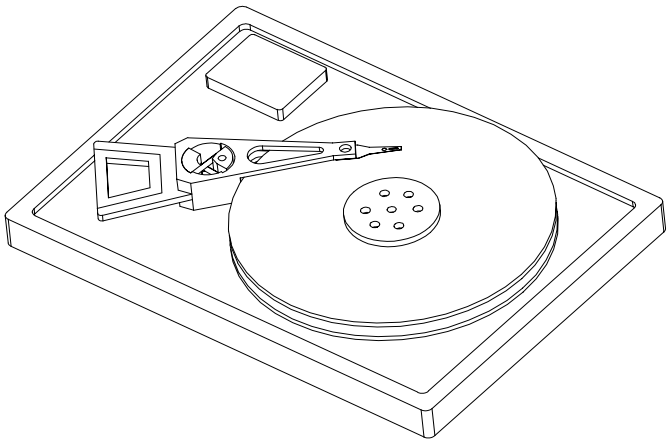

Figure 4.4: An assembly of the flexural pivot, actuator and hard disk drive.

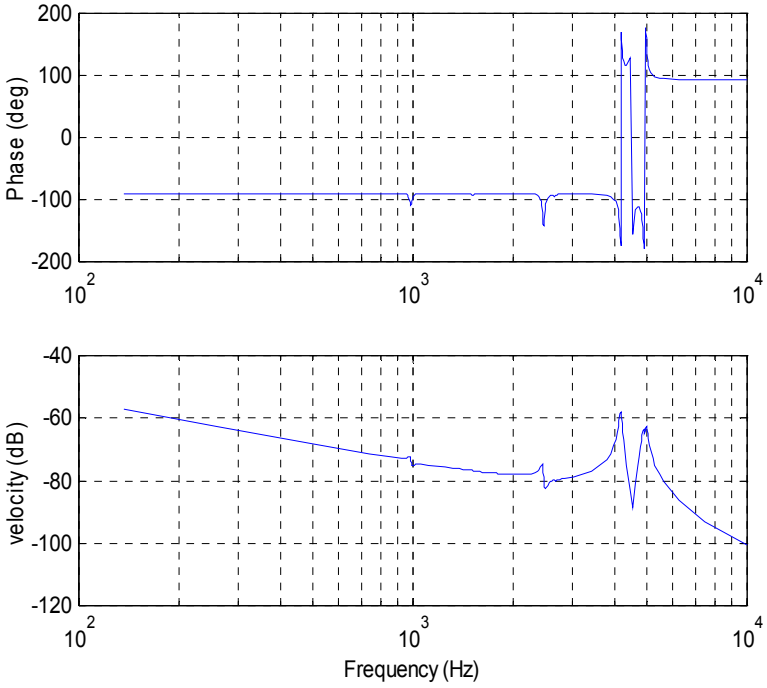

Figure 4.5: Frequency response of actuator arm tip with flexural pivot.

Figure 4.5 shows the frequency response of the actuator arm tip with the flexural pivot. It can be seen that the first dominant mode is 2.5 kHz. It is the first roll mode of the flexure pivot. This mode will become the first limit to affect actuator track mis-registration (TMR).

The pivot stiffness can be characterized by the resonance frequencies in radial, axial and tilt directions, and the mass properties of the flexural pivot.

$$k_{translation} = m(2\pi f)^2 \tag{4.1}$$

$$k_{tilt} = J(2\pi f)^2 \tag{4.2}$$

where, m is the total mass of the system and J is the inertia of the system to corresponding coordinate axes at the center of the mass. In the actuator design, the center of mass is roughly at the rotation center, the cross center line of the 4 flexures. f

is the resonance frequency in different directions. The reference coordinate system is shown in Figure 4.6.

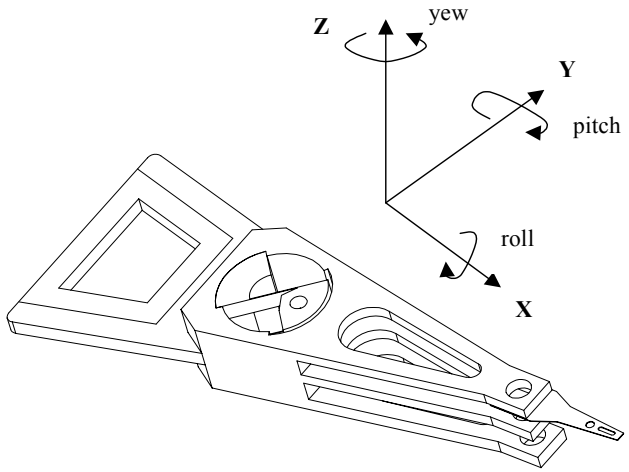

Figure 4.6: The coordinate system for pivot rigid body motion.

The actuator resonance frequencies in radial, axial and tilt directions, calculated stiffness and the reference ball bearing resonance frequencies and stiffness are listed in Table 4.1. It can be seen that the flexural pivot has sufficiently high translational stiffness. The translation stiffness is even comparable to that of ball bearings. The tilt stiffness is not as high as that of a conventional ball bearing and results in a lower resonance frequency, which is not beneficial to the actuator performance. However, as the amplitude of the tilt resonance is low, it does not play a significant role in the actuator performance. The rotational stiffness is low enough to reach a large deflection more than 12 degrees at the driven force range. But it is higher than that of a ball bearing. This causes an additional effort for the servo engineer to deal with flexure spring force in control design. However, the flexural bearing eliminates the friction effects.

Table 4.1: The natural frequencies and the stiffness of the designed flexural pivot and the comparison with ball bearing stiffness (Translatory: N/m; Rotational: Nm/rad).

Specs	Frequency (Hz)	Stiffness	Ball Bearing Stiffness
X	4929	10.8×10^{6}	20.0×10^{6}
Y	4133	7.6×10^{6}	
Z	2468	2.7×10^{6}	5.3×10^{6}
Roll	2389	98	463
Pitch	954	73	
Yew	15	1.98×10^{-2}	0

As the pitch stiffness of the flexure pivot is much lower than that of ball bearing, it is necessary to investigate how much effect this has on the vibration amplitude. A frequency response analysis is performed on the structure. In the analysis, a uniform base excitation is applied onto Z-direction of the structure and 1% damping ratio is used. The result is shown in Figure 4.7. It is found that the vibration peak due to the pitch motion is less than 2.3×10^{-7} mm, about 1/5 of that induced by the actuator arm up-down bending mode.

The stainless steel has good thermal stability. Normally the thermal stress can be estimated as

$$\sigma = E\varepsilon = E\eta\Delta T \tag{4.3}$$

where: E is Young's Modulus, η is the coefficient of thermal expansion and ΔT is the temperature range. For stainless steel, at a temperature change 55°C (IBM Storage Product), the estimated thermal stress is about 180 MPa, far below the fatigue limit of the material.

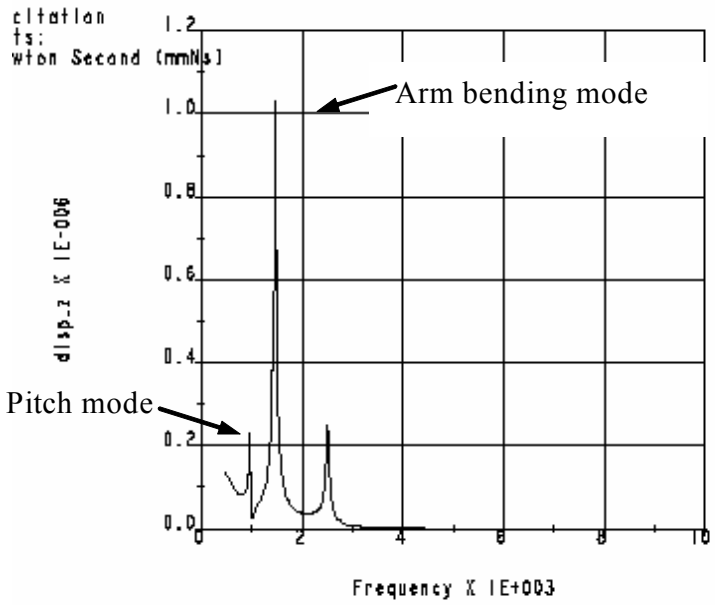

Figure 4.7: Frequency response of actuator arm tip (along Z direction) with flexural pivot.

4.3 Prototyping and testing

The prototypes of the flexural pivots are shown in Figure 4.8. In the prototypes, the shaft and the housing race are made of mild steel while the flexures are made of spring steel. The assemblies of the flexural pivot with actuator and the hard disk drive are shown in Figure 4.9 and Figure 4.10 respectively.

Figure 4.8: The prototypes of flexural pivot.

Figure 4.9: The assembly of a prototyped flexural pivot to an actuator arm.

The experimental measurements are conducted onto the assembly of the actuator with flexural pivot to a HDD drive. Static testing showed that the bias current needed is 80 to 100 mA based on Seagate U4 voice coil motor. Measurement of frequency response showed some difference with the simulation. This is due to the prototyping process and also to the dimensional differences between the actual prototypes and the design. Life cycling test is conducted on the flexure pivot. A drive based assembly incorporating the flexure pivot and actuator is used in the experiment. A function generator is employed to generate a sine wave signal to the actuator so that a repeated actuator stroke ±12° is obtained. After 3,000,000 cycles testing, the flexural pivot is observed without any damage.

Figure 4.10: The assembly of the actuator arm with flexural pivot to HDD.

Figure 4.11 shows the frequency responses of flexural pivot before and after life cycling test. It is obvious that there is not much difference observed. Figure 4.12 shows the frequency responses at the arm tip of the assembly of the actuator with flexural pivot at different positions, neutral position inner track and outer track respectively. The resonance shift is also listed in Table 4.2. From Table 4.2 and Figure 4.12, it can be seen that the first dominant mode (2.08 kHz) shift is within 5%. There is no obvious shift for the second and the third dominant resonance frequencies (2.6 and 5.1 kHz respectively), while the actuator arm is at the innermost track and outermost track positions.

Table 4.2: The dominant resonances shift.

Resonance frequency (kHz)	MD	OD	ID	Shift Variance
1st resonance	2.08	2.02	2.16	4.9%
2nd resonance	2.56	2.56	2.56	0
3rd resonance	5.12	5.12	5.12	0

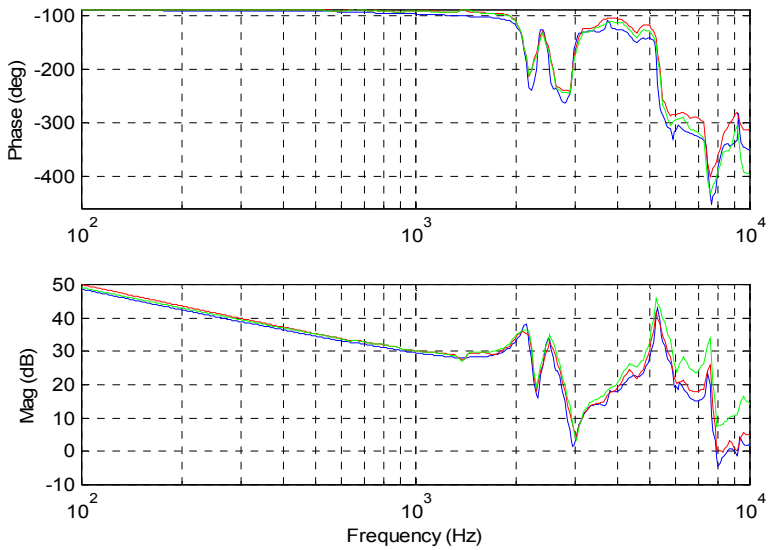

Figure 4.11: Frequency response at the arm tip of the assembly of actuator with flexural pivot before and after life cycling test.

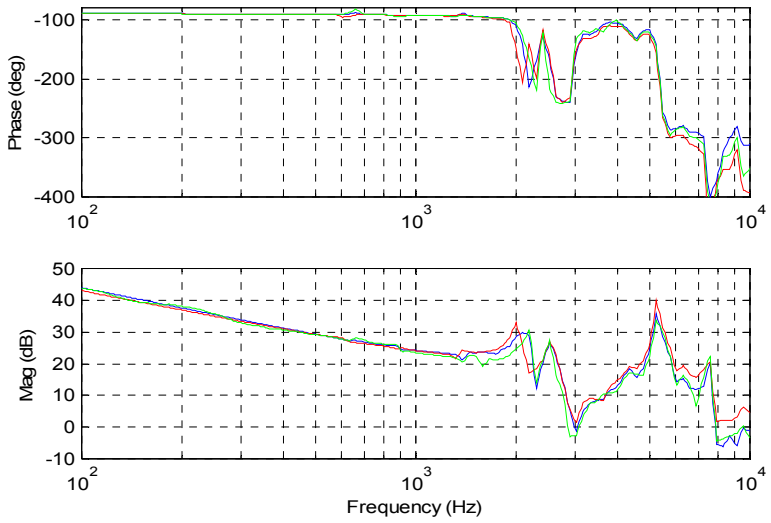

Figure 4.12: Frequency responses at different positions (blue line-MD, red line-OD and green line-ID).

4.4 Control design and implementation

In order to test the performance of the developed prototype of flexural pivot, control designs and implementations are carried out in both single-stage and dual-stage cases. The single stage servo control system uses the VCM using flexural pivot as the basic actuator; the dual-stage servo control system uses the said VCM as the primary actuator for coarse positioning and a PZT active suspension as the secondary actuator for fine positioning. The control designs are implemented in the real-time system dSpace with DSP (TMS320C31). The sampling rate was 20 kHz. The position signal was measured using LDV at the resolution of 2 μm/V. The schematic of control implementation is shown in Figure 4.13, in which only VCM loop is on in single stage control and both VCM and PZT loops are on in dual-stage control.

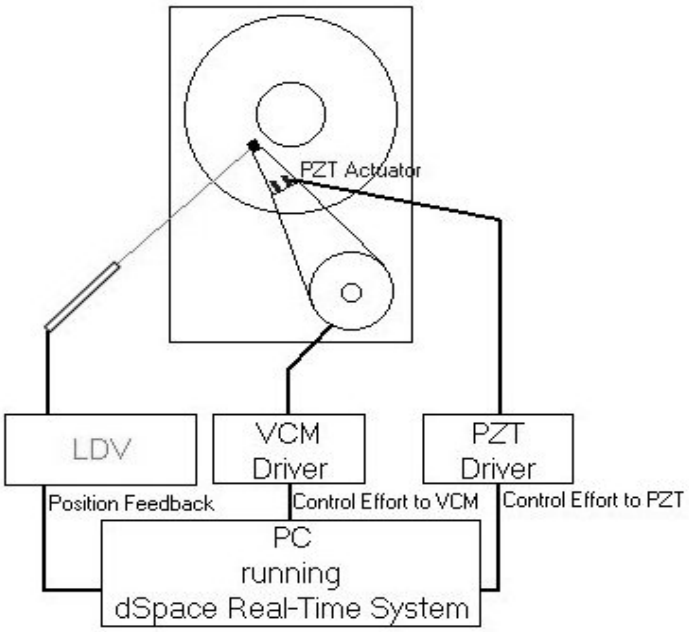

Figure 4.13: The schematic of control implementation systems.

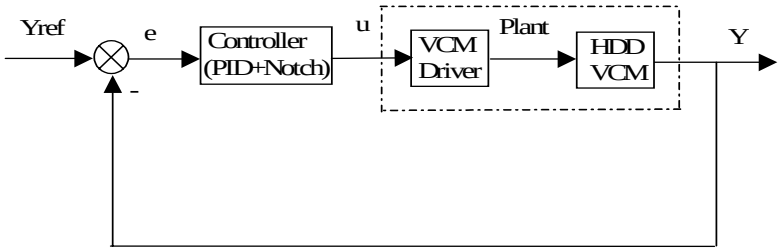

Figure 4.14: The block diagram of a single stage control system.

4.4.1 Single stage control design and experimental results

Based on the frequency response shown in Figure 4.12, a single-stage HDD control system was established as illustrated in Figure 4.14. A PID controller $C(z)$ with notch filter $H_{nf}(z)$ was designed for this system, where

$$C(z) = K_p(1 + \frac{T_s}{T_i}\frac{z}{z-1} + \frac{T_d}{T_s}\frac{z-1}{z}) \tag{4.4}$$

$$H_{nf}(z) = \frac{n_0 z^2 + n_1 z + n_2}{z^2 + d_1 z + d_2} \tag{4.5}$$

The control system implementation results are shown in Figure 4.15 (open system bode plot) and Figure 4.16 (Step response). In Figure 4.16, CH1 shows the system output while CH2 shows the corresponding control signal. The corresponding controller parameters are listed as follows:

$K_p = 0.2$, $T_i = 0.05$, $T_d = 0.0005$, $n_0 = 0.9269$, $n_1 = -1.4265$, $n_2 = 0.8865$,

$d_1 = -1.4265$, $d_2 = 0.8134$.

It was found in the experiment that the actuator using the pivot bearing possesses satisfactory characteristics. The HDD control system using the newly developed actuator can obtain a crossover frequency of 623 Hz, GM of 6.6 dB, PM of 530 degrees, and the step response of the control system can settle down in less than 1 ms.

4.4.2 Dual-stage control design and experimental results

A dual-stage servo control system composed of VCM and PZT active suspension is studied for the exploration of servo bandwidth using the flexural pivot. The model of PZT milli-actuator is shown in Figure 4.17. Because there is no direct measurement of relative position between PZT milli-actuator and VCM, the parallel control structure is adopted for the implementation of dual-stage servo system. Figure 4.18 shows the block diagram of the parallel dual-stage control structure. The notch filters were designed to compensate for the resonance in VCM and PZT models. For the compensated plant models, PID controller $Cv(z)$ was designed in VCM path and a lag compensator $Cp(z)$ was designed in PZT path.

$$Cv(z) = \frac{50.5z^2 - 100.5z + 50}{z^2 - z} \tag{4.6}$$

$$Cp(z) = \frac{-39.3984z + 2.4218}{z - 0.98} \tag{4.7}$$

The control design was implemented as shown in Figure 4.13. The servo bandwidth was 1,700 Hz with PM of 45 degrees and GM of 7 dB; the rise time in step response was about 0.2 ms and the settling time was about 0.5 ms. Figure 4.19 shows the overall open-loop bode plot of dual-stage control system. Figure 4.20 shows the step response of the dual-stage system.

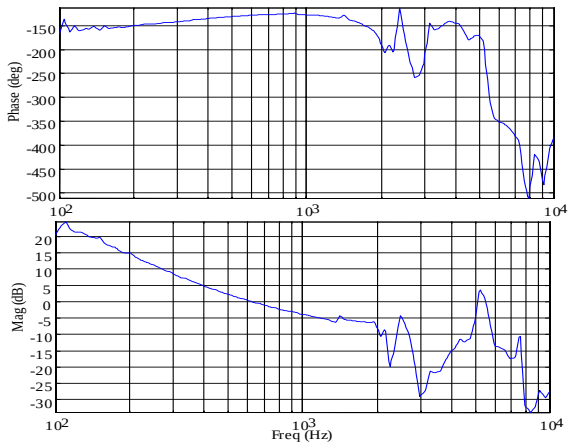

Figure 4.15: The open-loop plot of single stage control system.

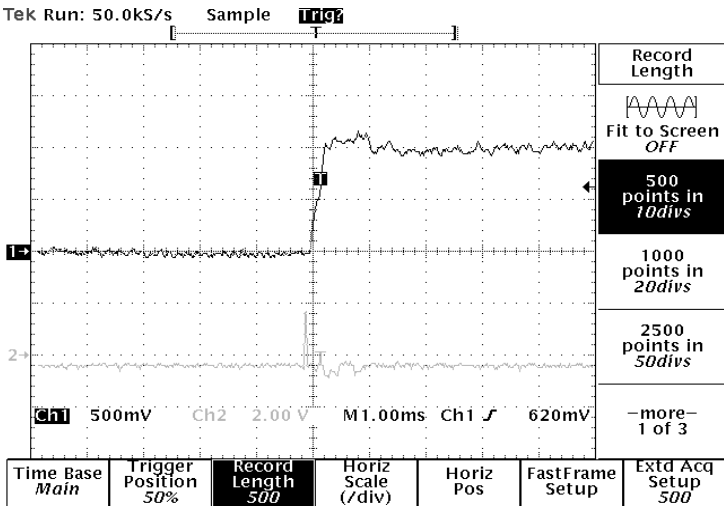

Figure 4.16: The step response of single stage control system.

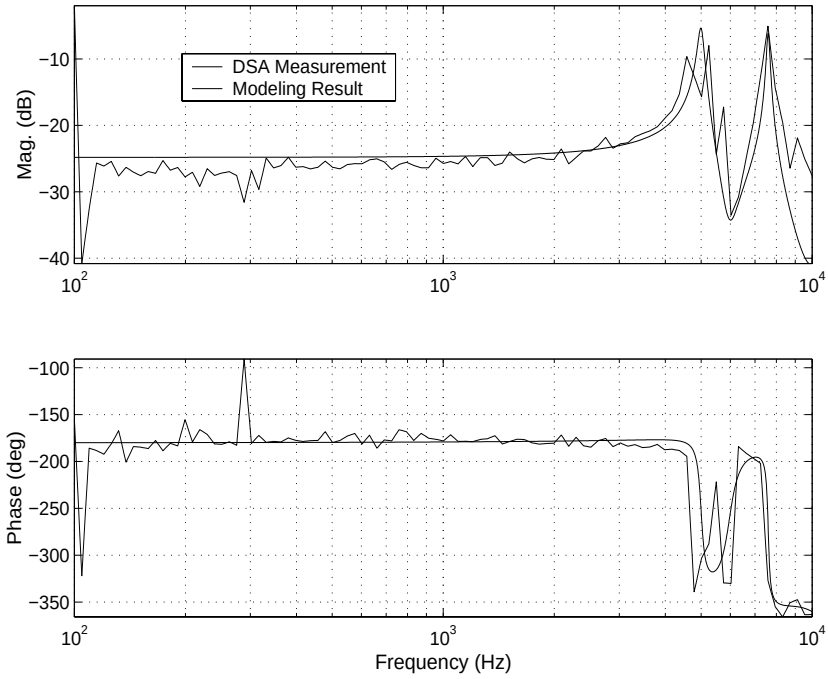

Figure 4.17: The PZT micro-actuator modeling.

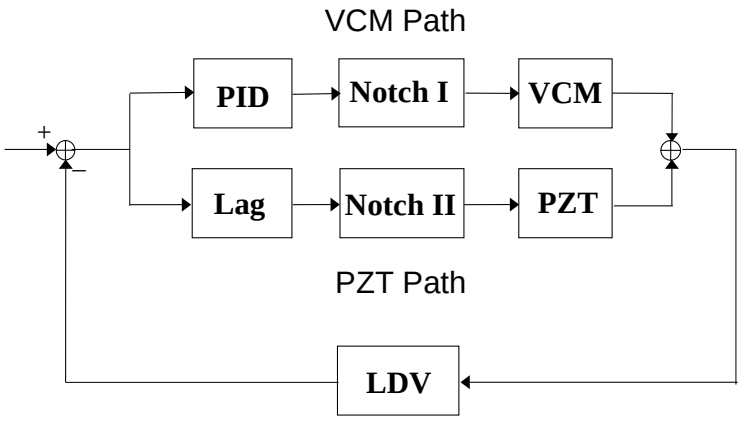

Figure 4.18: The parallel dual-stage control structure.

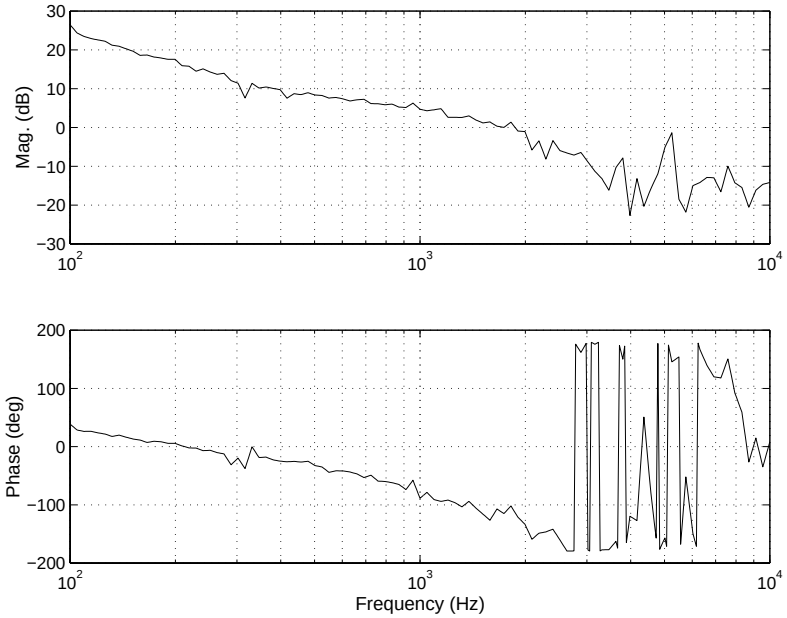

Figure 4.19: The open-loop bode plot of a dual-stage control system.

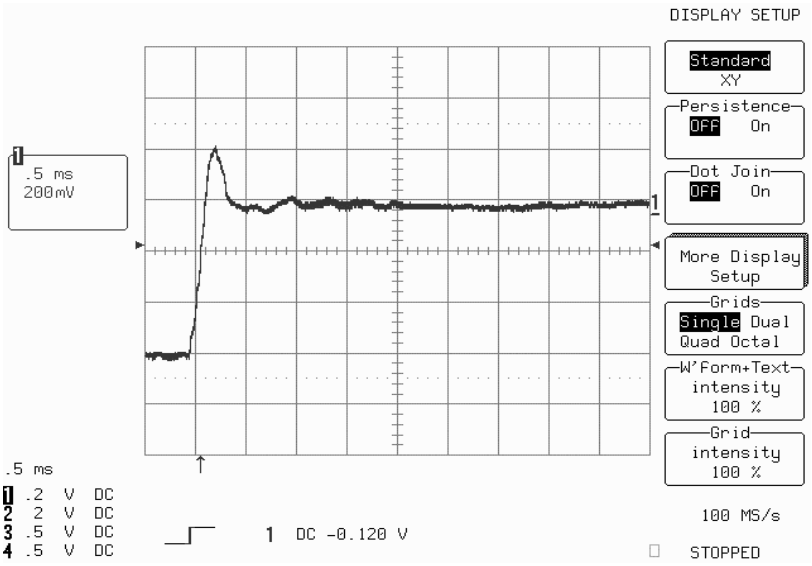

Figure 4.20: The step response of the dual-stage control system.

4.5 Conclusions

The 4-leaf cross-flexural pivot is proposed for use in disk drive actuator assembly instead of the currently used ball bearing. The design has comparable translational stiffness and lower tilt stiffness compared with the existing ball bearing system. The prototyped flexural pivot has been tested for more than 3 million life cycles without any failure. The dynamic performances of the flexural pivot after life cycling test do not change compared to those before the life cycling test. Single stage control implementation shows the potential of the flexural pivot to be used in hard disk drives. Dual-stage control by a micro actuator has demonstrated improved performances of actuator assembly using the flexural pivot.

The flexural pivot is a novel design for hard disk drive actuator assembly [He et al. (2002)]. It can also be used in other similar mechatronic devices.

CHAPTER 5

OPTIMIZATION OF A DISK DRIVE ACTUATOR WITH SMALL SKEW ACTUATION

Currently the utilization of the voice-coil-motor for actuating read/write head elements in magnetic hard disk drives (HDD) results in a skewed actuation, which necessitates an involved micro-jogging process and thus a complicated servo system. In perpendicular recording systems, a small skew actuation will relax the requirement on pole trimming. This chapter presents a magnetic hard disk drive actuator and suspension assembly with small skew actuation. In the present study, the distance from the actuator pivot to the read/write head is chosen so that the skew angle variation is minimized. After that, the suspension head is assembled to the actuator arm at a slant angle with respect to the actuator longitudinal direction to achieve a small absolute skew actuation. Finite element modeling and experimental measurements reveal that there are no significant changes of the actuator assembly dynamic performance with and without the slant angle.

5.1 Introduction

As the areal density of future magnetic recording increases to Terabits/in^2, the distance between read/write elements and the disk surface is reduced to the near-contact regime. Many magnetic disk drives employ a rotary actuator to move the read/write head in the radial direction of the magnetic disk. A typical current rotary actuator for a 3.5” disk drive causes the read/write heads to have a skew angle variation of 30°. The skew angle is the angle between slider’s longitudinal axis and track direction, termed

"geometric skew angle" (Liu and Soh, 1996). A large skew actuation will affect the slider's flying performance and off-track capability (Liu and Soh, 1996; Wiesen, et al., 1993; Hu, et al., 1996), causing an increase in side reading and an offset of written transitions from track center (Wei, et al., 1998). This complicates the position error signal (PES) calibration process in the HDD servo loop, as well as the self-servo track writing process. In a recent development in perpendicular magnetic recording, an involved read sensor pole trimming is necessary to relax the side reading effect due to skew angle variation (Wood, 2001; Lambert, et al., 2001; Kryder and Gustafson, 2004).

Previously, IBM proposed a parallel flexural in-line actuator for magnetic recording disk drives which has a small skew actuation (Chainer, et al., 1991). However, this design makes a significant change in the actuator structure compared to current ball bearing actuator designs. Also, it exhibits the first lateral resonance frequency of 1.5 kHz, which limits the achievable servo bandwidth. Toshiba researchers proposed a magnetic disk drive with an increased actuator arm length to achieve a small skew angle change (US Patent 6,021,024, 2000).

This chapter discusses the performance analysis and optimization of a magnetic disk drive actuator and head suspension designed to achieve a small skew actuation by extending the VCM arm length and slanting the suspension. Modal analysis using finite element modeling is performed to study the dynamic characteristics of the actuator with and without a slant angle. Experimental measurements along the actuator tracking direction are performed on the prototypes of the two actuator-structures to get a comparison of the dynamic performance.

5.2 Actuator assembly with small skew

Figure 5.1 shows the schematic of a simplified disk drive assembly with an increased actuator arm length. Typically, the slider's longitudinal direction coincides with the suspension's longitudinal direction. As shown in Figure 5.1, the skew angle is calculated by,

$$\theta = \sin^{-1}\left(\left(L^2 + r^2 - D^2\right)/2Lr\right) \tag{5.1}$$

where L is the arm length (the distance from the actuator pivot center to the head element), D is the distance between the pivot center and the spindle center, and r is the radius of the head element to the spindle center. The skew angle range versus the ratio of arm length to distance between the actuator pivot center and spindle center is shown in Figure 5.2. As can be seen from the figure, the minimum skew angle range is less than 4 degrees when the arm length ratio is around 1.11.

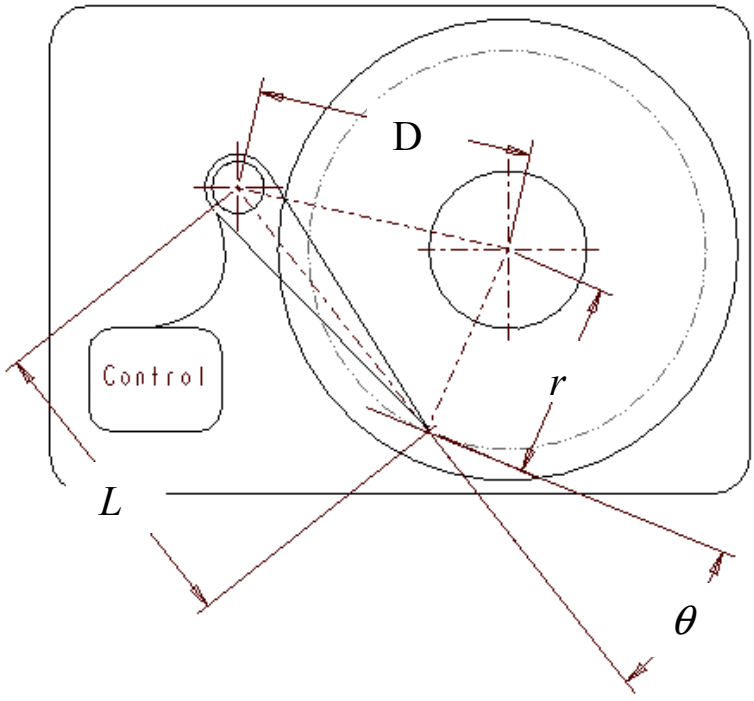

Figure 5.1: Optimization of arm length with minimum skew angle range.

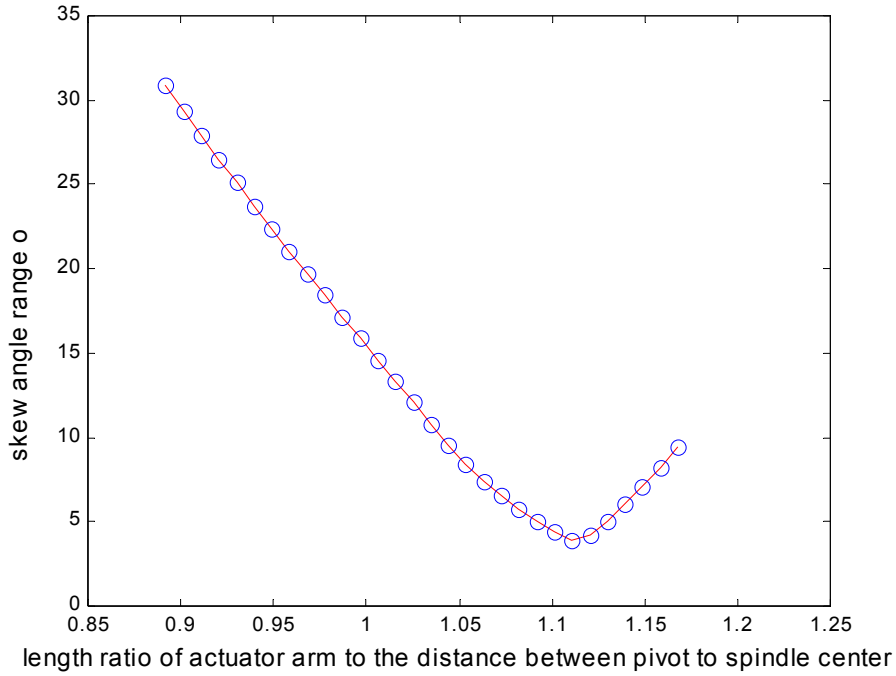

Figure 5.2: Skew angle range versus different arm length ratio.

Next, we slant the actuator arm assembly, i.e., we slant the suspension head assembly at an angle β with respect to the arm's longitudinal direction to obtain small skew actuation (as shown in Figure 5.3). β can be optimized so that the absolute skew angle of the actuator assembly is minimal, determined by

$$\beta = \cos^{-1}\left(\left(L_o^{\,2} - L_a^{\,2} - L_s^{\,2}\right)/\,2L_aL_s\right) \tag{5.2}$$

where L_o is optimal distance between the actuator pivot center and the head element which corresponds to minimal skew angle range, L_a is the arm length (the distance from the actuator pivot center to arm tip ball swaging center), and L_s is the suspension length (the distance from arm tip ball swaging center to the head element). As shown in Figure 5.4, the skew angle, θ_1, in a slanting suspension structure can be calculated by equation (5.3).

$$\theta_1 = 90^\circ - \angle ACO - \angle BCA = 90^\circ - \cos^{-1}\left[\frac{L_s^2 + L_0^2 - L_a^2}{2 \times L_s \times L_0}\right] - \cos^{-1}\left[\frac{L_0^2 + r^2 - D^2}{2 \times L_0 \times r}\right] \quad (5.3)$$

As the suspension length L_s is fixed, the slant angle β, will depend on the actual arm length, L_a, as expressed as equation (5.2). We optimize the arm length, L_a, such that the absolute skew angles from the inner diameter to outer diameter, are within ±2°. In the computation, the parameters used in skew angle calculating are measured and obtained as: the distance from the pivot center to the spindle center for 3.5" disk drive as, D=57.8mm; the suspension length, L_s =18.05mm; the optimized distance from the pivot center to the magnetic head, L_o=64.3mm; the radius in the inner diameter, r_{id} = 16.5 mm; the radius in the outer diameter, r_{od}=47mm. The optimized arm length is obtained as, L_a = 49.1 mm, while the slant angle β is calculated as 37.9°.

Figure 5.5 shows the skew angle ranges of a typical 3.5" drive actuator and the actuator assembly with slant suspension. It can be seen that the minimal skew angle in a HDD actuator assembly with slanting the suspension can be as low as ± 2º.

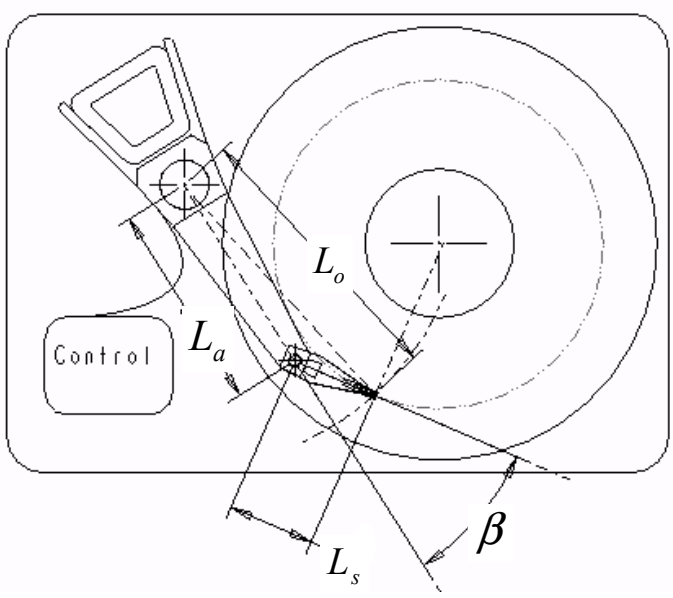

Figure 5.3: Magnetic disk drive actuator assembly with small skew.

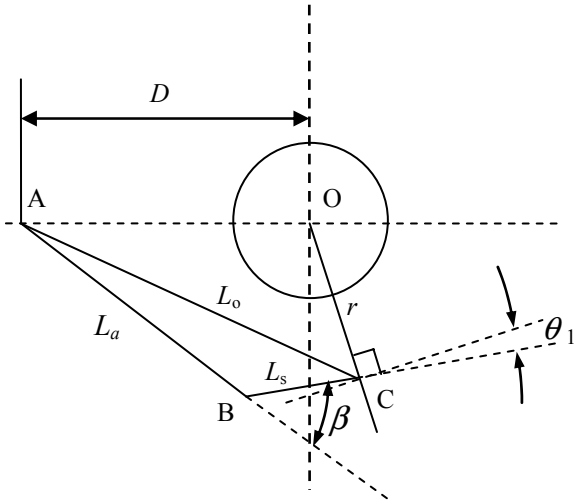

Figure 5.4: A schematic for calculating skew angle.

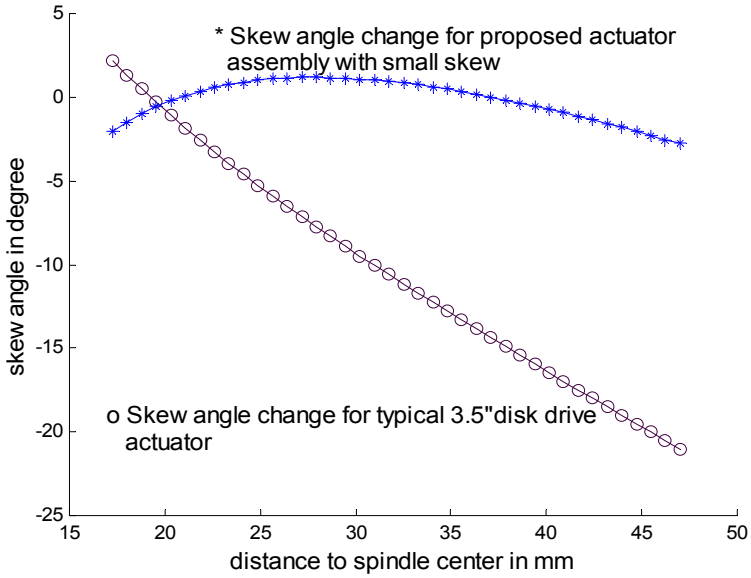

Figure 5.5: Skew angles for a typical 3.5" disk drive actuator and the actuator for small skew.

5.3 Performance evaluation

The dynamic characteristics (modal shapes) of a typical actuator with straight suspension assembly and the actuator with slant suspension assembly are analyzed using finite element methods.

Figure 5.6 shows the finite element meshes. In the simulation, a dummy suspension of thin stainless steel sheet is attached to the actuator arm tip. The resonance frequencies of different vibration modes are listed in Table 5.1. The resonance frequencies of the various modes for the actuator with slant suspension assembly are not significantly different from those of the actuator with straight suspension assembly.

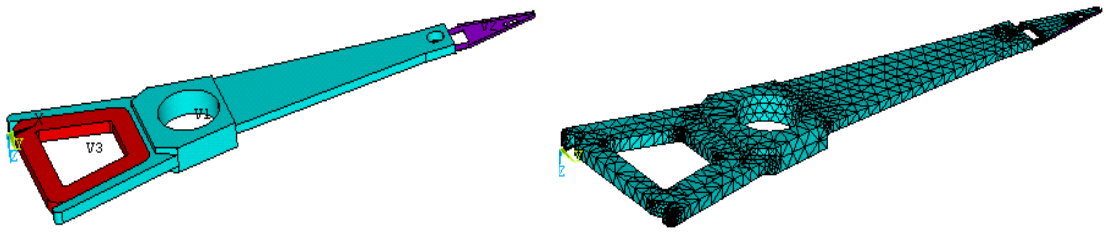

a. Finite element modeling without slanting suspension

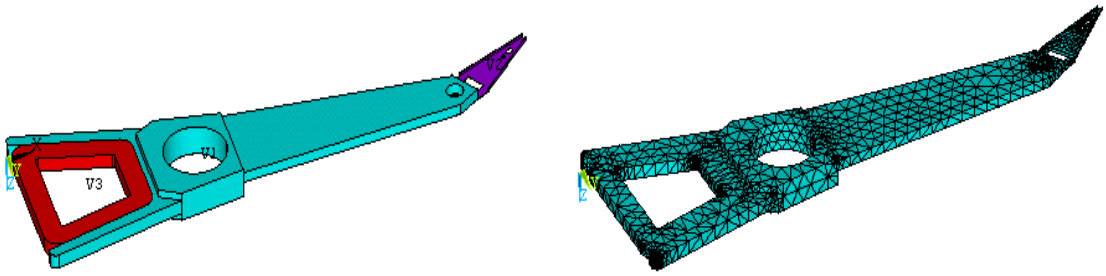

b. Finite element modeling with slanting the suspension

Figure 5.6: Finite element models of actuator assemblies with and without slant angle.

A prototype made of a typical 3.5” disk drive actuator arm and suspension for the actuator with straight and slant suspensions is shown in Figure 5.7. The measured frequency response of the prototype is shown in Figure 5.8. The small resonance peak at 2.5 kHz is the torsion mode of the suspension. The slight difference for the actuator assembly with straight suspension and slant suspension may be due to structural differences at the gluing point between the suspension and the arm tip. In addition, flight performance during the experiment may also affect the results.

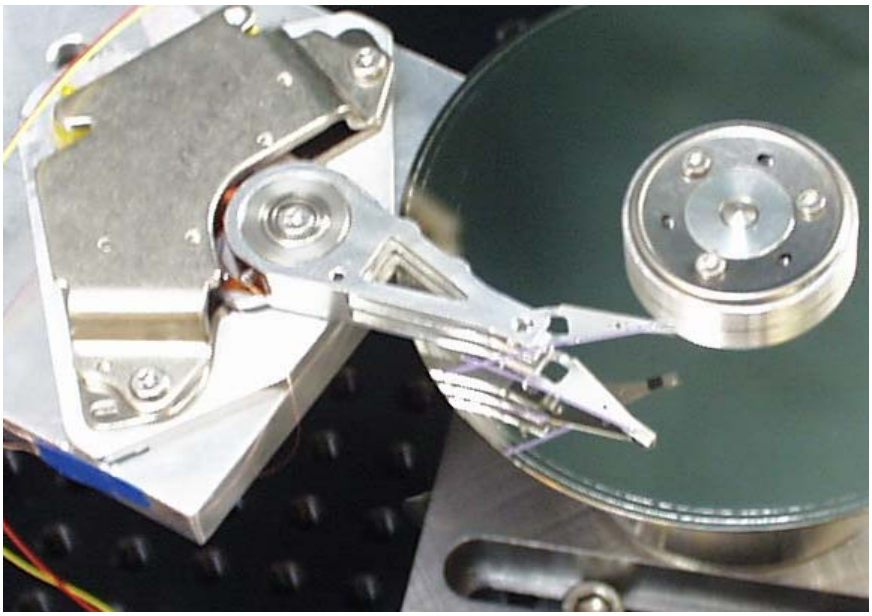

Figure 5.7: Actuator assemblies with and without slant angle

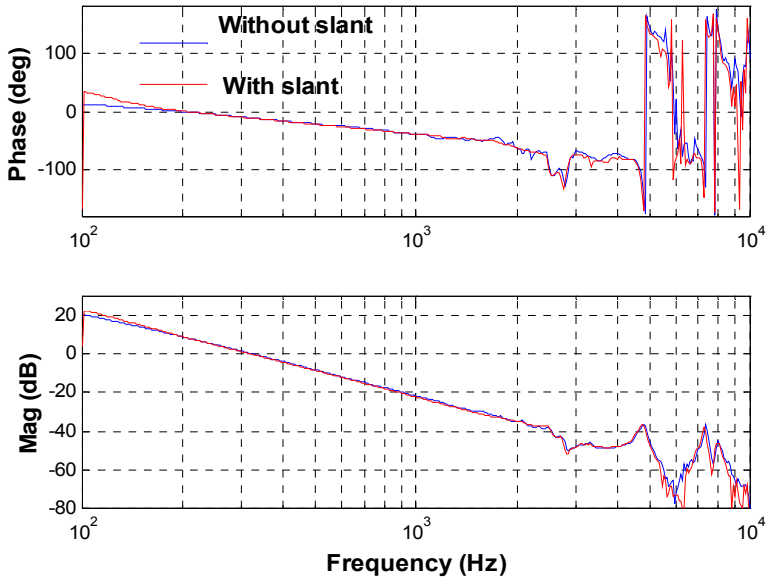

Figure 5.8: Frequency responses of actuator assemblies with and without slant angle

Table 5.1: Resonance frequencies of actuator assemblies with and without a slant angle.

Mode Shapes (kHz)	Actuator assembly without slant angle	Actuator assembly with slant angle
Suspension out of plane bending	0.24	0.24
Arm + suspension out of plane bending	0.89	0.92
Coil out of plane bending	2.67	2.67
Suspension torsion	2.80	2.86
Suspension second out of plane bending	3.45	3.51
Coil torsion	4.43	5.53
Arm + suspension second out-of-plane bending	4.93	4.86
Arm sway	6.07	5.97
Arm torsion + suspension second torsion	7.47	8.10
Suspension third torsion	8.30	8.48

We note here that even if there is no significant change of the resonance frequency for the slant suspension assembly compared to the straight suspension assembly, the length ratio for a minimal skew range has been increased to 1.11 from about 0.93 in the current actuator assembly. This causes the resonance frequency for the arm sway mode to drop 20~30% from the conventional design. A small skew actuator design, which does not sacrifice bandwidth, is called for. Possible remedies are: (1) reducing the actuator mass, (2) specifying the proper suspension to arm length ratio, (3)

designing high bandwidth VCM arm and suspension structures, and so on (Lin, et al., 2001; Health, 2000). In addition, introducing a secondary stage actuator for dual stage control of the head element is one possible means to increase the actuator servo bandwidth (Guo, et al., 2001; He, et al., 1999). Furthermore, reducing vibration due to air flow, spindle motor, disk, etc., can relax the requirements on servo bandwidth (Ong, et al., 2000).

5.4 Conclusions

This chapter shows that a disk drive actuator can be designed with a skew angle of ±2 degrees by extending the actuator arm length to a certain point and slanting the suspension or head assembly. There is no significant change in the dynamic performance for the actuator from slanting the suspension.

CHAPTER 6

DYNAMICS MODELING OF A PIEZOELECTRIC SUSPENSION FOR MAGNETIC RECORDING

This chapter describes the fundamentals of piezoelectric micro actuators and presents a split electrodes piezoelectric micro actuator for use in disk drive head suspension structure. A piezoelectric suspension based on the piezoelectric micro actuator structure is presented. The dynamic behaviors of the micro actuator are investigated and the actuator shape is optimized using an analytical method. The static and dynamic behaviors of the piezoelectric suspension structure for high track density magnetic recording systems are investigated by finite element method (FEM). Based upon the analyses of piezoelectric actuators, the optimization of piezoelectric suspension is conducted to achieve a high resonance frequency of sway mode and large displacement sensitivity. The finite element simulation results on a planar piezoelectric suspension agree quite well with the experimental measurements using a Laser Doppler Vibrometer (LDV). The optimized piezoelectric suspension demonstrates better performances than those of the planar piezoelectric suspension.

6.1 Introduction

As described in Chapter 1, the main obstacle to increasing the track density is inadequate head positioning accuracy, which mainly depends on the mechanical and servo performance of read/write systems of the hard disk drive. With the requirements of accurate read/write data of magnetic recording, the maximum tolerable offset between the R/W head and the track center is less than 10% of the track pitch. It is

estimated that a drive spinning at 7,200 rpm supporting the above track density would require a servo bandwidth of about 2~3 kHz (Guo, et al., 1998). To achieve such high track density, one solution that can suppress the disturbances and provide high bandwidth tracking ability is by using a dual-stage servo system, that is, a voice coil motor (VCM) as the primary stage and a micro-actuator as the secondary stage. As a functional material, piezoelectric ceramics can play the role of a micro-actuator. A design of a planar piezoelectric actuator made of piezoelectric ceramic sheet and the design of piezoelectric suspension with a part of load beam replaced by the planar piezoelectric actuator were presented by Guo, et al. (1998). The design has a simple structure and low cost. The experimental study on the piezoelectric actuator and the suspension shows that the frequency response and displacement output can satisfy the requirements for dual-stage servo system.

In the current study, finite element method (FEM) was employed to further investigate the static and dynamic performances of the planar piezoelectric suspension. Up until now, some studies on a conventional suspension by finite element method have been carried out (Jeans, 1992; Watanabe, et al., 1997). All the previous work provides valuable information for the current finite element modeling on the piezoelectric suspension. Hutchinson-850, a type of conventional suspension (Hutchinson, 1995), was modeled and investigated. Finite element analyses were also performed on the planar piezoelectric suspension. A good agreement exists between the finite element analysis and the experimental investigation made by Guo, et al. (1998).

The study reveals that the planar piezoelectric suspension has a good displacement sensitivity and high resonance frequency of sway mode. Moreover, by optimizing the

shape and dimensions of the piezoelectric actuator, the optimal performances can be achieved. Based on theoretical analyses of the planar piezoelectric actuator, finite element analyses are conducted to optimize the assembly of the planar piezoelectric actuator with the suspension. The objective of the optimization is to improve the resonance frequency of sway mode and the displacement sensitivity of the suspension. An optimized design of the piezoelectric suspension is presented.

6.2 Basic piezoelectricity

The word "piezo" is derived from the Greek word for pressure. In 1880, Jacques and Pierre Curie discovered that pressure applied to a quartz crystal creates an electrical charge in the crystal. They called the phenomena the piezo effect. Later they also verified that an electrical field applied to the crystal would lead to a deformation of the material. This effect is referred to as the inverse piezo effect. After the discovery it took several decades to utilize the piezoelectric phenomenon. As stated above, piezoelectric materials can be used to convert electrical energy into mechanical energy and vice versa. For micro-positioning, precise motion will result when an electric field is applied to a piezoelectric material. Actuators using this effect became available and have changed the world of precision positioning.

For a solid piezoelectric ceramic, the constitutive equation for piezoelectric ceramic can be written as:

$$\{\sigma\} = [C]\{\varepsilon\} - [e_e]^T \{E_e\} \tag{6.1}$$

$$\{D\} = [e_e]\{\varepsilon\} + [g]\{E_e\} \tag{6.2}$$

$\{D\}$, $\{E_e\}$, $\{\sigma\}$, $\{e_e\}$, are electric displacement, electric field, stress and strain vectors respectively. $[C]$, $[e_e]$, and $[g]$ are elastic constant, piezoelectric constant and dielectric constant respectively. For homogenous piezoelectric ceramic, while the polarized direction in z direction, $[C]$, $[e_e]$, and $[g]$ can be further written as:

$$[C]=\begin{bmatrix} c_{11} & c_{12} & c_{13} & 0 & 0 & 0 \\ c_{12} & c_{22} & c_{23} & 0 & 0 & 0 \\ c_{13} & c_{23} & c_{33} & 0 & 0 & 0 \\ 0 & 0 & 0 & c_{44} & 0 & 0 \\ 0 & 0 & 0 & 0 & c_{55} & 0 \\ 0 & 0 & 0 & 0 & 0 & c_{66} \end{bmatrix} \qquad [g]=\begin{bmatrix} g_{11} & 0 & 0 \\ 0 & g_{22} & 0 \\ 0 & 0 & g_{33} \end{bmatrix} \tag{6.3}$$

$$[e_e]=\begin{bmatrix} 0 & 0 & 0 & 0 & e_{15} & 0 \\ 0 & 0 & 0 & e_{24} & 0 & 0 \\ e_{31} & e_{32} & e_{33} & 0 & 0 & 0 \end{bmatrix} \tag{6.4}$$

The widely used piezoelectric actuator modes include d_{31}, d_{33} (as shown in Figure 6.1) and shear d_{51}. In d_{31} mode, electric field points in the same direction as the polarized direction (along axis 3), resulting a motion along axis 1; while in d_{33} mode, electric field points in the same direction as the polarized direction (along axis 3), resulting a motion also along axis 3. Figure 6.2 shows the d_{51} mode that electric field is applied perpendicular to polarization vector, resulting in a shear deformation about the axis perpendicular to both polarized direction and electric field.

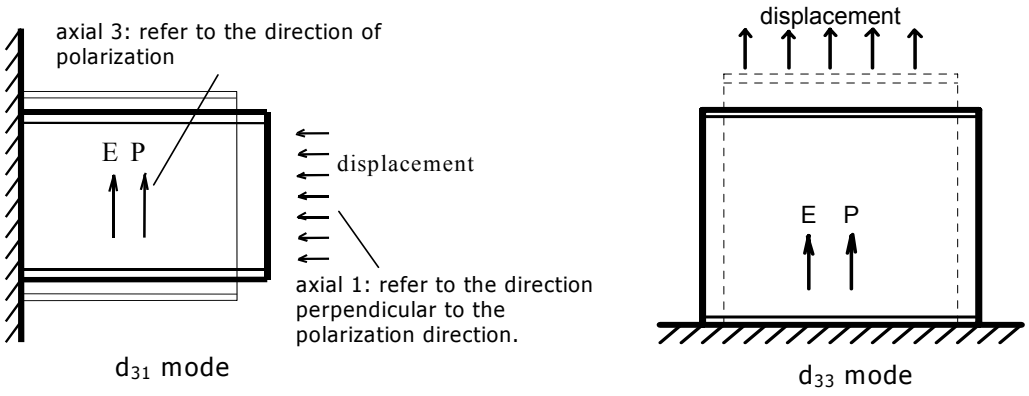

Figure 6.1: d_{31} and d_{33} modes of piezoelectric actuators.

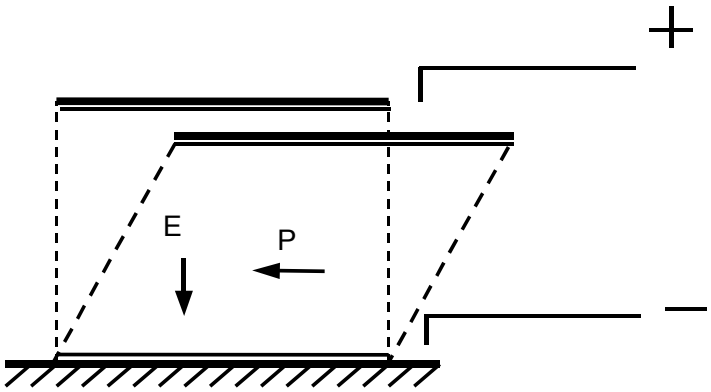

Figure 6.2: Shear mode (d_{51}) of piezoelectricity.

6.3 The planar piezoelectric actuator/suspension with split electrodes

Figure 6.3 illustrates the basic structure of a planar piezoelectric actuator. It is a single piece of rectangular piezoelectric ceramic sheet polarized in the direction of its thickness and "d_{31}" operation mode is used. The upper and lower electrodes are split into two separate symmetric parts, between which there is one crevice where no electrode is applied on the piezoelectric sheet. This kind of piezoelectric ceramics sheet can generate an in-plane displacement at a proper driving voltage. As shown in Figure 6.3, under a given voltage, one half, A, of the actuator will expand while the other half, B, will contract. Thus, if one end of the actuator is clamped onto a base, the deflection of the other end will be along the y-direction. Because the stiffness of the piezoelectric actuator in y-direction is very high, a high resonance frequency in y-direction is expected. The displacement sensitivity and resonance frequency of the actuator can be controlled by changing its shapes and dimensions.

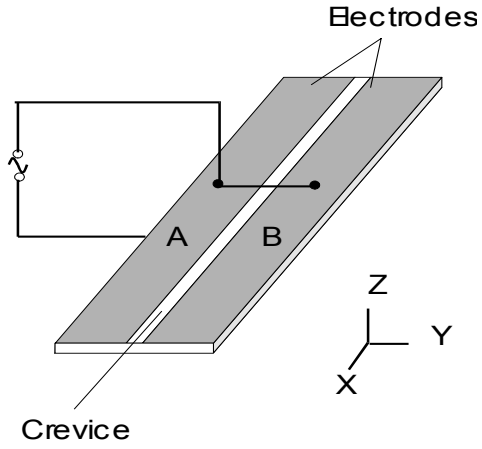

Figure 6.3: High bandwidth planar piezoelectric actuator.

In order to meet the head/media interface requirements and obtain a high servo bandwidth, the suspension and the gimbal assembly should be relatively soft in the vertical, pitch and roll directions and stiff in the in-plane direction. In a hard disk servomechanism, the driving direction of the secondary actuator should be in the track seeking/following direction. As described above, the planar piezoelectric actuator possesses this property so that it can be used to form a piezoelectric suspension. The planar piezoelectric suspension is shown in Figure 6.4. The planar piezoelectric actuator is attached on the load beam of the conventional suspension (Hutchinson TSA850, 1995), and the slider with gimbal assembly (HGA) is directly attached to the tip of the actuator. The attachment is achieved with a kind of epoxy resin. In this structure, the piezoelectric actuator can serve both as a part of the suspension to support the slider/head and a secondary actuator to provide rapid and accurate positioning to the read/write head in y-direction. In the prototype of the planar piezoelectric suspension, the dimensions of the piezoelectric actuator are 11×5×0.2 mm and the measured thickness of the epoxy resin is 0.15 mm.

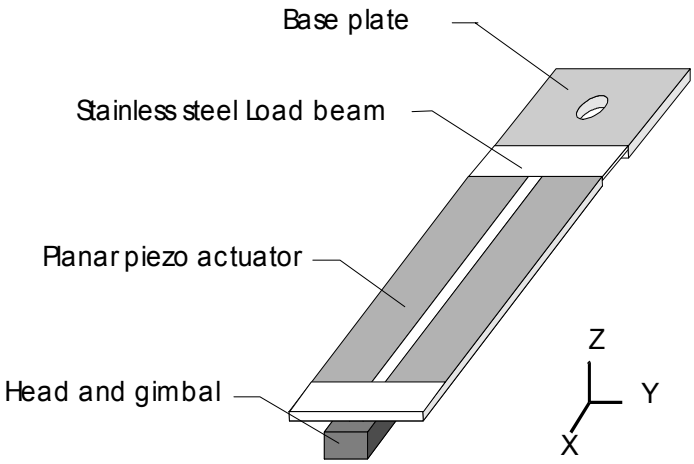

Figure 6.4: Suspension made of a planar piezoelectric actuator.

6.4 Dynamic and deflection analysis of split electrodes piezoelectric actuators

6.4.1 Natural frequency of the split electrodes piezoelectric actuators

A piezoelectric micro actuator used in disk drive servo mechanical system is used as dual stage servo. As it works in a high frequency range, its natural frequency must be as high as possible so that the servo bandwidth can be enhanced. Therefore the dynamic analysis of piezoelectric micro actuator is necessary. A split electrodes piezoelectric actuator with variable cross section as shown in Figure 6.5 can be considered as a cantilever beam. Its equation of motion (neglecting damping) is:

$$\frac{\partial}{\partial x}\left[J(x)\frac{\partial^2 y(x,t)}{\partial t^2 \partial x}\right] = \frac{\partial^2}{\partial x^2}\left[E_Y I(x)\frac{\partial^2 y(x,t)}{\partial x^2}\right] + \mu(x)\frac{\partial^2 y(x,t)}{\partial t^2} - p(x,t) \qquad (6.5)$$

where, $\mu(x)$ is the density per unit length. If the material density is ρ, the cross section area is $A(x)$, then $\mu(x)= \rho A(x)$. $E_Y I(x)$ is the bending modulus. $J(x)$ is moment of inertia along the axis which is perpendicular to the vibration plane and parallel to the z axis. $p(x, t)$ is the distribution load applied on the beam. If we consider a slander beam, the

rotational moment of inertia $J(x)$ can be neglected. Further we let $p(x, t)=0$, then the equation of motion can be written as

$$\frac{\partial^2}{\partial x^2}\left[E_Y I \frac{\partial^2 y(x,t)}{\partial x^2} \right] + \mu \frac{\partial^2 y(x,t)}{\partial t^2} = 0 \tag{6.6}$$

It is difficult to find the analytical solutions for equation (6.6). However, an approximate method, such as Ritz method, can be used to estimate the natural frequencies of the beam structure. The resonance frequencies of several typical shapes of the actuator structure, namely, triangular, trapezoidal, and rectangular actuators have been discussed by Wang (1997).

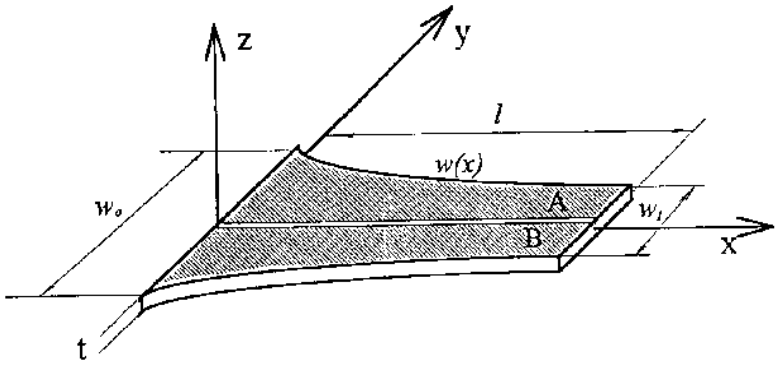

Figure 6.5: Split piezoelectric actuator with variable cross section.

Figure 6.6 shows a trapezoidal piezoelectric actuator. The width of the cross section $w(x)$, moment of inertia $I(x)$ and the mass per unit length $\mu(x)$ can be written respectively as,

$$w(x) = w_0(1 - a\frac{x}{l}) \tag{6.7}$$

$$I(x) = \frac{t w_0^{\,3}}{12}(1 - a\frac{x}{l})^3 = I_0(1 - a\frac{x}{l})^3 \tag{6.8}$$

$$\mu(x) = \rho w(x)t = \rho w_0 t(1 - a\frac{x}{l}) = \mu_0(1 - a\frac{x}{l}) \tag{6.9}$$

where, $a = (w_0 - w_1)/w_0$, t is the thickness the split actuator, I_0 and μ_0 are the inertia of moment and the mass per unit length at the fixed end of the actuator.

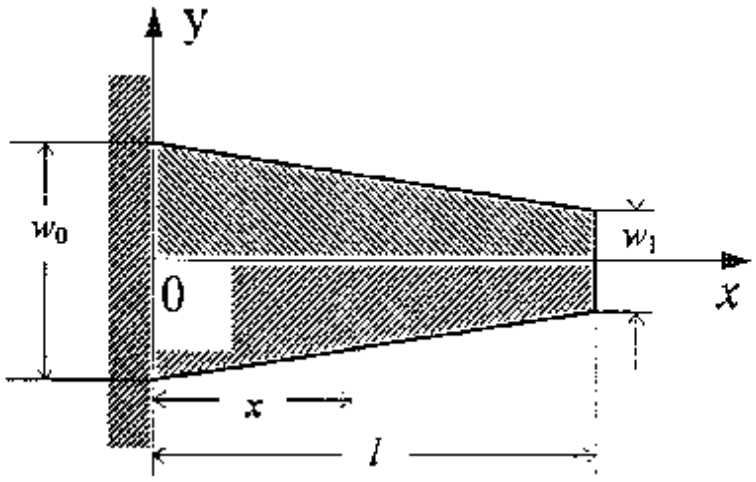

Figure 6.6: Trapezoidal piezoelectric actuator.

The Rayleigh-Ritz method (Reddy, 1999) is used to calculate the natural frequencies of the actuator structure. A trial function is selected to satisfy the geometrical boundary condition. The trial function is as

$$Y(x) = a_1 x^2 + a_2 x^3 \tag{6.10}$$

Obviously it satisfies the geometrical boundary condition, i.e., at x=0, there are $Y(0)$=0, and $Y'(0)$=0. By equation (6.6), therefore the equation to calculate the resonance frequency can be written as

$$A\omega^4 + B\omega^2 + C = 0 \tag{6.11}$$

where,

$$A = (\frac{1}{5} - \frac{a}{6})(\frac{1}{7} - \frac{a}{8}) - (\frac{1}{6} - \frac{a}{7})^2$$

$$B = -\frac{E_Y I_0}{\mu_0 l^4}[4(1-\frac{3a}{2}+a^2-\frac{a^3}{4})(\frac{1}{7}-\frac{a}{8})+36(\frac{1}{3}-\frac{3a}{4}+\frac{3a^2}{5}-\frac{a^3}{6})$$
$$-24(\frac{1}{2}-a+\frac{3a^2}{4}-\frac{a^3}{5})(\frac{1}{6}-\frac{a}{7})]$$
$$C = 144(\frac{E_Y I_0}{\mu_0 l^4})[(1-\frac{3a}{2}+a^2-\frac{a^3}{4})(\frac{1}{3}-\frac{3a}{4}+\frac{3a^2}{5}-\frac{a^3}{6})-(\frac{1}{2}-a+\frac{3a^2}{4}-\frac{a^3}{5})^2]$$

Rectangular piezoelectric actuator

While *a*=0, the trapezoidal actuator becomes a rectangular actuator as shown in Figure 6.3. Equation (6.11) becomes as

$$\omega^4 - 1224\frac{E_Y I_0}{\mu_0 l^4}\omega^2 + 15120(\frac{E_Y I_0}{\mu_0 l^4})^2 = 0 \tag{6.12}$$

The first two solutions of the equation (6.12) are as

$$\omega_1 = \frac{3.533}{l^2}\sqrt{\frac{E_Y I_0}{\mu_0}} \tag{6.13}$$

$$\omega_2 = \frac{34.81}{l^2}\sqrt{\frac{E_Y I_0}{\mu_0}} \tag{6.14}$$

Triangular piezoelectric actuator

While *a*=1, the trapezoidal actuator becomes a triangular actuator as shown in Figure 6.7. Equation (6.11) becomes

$$\omega^4 - 327.61\frac{E_Y I_0}{\mu_0 l^4}\omega^2 + 8467.40(\frac{E_Y I_0}{\mu_0 l^4})^2 = 0 \tag{6.15}$$

The first two solutions of above equation are as:

$$\omega_1 = \frac{5.319}{l^2}\sqrt{\frac{E_Y I_0}{\mu_0}} \tag{6.16}$$

$$\omega_1 = \frac{17.30}{l^2}\sqrt{\frac{E_Y I_0}{\mu_0}} \tag{6.17}$$

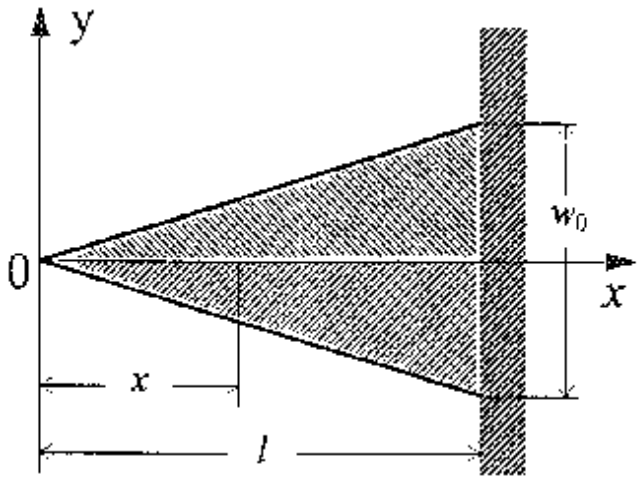

Figure 6.7: Triangular piezoelectric actuator.

The first natural frequency ω_1 is the dominant contributor to the servo bandwidth of actuator servo bandwidth. Generally we can discuss the relationship between ω_1 and the shape factor a. Therefore we write the first natural frequency ω_1 as

$$\omega_1 = \frac{k_1}{l^2}\sqrt{\frac{E_Y I_0}{\mu_0}} \tag{6.18}$$

k_1 is the constant determined by a. Figure 6.8 shows the relationship curve between k_1 and a. It can be seen that by increasing a, the first order natural frequency increases. That means the servo bandwidth of the actuator increases with increasing a. The servo bandwidth of the triangular actuator is about 1.5 times of that a rectangular actuator, i.e., 5.319/3.533=1.5.

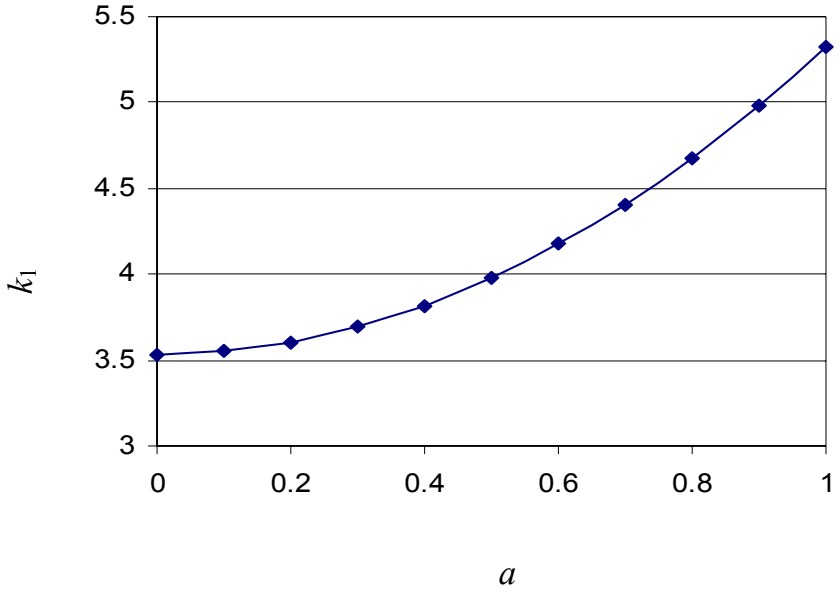

Figure 6.8: The relationship curve between k_1 ($\omega_1 = k_1 / l^2 \sqrt{E_Y I_0 / \mu_0}$) and a ($a = (w_0 - w_1)/w_0$).

6.4.2 Static deflection of split electrodes piezoelectric actuators

Wang (1997) provides the analytical solutions of the deflections at the free ends of split electrodes piezoelectric actuators with some types of shape, i.e. rectangular, trapezoidal and triangular shapes. The solutions are listed as

Rectangular actuator:

$$\delta = 3d_{31}E_3 l^2 / 2w_0 \tag{6.19}$$

Triangular actuator:

$$\delta = 3d_{31}E_3 l^2 / w_0 \tag{6.20}$$

Trapezoidal actuator:

$$\delta = \frac{3d_{31}E_3 l^2 w_1}{(w_0 - w_1)^2}\left(\ln\frac{w_1}{w_0} + \frac{w_0}{w_1} - 1\right) \tag{6.21}$$

Where E_3 is the external electric field imposed to the piezoelectric actuators. Generally we can write the deflection expression as:

$$\delta = k_2 d_{31} E_3 \frac{l^2}{w_0} \tag{6.22}$$

where k_2 is the constant determined by the actuator shape. Figure 6.9 shows the relationship curve between k_2 and a. It can be seen that with increasing a, the deflection of the free end at an applied electric field increases. The deflection at the free end of a triangular actuator is about 2 times of that a rectangular actuator.

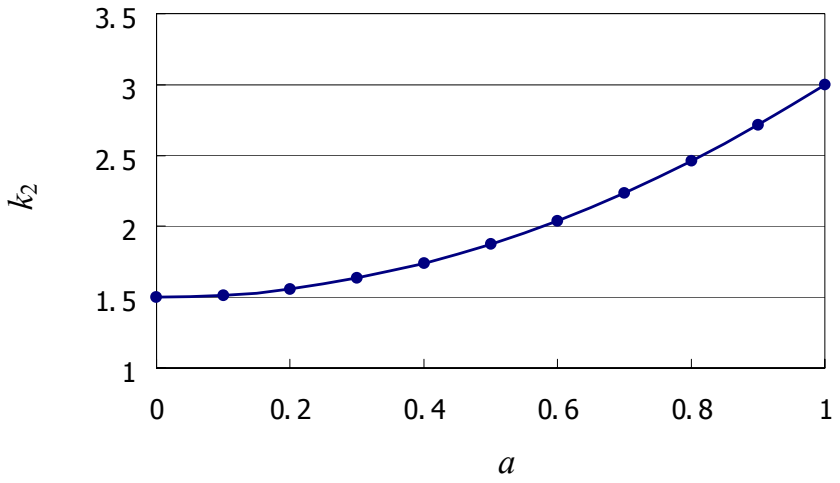

Figure 6.9: The relationship curve between k_2 ($\delta = k_2 d_{31} E_3 l^2 / w_0$) and a ($a = (w_0 - w_1)/w_0$).

6.5 Experimental investigation of the dynamics of piezoelectric micro actuators and suspensions

The dynamic frequency response of piezoelectric micro actuator and suspensions can be experimentally investigated using a Laser Doppler Vibrometer (LDV) and a dynamic signal analyzer (DSA). Figure 6.10 shows the experiment setup. The source excitation signal at a specified frequency sweep range is generated by DSA and sent to

the piezoelectric micro actuator through a piezoelectric-amplifier. The laser signal generated and received by LDV will sense the vibration characteristics of the actuator/suspension measurement points and send the signal back to DSA for analyses and demonstration.

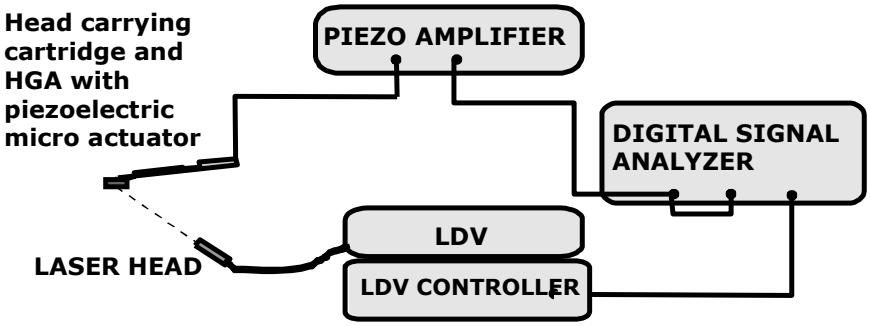

PIEZO AMPLIFIER: PIEZO SYSTEM. 60.102
LDV: VIBROMETER CONTROLLER POLYTEC OFV3001
FIBER INTERFEROMETER POLYTEC OFV502
DIGITAL SIGNAL ANALYZER: HP DSA 35670A

Figure 6.10: Experimental setup of dynamic frequency response measurement of piezoelectric micro actuator and suspension.

The prototype of the piezoelectric micro actuator and the suspension are shown in Figure 6.11. The measurement is along the head seeking/tracking direction, as the dynamic resonance characteristics along the head positioning direction is the concern in the investigation. Figure 6.12 shows the displacement output of the piezoelectric suspension. With a ±20volts sine wave voltage at 1KHz, the displacement output on the slider is about ±1.0μm. Figure 6.13 shows the measured velocity frequency response of the planar piezoelectric actuator with its one end fixed on a heavy base. The measurement is taken along the seeking/tracking direction at the free end of the actuator. The resonance frequency of the in-plane sway mode is about 9.5 kHz. Figure 6.14 illustrates the measured velocity frequency response of the planar piezoelectric suspension with its base plate fixed. The slider flies over the rotating disk surface with

a proper air bearing created between the slider and the disk surface. At 2.1 kHz, there is one small resonance peak, which is probably caused by the resonance of the slider and gimbal. A pair of resonance peaks and valleys occurs at 6.3 kHz and 10.6 kHz respectively, which result in phase shift about 180°. Comparing Figure 6.13 with Figure 6.14, the dominant resonance frequency of the piezoelectric suspension is reduced by about 3 kHz. This is due to an additional mass, i.e., part of the suspension load beam, gimbal and slider being added to the free end of the actuators and the fixed end of the piezoelectric micro actuator being connected to suspension load beam other than being connected to a rigid base. From the structure and the testing results, the planar piezoelectric suspension can be used as a dual-stage actuator for fine positioning of the magnetic head with its dominant resonance peak compensated by a notch filter.

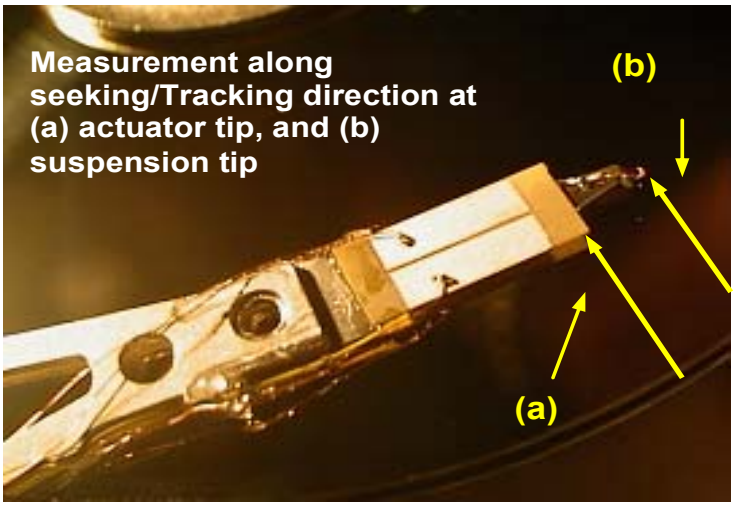

Figure 6.11: Prototyping of piezoelectric micro actuator and suspension, and the measurement directions.

The linearity response of the piezoelectric suspension is experimentally investigated. Generally piezoelectric actuators demonstrate non-linearality as a hysterisis loop. The

measured hysterisis loop of the prototyped piezoelectric suspension at the suspension slider tip is shown in Figure 6.15. The result agrees with the simulation that displacement sensitivity is about 0.051 μm/V.

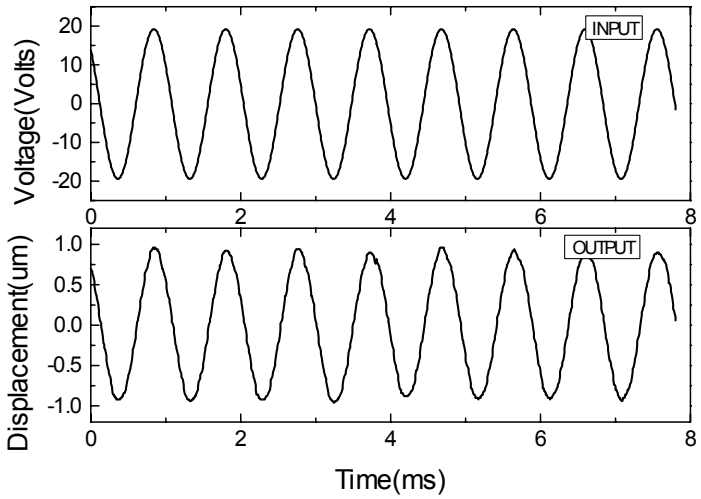

Figure 6.12: Displacement output of the piezoelectric suspension.

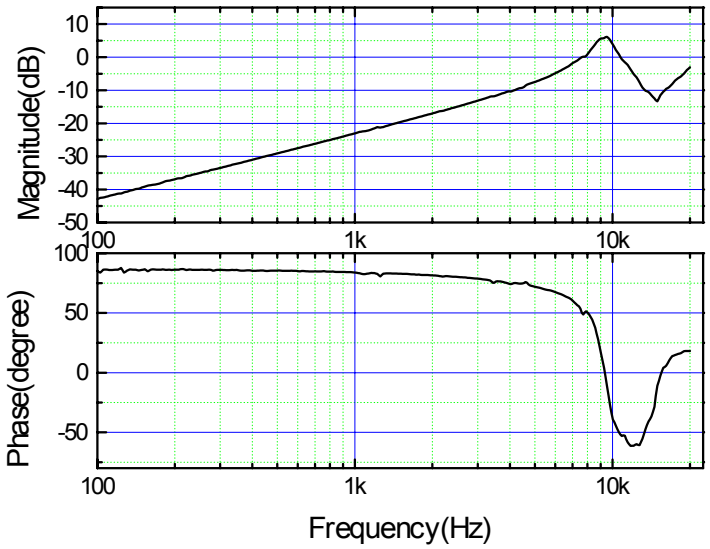

Figure 6.13: Frequency response of the planar piezoelectric actuator.

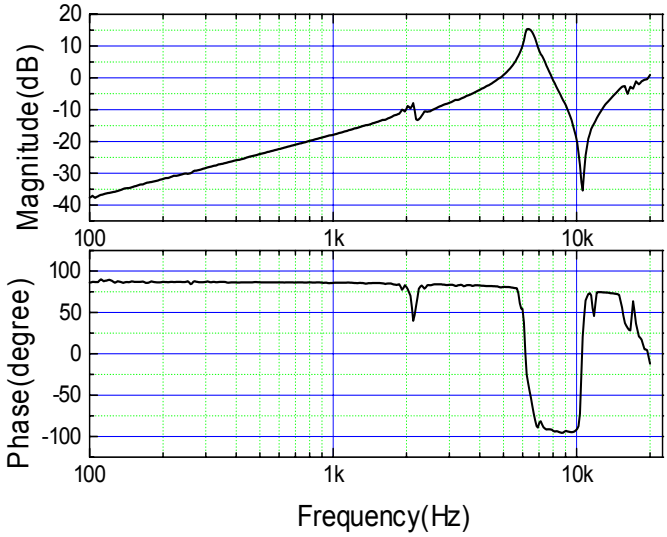

Figure 6.14**:** Frequency response of the piezoelectric suspension.

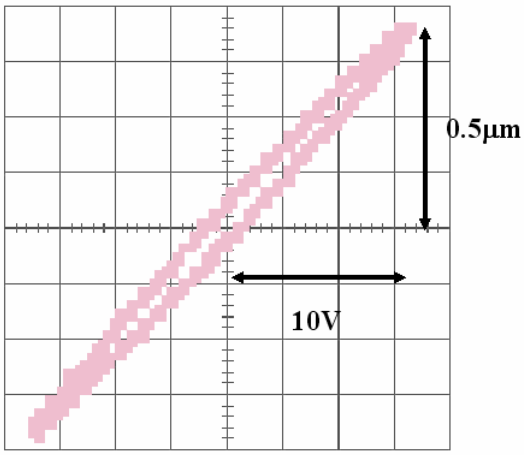

Figure 6.15: The hysterisis loop of the planar piezoelectric suspension.

6.6 Finite element simulation on conventional and the planar piezoelectric suspensions

6.6.1 Conventional suspension

In this study, finite element analyses are performed using the software ABAQUS. The choice of the software is due to the fact that ABAQUS provides a convenient tool to analyze piezoelectric behaviors of materials. Before the finite element modeling on the planar piezoelectric suspension, dynamic modal analyses of a conventional suspension

based on Hutchinson TSA850 is simulated using ABAQUS. The results obtained by finite element analyses show a close agreement with related data from the Hutchinson-850 data sheet (1995), as listed in Table 6.1. The FEM mesh is shown in Figure 6.16.

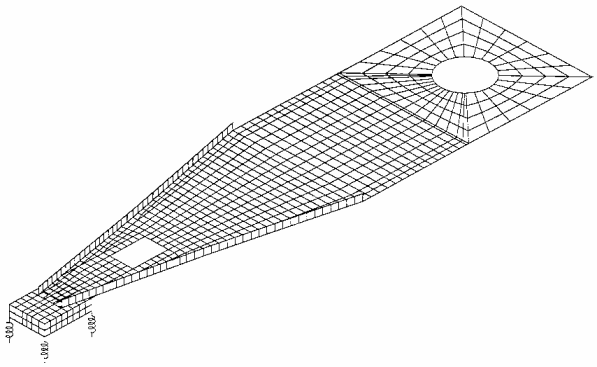

Figure 6.16: Finite element modeling of conventional suspension.

Table 6.1: Characteristics of a conventional suspension.

Natural Frequencies	By FEM Modeling	From Hutchinson 850
1st torsion (kHz)	2.63	2.4~2.8
2nd torsion (kHz)	6.59	6.2~8.0
Sway (kHz)	12.35	>11.0

6.6.2 Planar piezoelectric suspension

In the prototype, the piezoelectric actuator is connected to the suspension load beam by epoxy resin. Therefore, in the finite element modeling of the planar piezoelectric suspension, this effect should be accounted for. The thickness of the stainless steel load beam and the gimbal are 0.76 mm and 0.36 mm respectively and they are modeled by shell elements due to their very small thickness compared to overall dimensions in the lengthwise directions. The epoxy resin and the cermet (aluminum oxide titanium carbide) slider are modeled by 8-node hexahedron elements. The piezoelectric actuator

is modeled by 8-node hexahedron piezoelectric elements. The air bearing is modeled by four springs at the four corners of the slider. The stiffness of the four springs is 4×10^5 N/m, and a vertical displacement of 100 nm is induced to provide the same level of pre-loads as that of a conventional suspension. The base plate is constrained as if the suspension is mounted on the arm tip. The related material physical properties used in the model are listed in Table 6.2.

Table 6.2: Materials properties used in model

Material	Young's Modulus (N/m^2)	Density (kg/m^3)	Poisson's Ratio
Stainless steel	1.93×10^{11}	7800	0.30
Epoxy resin	2.50×10^{9}	1000	0.30
Cermet	1.38×10^{11}	3800	0.26

The density of the piezoelectric ceramics is 7800 $kg/m^{3.}$ Other related material physical properties in this study are listed in Tables 6.3 to 6.5. The finite element simulation includes modal and electrostatic analyses. The related resonance modes and the static deformation obtained by finite element analyses are shown in Figure 6.17. The characteristics of the planar piezoelectric are listed in Table 6.6. From the results listed in Table 6.1 and Table 6.6, the overall natural frequencies of the planar suspension are lower than those of the conventional suspension. This is due to the fact that the introduction of the piezoelectric actuator increases the total mass and decreases the stiffness of the suspension. The thickness of the piezoelectric actuator is 0.2 mm, much thicker than that of the load beam of 0.076 mm thick. The density of piezoelectric ceramics is in the same region as that of stainless steel. The elastic

modulus along the principal direction of the piezoelectric ceramics is about half of the steel. These factors cause the lower natural frequencies of the planar piezoelectric suspension compared to the conventional suspension.

Table 6.3: Elastic matrix of piezoelectric ceramics ($\times 10^9$ N/m^2).

91.6507	46.4019	41.8564	0	0	0
46.4019	91.6507	41.8564	0	0	0
41.8564	41.8564	78.5725	0	0	0
0	0	0	21.0526	0	0
0	0	0	0	21.0526	0
0	0	0	0	0	22.6244

Table 6.4: Piezoelectric coupling matrix (Coulomb/m^2).

0	0	-8.1201
0	0	-8.1201
0	0	14.7569
0	12.3158	0
12.3158	0	0
0	0	0

Table 6.5: Dielectric matrix ($\times 10^{-9}$ Farad/m).

11.3803	0	0
0	11.3803	0
0	0	7.6928

However, the planar piezoelectric suspension can still provide the resonance frequency of sway mode above 6 kHz, which still can be used to achieve the 2 ~3 kHz of servo control bandwidth in the read/write system of hard disk drive. Experimental

investigation (Guo, et al., 1998) revealed the sway mode frequency at 6.3 kHz, quite close to the results listed in Table 6.6. Electrostatic analysis by finite element method indicates that a 0.615 μm displacement along the *y*-direction on the slider is generated at a 12 volts driving voltage. This provides the displacement sensitivity of 0.051 μm/V. The static deformation of the planar piezoelectric suspension at the voltage of 12 volts is shown in Figure 6.17d.

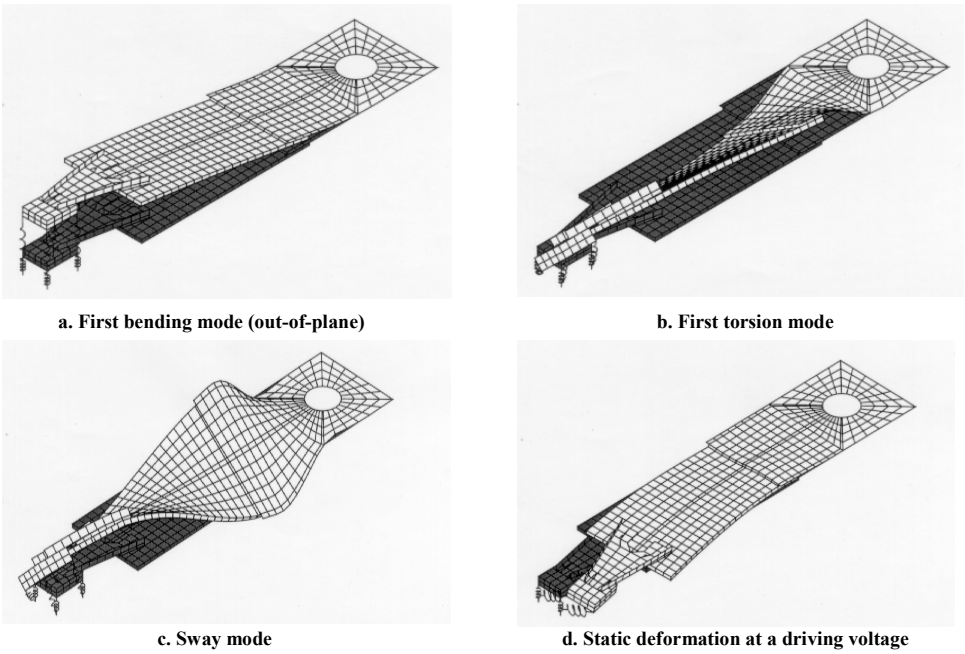

Figure 6.17: The finite element modeling and mode shapes of the planar piezoelectric suspension.

Table 6.6: Characteristics of planar piezoelectric suspension.

1st bending (kHz)	0.58
1st torsion (kHz)	1.93
Sway (kHz)	6.12
Displacement at 12 V (μm)	0.615
Sensitivity (μ m/V)	0.051

It should be pointed out that the epoxy resin also affects the natural frequencies and displacement sensitivity. The elastic modulus of the different epoxy resins range (1.50 ~ 3.50) $\times 10^9$ N/m^2. The simulated results for the planar piezoelectric suspension with different Young's modulus of the epoxy resins are listed in Table 6.7. It can be seen that the stiffer the epoxy resin, the higher the resonance frequency of sway mode. The displacement does not change very much by the increase in the stiffness of epoxy resin, but shows a gentle decreasing trend. For an assumed much stiffer epoxy resin with an elastic modulus of 90 $\times 10^9$ N/m^2, the resonance frequency of sway mode of the planar piezoelectric suspension can be expected to reach 6.54 kHz. As 90 $\times 10^9$ N/m^2 is quite close to the value of E_{11} of the elastic matrix of piezoelectric ceramics, such case can be thought of as a perfect connection between piezoelectric ceramics and load beam. It can thus be seen that improving the bonding condition between the actuator and the suspension enhances the performances of the planar piezoelectric suspension.

Table 6.7: Effects of epoxy resin stiffness on piezoelectric suspensions.

Young's modulus ($\times 10^9$ N/m^2)	Sway mode (kHz)	Displacement Sensitivity (μm/V)
1.50	5.99	0.052
2.50	6.12	0.051
3.50	6.18	0.051
90.0	6.54	0.049

6.7 Optimization of piezoelectric suspension

The objectives of the optimization on the planar piezoelectric suspension are to achieve a highest resonance frequency of sway mode and a satisfactory displacement sensitivity. From the theoretical analyses on the in-plane bending dynamics and the displacement at a driving voltage as described earlier, with the same actuator length and the same width at the actuator fixed end, a triangular split electrode piezoelectric actuator attains a higher resonance frequency of sway mode and higher static displacement sensitivity compared to a rectangular split electrode piezoelectric actuator. However, for the suspension structure with such a built-in piezoelectric actuator, this may not be true due to an additional mass of head gimbal assembly (HGA) attached to the tip of the piezoelectric actuator.

Optimization on the piezoelectric suspension is performed using finite element method. Based upon the theoretical dynamic and electrostatic analyses of the piezoelectric actuator, the optimization was performed by simulating the piezoelectric suspension with different shapes and dimensions of the piezoelectric actuator. The piezoelectric actuator was changed from a rectangular shape to a triangular shape and introduced onto the suspension for the simulation. In the simulations, w_0, the width of one end of the actuator attaching to the load beam of the suspension is kept unchanged while w_1, the width of the other end attaching to the slider and gimbal assembly was changed from 5 mm to 0.2 mm. The resonance frequency of sway mode and the displacement at 12 volts of the piezoelectric suspension with five different w_1 were obtained and listed in Table 6.8.

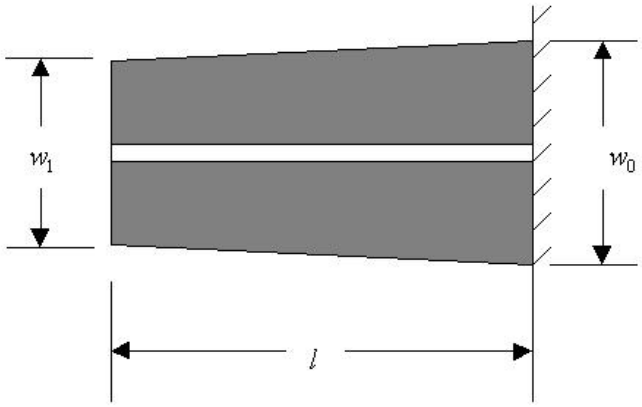

Figure 6.18: Trapezoidal piezoelectric actuator.

Table 6.8: Optimization of piezoelectric suspension.

Value of w_1 (mm)	Sway Mode (kHz)	Displacement at 12 volts (μm)
5 .00	6.12	0.62
4.00	6.50	0.63
2.68	7.06	0.76
1.00	6.23	0.97
0.20	4.64	1.21

The data listed in Table 6.8 is plotted in Figure 6.19. From the simulation results, the displacement sensitivity of the piezoelectric suspension follows the same trend as that of an actuator. That is, increasing w_1 value causes an increase in the displacement of the slider. However, the resonance frequency of sway mode does not change monotonically with w_1. An explanation for this fact is the effects of the total mass of the slider and gimbal assembly (HGA). The total mass of HGA can be looked upon as a point mass at the actuator end. There definitely exists a possible critical value of w_1 of the actuator dimension, such that when w_1 is less than the critical value, the total

stiffness of the suspension decreases as w_1 decreases. This leads to the decrease of the resonance frequency of sway mode. The critical w_1 corresponds to the maximum resonance frequency of sway mode. From Figure 6.19, it can be seen that the critical w_1 value of this structure is about 2.3. This value can be taken as the optimal choice for the reason that it provides the maximum resonance frequency of sway mode and a satisfactory displacement. The corresponding resonance frequency of sway mode and displacement at 12 volts are 7.2 kHz and 0.78 μm respectively. It provides a displacement sensitivity of 0.065 μm/V. The optimized piezoelectric suspension is shown in Figure 6.20. It does not correspond to the largest displacement sensitivity as the smallest w_1 (triangular piezoelectric actuator) does. However, the smallest w_1 sacrifices too much on the resonance frequency of sway mode.

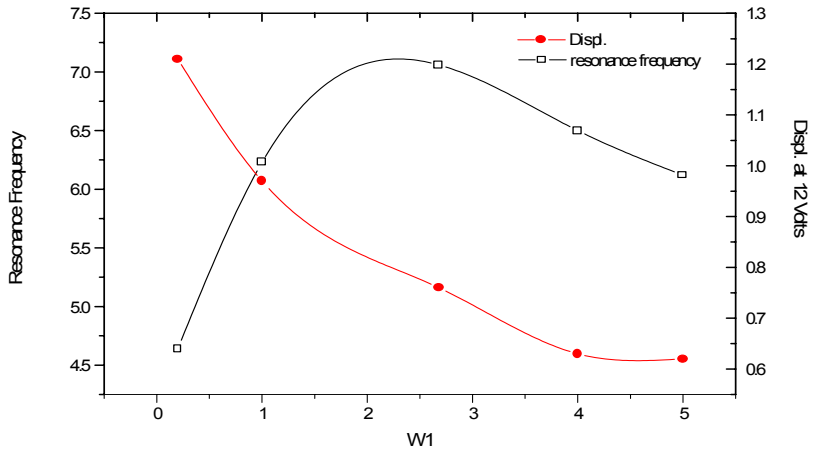

Figure 6.19: Dependence of the sway mode frequency and electrostatic displacement on width w_1.

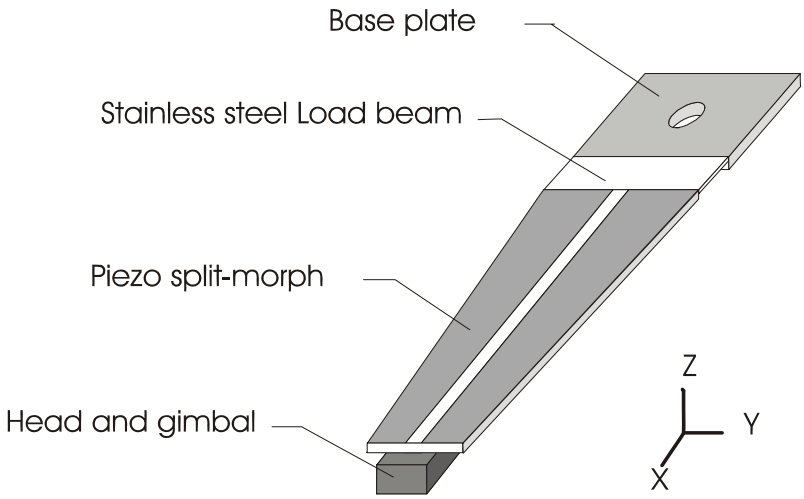

Figure 6.20: Optimized piezoelectric suspension.

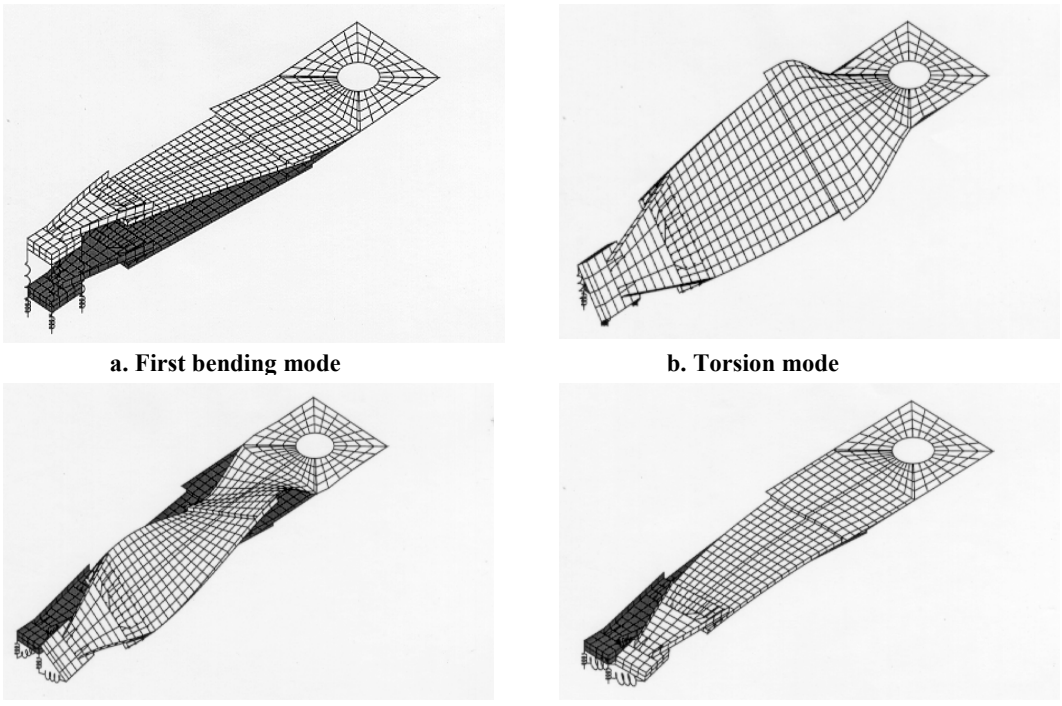

a. First bending mode **b. Torsion mode**

b. Sway mode **b. Static deformation at a driving voltage**

Figure 6.21: Finite element modeling and mode shapes of optimized piezoelectric suspension.

The finite element model and related mode shapes of the optimized piezoelectric suspension are shown in Figure 6.21. The design parameters and simulated performances of Hutchinson 850 suspension, Hutchinson Pico piezoelectric

suspension, planar piezoelectric suspension and optimized piezoelectric suspension are listed in Table 6.9. It is found that the planar piezoelectric suspension shows good characteristics and the optimized piezoelectric suspension demonstrates much improved performances than that of the planar piezoelectric suspension. A prototype of the optimized piezoelectric suspension is shown in Figure 6.22.

Table 6.9: Data list of Hutchinson (850) conventional suspension, Hutchinson-Pico PZT suspension, planar piezoelectric suspension and optimized piezoelectric suspension.

Characteristics	Hutchinson (850)	Hutchinson –Pico PZT Suspension	Planar PZT Suspension	Optimized PZT Suspension
Length from boss to gimbal	18.05	NA	18.05	18.05
Thickness of load beam (mm)	0.076	0.1016	0.076	0.076
Gram load ($\times 10^{-3}$ N)	30~70	NA	40	40
Thickness of PZT	NA	0.1905	0.2	0.2
First bending mode (kHz)	----	----	0.58	0.66
First torsion mode (kHz)	2.4~2.8	----	1.93	2.72
Sway mode (kHz)	>11.0	5.3	6.12	7.20
Sensitivity ($\times 10^{-6}$ m/V)	NA	0.028	0.051	0.065

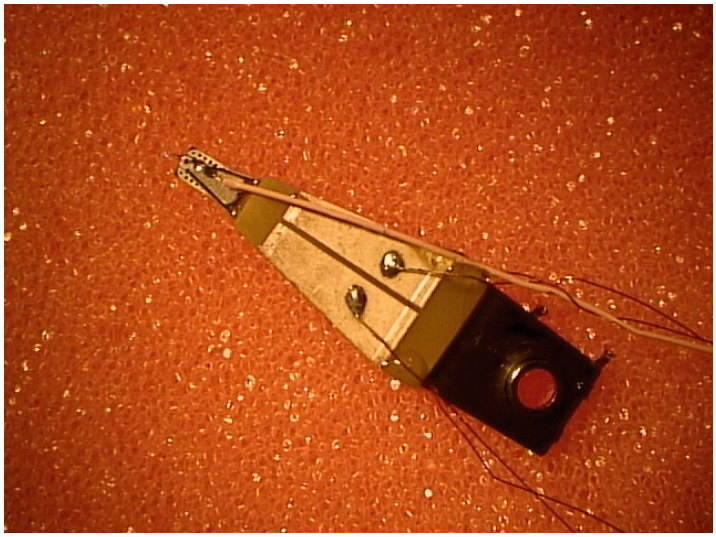

Figure 6.22: The optimized piezoelectric suspension.

6.8 Conclusions

The planar piezoelectric suspension has a sway mode resonance frequency of 6.12 kHz and a displacement sensitivity of 0.051 μm/V. The resonance frequency of sway mode obtained by finite element simulation agrees quite well with experimental result of 6.3 kHz.

The optimized piezoelectric suspension demonstrates a sway mode resonance frequency of 7.2 kHz and a displacement sensitivity of 0.065 μm/V. The performances are superior to that of the planar piezoelectric suspension. Improving the bonding condition between the piezoelectric actuator and the suspension will enhance the performances of the piezoelectric suspension.

The planar and optimized piezoelectric suspension can serve both as a conventional suspension to support slider/head and a secondary micro-actuator to provide accurate and rapid positioning to the recording head.

PART II

RELIABILITY MODELING OF PIEZOELECTRIC MICRO-ACTUATORS

CHAPTER 7

A PROBABILISTIC MODEL TO EVALUATE THE RELIABILITY OF PIEZOELECTRIC MICRO-ACTUATORS

In this chapter, a probabilistic approach is presented to evaluate the reliability of piezoelectric micro actuators. Based on the relationship between the lifetime and degradation mechanism of piezoelectric actuators and the electric field strength, the concept of "electric strength" is proposed to indicate the electric field strength of the piezoelectric actuators at a specified lifetime. The lifetime (number of cycles to failure) of piezoelectric actuator, electric strength, and electric load are considered as the random variables and their probability distributions are discussed. The interference model of electric load and electric strength is applied to reliability design of piezoelectric micro actuators. By this approach, the relationship between the reliability and the lifetime of piezoelectric actuator can be obtained. This reliability model is applied to disk drive head positioning system, and the relationship of the reliability versus lifecycles is given.

7.1 Introduction

The applications of piezoelectric actuators have increased remarkably in many fields that utilize vibrations around the resonance frequency, such as in ultrasonic motors, precision positioners and adaptive mechanical dampers (Uchino, 1998; He, et al., 1999; Morita, 2003). In most cases, the piezoelectric actuator will experience repeated loads during their operation. The fatigue failure and the life cycles issues become important factors to be considered for researchers and engineers. So far there are

several investigations in the fatigue behavior and mechanism of the piezoelectric actuators and the methods of improvement. In general, this research can be categorized into life cycle of the multi-layer ceramic actuator (Thongrueng, et al., 1998; Nakamura, et al., 2001), actuator environmental stability (Yoshikawa and Farrell, 2000), and fracture/crack growth of piezoelectric ceramics (Mall and Hsu, 2000; Mitrovic, et al., 2000; Wang and Carman, 1998; Dausch and Hooker, 1997).

Probabilistic reliability analysis has been widely practiced in the fatigue design and life cycles estimation of mechanical components and structures due to the variation of material properties and environment uncertainties (Mall and Hsu, 2000; Mittrovic, et al., 2000). According to previous research (Nakamura, et al., 2001; Thongrueng, et al., 1998; Yoshikawa and Farrell, 2000), the performances and lifetime of piezoelectric actuators are sensitive to the operating environment and external mechanical and electric loads. Experimental data shows the variation and diversity of the material properties affect the actuator performance. Therefore, it is necessary to introduce probabilistic approaches and statistical tools in the reliability evaluation of piezoelectric actuators.

For the reliability practice in conventional fatigue design and life estimation, *P-S-N* curve, i.e., the relationship among the **P**robability, **S**tress level, and the **N**umber of cycles to failure is used to estimate the fatigue life at a certain reliability level (Carter, 1997). An individual *S-N* curve is obtained by the fatigue test on a certain quantity of specimens in the laboratory. In the life estimation of a practical structure, the local strain and stress of critical parts or locations of the structure are measured. Then the strain or stress is used in conjunction with the *S-N* curve for lifetime estimation. For

miniaturized piezoelectric actuators, numerical methods can be used to obtain the stress and strain of piezoelectric material. However, experimentally it is not convenient to obtain the local strain and stress of the critical locations of piezoelectric micro actuators. Therefore the *S-N* curve is not very useful for the fatigue life estimation. Instead, the relationship between the lifetime (number of cycles to failure) *N* and the strength of electric field *E, E-N* curve is more convenient.

This chapter presents a probabilistic approach to evaluate the long time reliability of piezoelectric micro actuators based on *E-N* curves. The electric load-strength interference model is introduced. The methods to determine the probability distributions of lifetime, electric load, and electric strength are proposed. A case study of disk drive dual stage head positioning piezoelectric micro actuator demonstrates the application of the approach.

7.2 *E-N* curve and *P-E-N* curve

The relationship between the lifetime and the electric field strength of multi-layer piezoelectric is revealed by Thongueng, et al. (1998),

$$\log N = B \log E + C \tag{7.1}$$

where *B* and *C* are constant, and *E* is the applied electric field, and *N* is the life cycles. According to (7.1), the logarithm of lifetime of piezoelectric actuator has a linear relationship with the logarithm of driving voltage *E*. In general, we write the lifetime *N* as the function of driving voltage *E*, i.e.,

$$N = f(E) \tag{7.2}$$

Where N is the lifetime of piezoelectric actuator at a given driving voltage, which is termed as the **electric strength**, and E is the electric strength at a specified lifetime of piezoelectric actuators. The equation (7.2) can be plotted as the E-N curve. Furthermore, considering the variation of material properties and uncertainties of the environment, we take N and E as random variables. Therefore the lifetime (number of cycles to failure) N at a given electric strength will follow a certain probability distribution and similarly the electric strength E will also follow a certain probability distribution at a specified lifetime. The E-N curve with a certain survival probability P is termed as P-E-N curve. The schematic plots of E-N curve and P-E-N curve are shown in Figure 7.1, which are similar to the S-N curve and P-S-N curve in mechanical fatigue. The E-N curve and P-E-N curve can be used for the lifetime estimation of piezoelectric actuators.

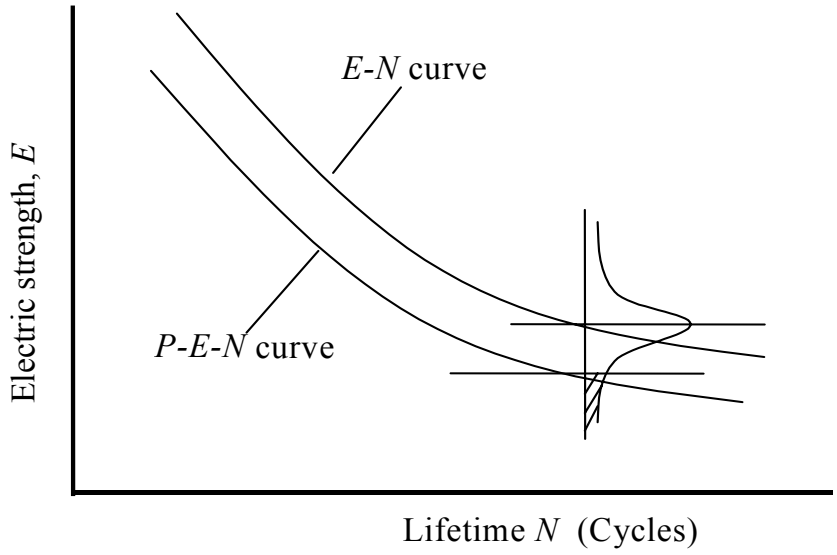

Figure 7.1**:** A schematic plot of E-N and P-E-N curves of piezoelectric actuators.

7.3 Electric load-strength interference model

The well-known stress-strength interference model for mechanical reliability (Carter, 1997) is applied to the reliability evaluation of piezoelectric actuators. Here we call this reliability model as electric load-strength interference model, As shown in Figure 7.2, the reliability of piezoelectric actuators is the **probability** that the electric strength E is greater than electric load e, i.e.,

$$R = P(E > e) \tag{7.3}$$

where R is the reliability quantified by probability. The probability density function of electric load is $w(e)$, the probability density function of electric strength E at a specified lifetime N is $g(E|N)$, as shown in Figure 7.2. The probability of electric load as a specified value e' is $w(e')de$ and the probability of that the electric strength is greater than the specified electric load e' is as

$$P(E > e') = \int_{e'}^{E_{\max}} g(E|N)dE \tag{7.4}$$

where E_{max} is the maximum value of electric strength E. According to the product rule of the probability, when the two events occur simultaneously,

$$dR = w(e)de \int_{e'}^{E_{\max}} g(E|N)dE \tag{7.5}$$

Therefore the probability that the electric strength, E is greater than any electric load, e as the reliability expression (7.3) should be the integration of (7.5) for every possible electric load e, i.e.,

$$R = \int_{e_{\min}}^{e_{\max}} w(e)\left[\int_{e}^{E_{\max}} g(E|N)dE\right]de \tag{7.6}$$

Actually, equation (7.4) becomes a mathematical expression for the *P-E-N* curve. It is necessary to discuss the probability distributions of electric strength and electric load.

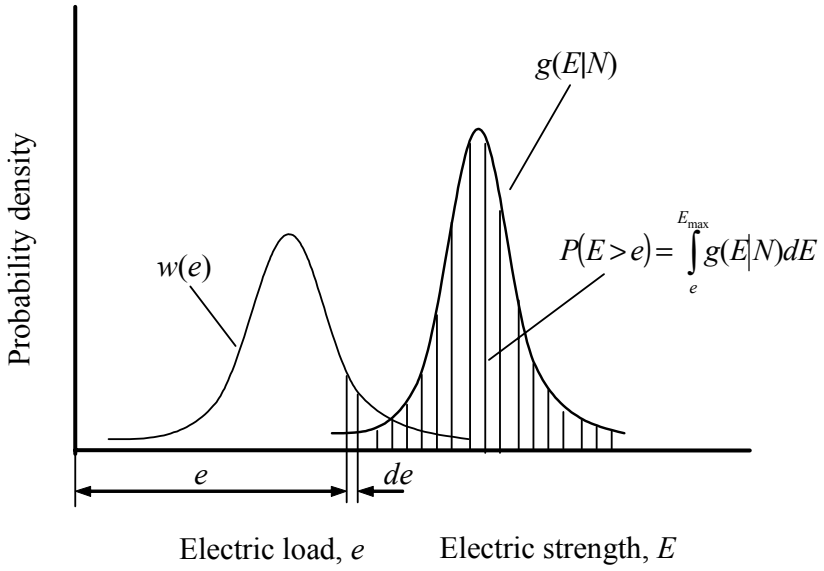

Figure 7.2**:** The electric load-strength interference model.

7.4 Probability distributions of electric strength and electric load

7.4.1 Probability distribution of electric strength

In fatigue reliability, it has been proven that in *P-S-N* curve, the failure probability of fatigue life equals that of fatigue strength (Fu and Gao, 1985). A similar approach can be used to prove that in *P-E-N* curve, there exists equivalence between the failure probability of electric strength at a specified lifetime and that of lifetime at a given electric strength. As shown in Figure 7.3, the corresponding relationship of the failure probability between electric strength and lifetime can be written as

$P(N<N_0|E_0)=P(E<E_0|N_0)$

which can be further expressed as

$$\int_{N_{\min}}^{N_0} f(N|E_0)dN = \int_{E_{\min}}^{E_0} g(E|N_0)dE \tag{7.7}$$

where $f(N|E_0)$ is the probability density function of lifetime at a given electric strength, E_0, whereas $g(E|N_0)$ is the probability density function of electric strength at the

specific lifetime N_0, $N_{\min}$ and $E_{\min}$ are the minimum lifetime and the minimum electric strength respectively. We using an arbitrary point (*N, E*) at the *P-E-N* curve to replace the specific point (N_0, E_0), equation (7.7) becomes

$$\int_{N_{\min}}^{N} f(x|E)dx = \int_{E_{\min}}^{E} g(y|N)dy$$

where, *x* and *y* are dummy integration variables. Therefore, the probability distribution of electric strength can be written as

$$g(E|N) = \frac{d}{dE}\int_{N_{\min}}^{N} f(x|E)dx \tag{7.8}$$

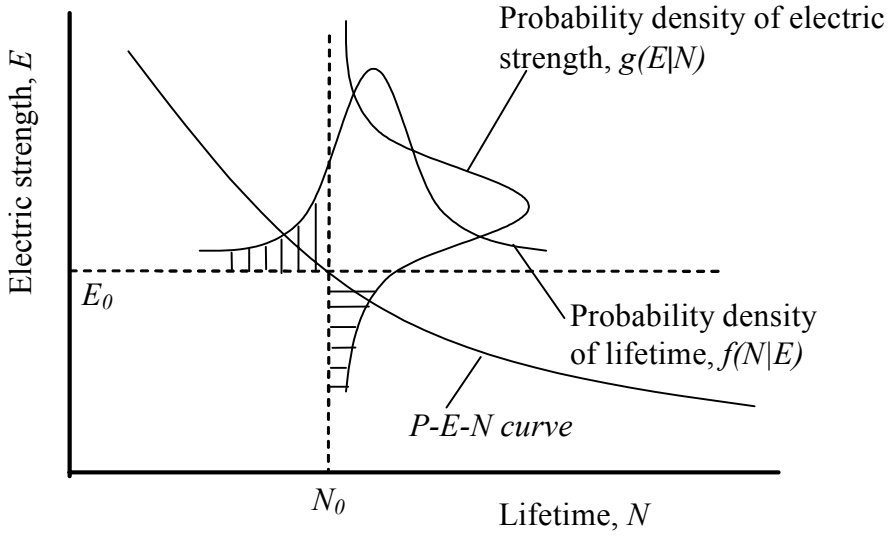

Figure 7.3**:** Equivalence of the failure probability of electric strength and lifetime.

Furthermore, let $\phi(z)$ and $\psi(z)$ be monotonic functions of *z*, according to the principle of probability, there are

$$P(E_{\min} < E < E_0) = P[\psi(E_{\min}) < \psi(E) < \psi(E_0)] \tag{7.9}$$

$$P(N_{\min} < N < N_0) = P[\phi(N_{\min}) < \phi(N) < \phi(N_0)] \tag{7.10}$$

According to (7.7), (7.9) and (7.10), we have,

$$P[\psi(E_{\min}) < \psi(E) < \psi(E_0)] = P[\phi(N_{\min}) < \phi(N) < \phi(N_0)] \tag{7.11}$$

Let $f[\phi(N)|E]$ indicates the probability density function of the function of the lifetime at a given electric strength E, and $g[\psi(E)|N]$ stands for the probability density function of electric strength E at a specific lifetime E, equation (7.11) can be written as

$$\int_{\psi(E_{\min})}^{\psi(E_0)} g[\psi(E)|N_0]d\psi = \int_{\phi(N_{\min})}^{\phi(N_0)} f[\phi(N)|E_0]d\phi \tag{7.12}$$

For an arbitrary point (E, N) in the E-N curve, equation (7.12) can be written as

$$\int_{\psi(E_{\min})}^{\psi(E)} g[y|N]dy = \int_{\phi(N_{\min})}^{\phi(N)} f[x|E]dx \tag{7.13}$$

Therefore, the probability density function of the function of electric strength can be written as

$$g[\psi(E)|N] = \frac{d}{d\psi}\int_{\phi(N_{\min})}^{\phi(N)} f[x|E]dx \tag{7.14}$$

In general, the logarithm of lifetime follows a normal distribution or the lifetime follows a Weibull distribution (Gao, 1986; Fu and Gao, 1985; Gope, 1999). We discuss the two cases.

Case I: Logarithm of lifetime follows a normal distribution

The probability density function of the logarithm of lifetime can be written as

$$f(\log N|E) = \frac{1}{\sqrt{2\pi}\sigma(E)}\exp\left\{-\frac{[\log N - \mu(E)]^2}{2\sigma^2(E)}\right\} \tag{7.15}$$

where, $\mu(E)$ and $\sigma(E)$ are the mean value and standard deviation of the logarithm of lifetime at a given electric strength E. They are functions of electric strength E. By (7.14), (7.15) and let $\phi(N)=\log N$, and $\phi(N_{min})= -\infty$, then,

$$g(\psi|N) = \frac{d}{d\psi}\int_{-\infty}^{\log N}\frac{1}{\sqrt{2\pi}\sigma(E)}\exp\left\{-\frac{[x-\mu(E)]^2}{2\sigma^2(E)}\right\}dx \tag{7.16}$$

Further introducing an integration variable u:

$$u = \frac{\log N - \mu(E)}{\sigma(E)} = \frac{\phi - \mu(e)}{\sigma(E)}, \qquad \phi = \mu + \sigma(E)u$$

$$d\phi = \sigma(E)du$$

(7.16) becomes,

$$g(\psi|N) = \frac{d}{d\psi}\int_{-\infty}^{\frac{\log N-\mu(E)}{\sigma(E)}} \frac{1}{\sqrt{2\pi}} e^{-\frac{u^2}{2}} du \tag{7.17}$$

According to the integration principle,

$$\frac{d}{dx}\int_{-\infty}^{\eta(x)} h(y)dy = h[\eta(x)]\frac{d}{dx}\eta(x)$$

Equation (7.17) becomes

$$g(\psi|N) = \frac{1}{\sqrt{2\pi}}\exp\left\{-\frac{[\log N - \mu(E)]^2}{2\sigma^2(E)}\right\}\frac{d}{d\psi}\left[\frac{\log N - \mu(E)}{\sigma(E)}\right] \tag{7.18}$$

If we let $\psi = E$, then we obtain the probability density function of electric strength as

$$g(E|N) = \frac{\mu(E)\sigma'(E) - \mu'(E)\sigma(E) - \sigma'(E)\log(N)}{\sqrt{2\pi}\sigma^2(E)}\exp\left\{-\frac{[\log(N) - \mu(E)]^2}{2\sigma^2(E)}\right\} \tag{7.19}$$

where, $\mu'(E)$ and $\sigma'(E)$ are the first order derivatives of $\mu(E)$ and $\sigma(E)$ with respect to E.

Case II: Lifetime follows a Weibull distribution

The probability density function of lifetime can be written as

$$f(N|E) = \frac{b(E)}{N_a(E) - N_0(E)}\left[\frac{N - N_0(E)}{N_a(E) - N_0(E)}\right]^{b(E)-1}\exp\left\{-\left[\frac{N - N_0(E)}{N_a(E) - N_0(E)}\right]^{b(E)}\right\} \tag{7.20}$$

where, $N_0(E)$, $N_a(E)$ and $b(E)$ are the minimum lifetime, characteristic lifetime and Weibull shape parameter respectively. By (7.14) and (7.20), and let $\phi(N)=N$, and $\phi(N_{\min})=N_0$, then

$$g(\psi|N)=\frac{d}{d\psi}\int_{N_0(E)}^{N}\frac{b(E)}{N_a(E)-N_0(E)}\left[\frac{N-N_0(E)}{N_a(E)-N_0(E)}\right]^{b(E)-1}\cdot\exp\left\{-\left[\frac{N-N_0(E)}{N_a(E)-N_0(E)}\right]^{b(E)}\right\}dN \tag{7.21}$$

Let,

$$Z=\left[\frac{N-N_0(E)}{N_a(E)-N_0(E)}\right]^{b(E)}$$

Equation (7.21) becomes,

$$g(\psi|N)=\frac{d}{d\psi}\int_0^{\left[\frac{N-N_0(E)}{N_a(E)-N_0(E)}\right]^{b(E)}}e^{-Z}dZ=-\frac{d}{d\psi}\exp\left\{-\left[\frac{N-N_0(E)}{N_a(E)-N_0(E)}\right]^{b(E)}\right\} \tag{7.22}$$

Let $\psi=E$, then the probability density function of electric strength at a specific lifetime is obtained as

$$g(E|N)=\left[\frac{N-N_0(E)}{N_a(E)-N_0(E)}\right]^{b(E)}\left\{-b(E)\left[\frac{N_0'(E)}{N-N_0(E)}+\frac{N_a'(E)-N_0'(E)}{N_a(E)-N_0(E)}\right]+b'(E)\ln\frac{N-N_0(E)}{N_a(E)-N_0(E)}\right\}$$
$$\cdot\exp\left\{-\left[\frac{N-N_0(E)}{N_a(E)-N_0(E)}\right]^{b(E)}\right\} \tag{7.23}$$

where, $N_0'(E)$, $N_a'(E)$ and $b'(E)$ are respectively the first order derivatives of $N_0(E)$, $N_a(E)$ and $b(E)$ to E.

Determination of $\mu(E)$ and $\sigma(E)$

While the logarithm of lifetime follows a normal distribution, $\mu(E)$ and $\sigma(E)$ are respectively the mean and standard deviation of the logarithm of lifetime at a specified E. According to *P-E-N* curve, for normal distribution, the survival probability p is as

$$p=\int_{u_p}^{\infty}\frac{1}{\sqrt{2\pi}}e^{-\frac{u^2}{2}}du \tag{7.24}$$

$$u_p=\frac{\log N_p-\mu(E)}{\sigma(E)} \tag{7.25}$$

where u_p is the standard normal deviate, can be obtained from the standard normal distribution table. N_p is the p^{th} percentile of the lifetime distribution. For two selected survive probabilities p_1, p_2 and corresponding two *P-E-N* curves, there are,

$$u_{p_1} = \frac{\log N_{p_1} - \mu(E)}{\sigma(E)} \tag{7.26}$$

$$u_{p_2} = \frac{\log N_{p_2} - \mu(E)}{\sigma(E)} \tag{7.27}$$

By equations (7.26) and (7.27), $\mu(E)$ and $\sigma(E)$ can be solved. *P-E-N* curve can be obtained by experimental data.

Determination of $N_0(E)$, $N_a(E)$, and $b(E)$

$N_0(E)$, $N_a(E)$, and $b(E)$ can be determined by experimental data. For a series of given electric strength $E_i\,(i=1,\cdots,n)$, we can obtain the corresponding minimum lifetime $N_0(E_i)$, the characteristic lifetime $N_a(E_i)$ and Weibull shape parameter $b(E_i)$. The maximum likelihood method (Montgomery, 2002; Hirose, 1996) and statistic regressions (Li, 1994; Schmid, 1997) can be used to estimate the parameters in a 3-parameter Weibull distribution. By regression analysis, the expressions $N_0(E)$, $N_a(E)$, and $b(E)$ as the functions of *E* can be obtained.

The probability distribution of electric strength can also be obtained according to *E-N* curve and *P-E-N* curve. Based on a series of *E-N* curve and *P-E-N* curve, we can obtain a series E values at a specified lifetime *N*. By statistical analysis of a series E values, its statistical distribution can be estimated. The typical distributions, e.g. normal distribution and Weibull distribution can be used for the distribution

examination. For different specific lifetime $N_i\,(i=1,\cdots,n)$, we can examine the relationship between the statistical distribution of electric load E and the lifetime. In cases that the electric strength E does not follow the typical distributions, the probability distribution should be obtained according to the probability distribution of lifetime.

7.4.2 Probability distribution of electric load

The spectrum of electric load can be determined from the actual applications of the piezoelectric actuators. The probability distribution of the random electric load can be obtained by statistical counting of the random electric load at a certain time period. The reason is that in general case, the load-time process can be taken as stationary stochastic process (Sobczyk and Spencer, 1992). The probability distribution of electric load can be characterized by stochastic process and statistical estimation. The type of probability distribution the electric load fits is determined by the regression analysis results. In general, load follows either a normal distribution or a Weibull distribution. When the load follows the normal distribution, the probability density function of electric load $w(e)$ can be written as

$$w(e)=\frac{1}{\sqrt{2\pi}\sigma_e}\cdot e^{-\frac{(e-\mu_e)^2}{2\sigma_e{}^2}} \tag{7.28}$$

where μ_e and σ_e are the mean value and standard deviation of e respectively. When the load follows the Weibull distribution, then the probability density function of electric load $w(e)$ is written as

$$w(e)=\frac{\alpha}{e_a-e_0}\left(\frac{e-e_0}{e_a-e_0}\right)^{\alpha-1}\exp\left[-\left(\frac{e-e_0}{e_a-e_0}\right)^{\alpha}\right] \tag{7.29}$$

where e_0 , e_a and α are the minimum electric load, characteristic electric load and Weibull shape parameter respectively. In some cases, the minimum value (here referred as e_0) of a three parameter Weibull distribution is set as zero to simplify the calculation without sacrificing the accuracy (Gao, 1986). Then the 3-parameter Weibull distribution becomes a two parameter Weibull distribution.

7.5 Reliability evaluation of a piggyback piezoelectric actuator used for disk drive head positioning system

As described in the last chapter, to suppress the resonance amplitude of the read/write head in a disk drive servo mechanical system and increase the servo bandwidth, a widely accepted solution is to introduce a dual-stage servo control system which uses the voice coil motor in combination a high bandwidth secondary actuator. In the research and development activities of micro actuators, much effort were made on developing piezoelectric micro actuators for their high resolution, fast response and high resonance frequencies. Here, we introduce a piggyback piezoelectric micro actuator developed by Nakamura et al in Hitachi, Ltd. (Nakamura, et al., 2002) to demonstrate the application of the reliability model.

The piggyback piezoelectric micro actuator and its assembly to hard disk drive are shown in Figure 7.4. Nakamura et al. performed fatigue test to this actuator and presented experimental results. From their publication (Nakamura, et al., 2001), we obtain the experimental data of lifetime and driving voltage at 25°C as listed in Table 7.1.

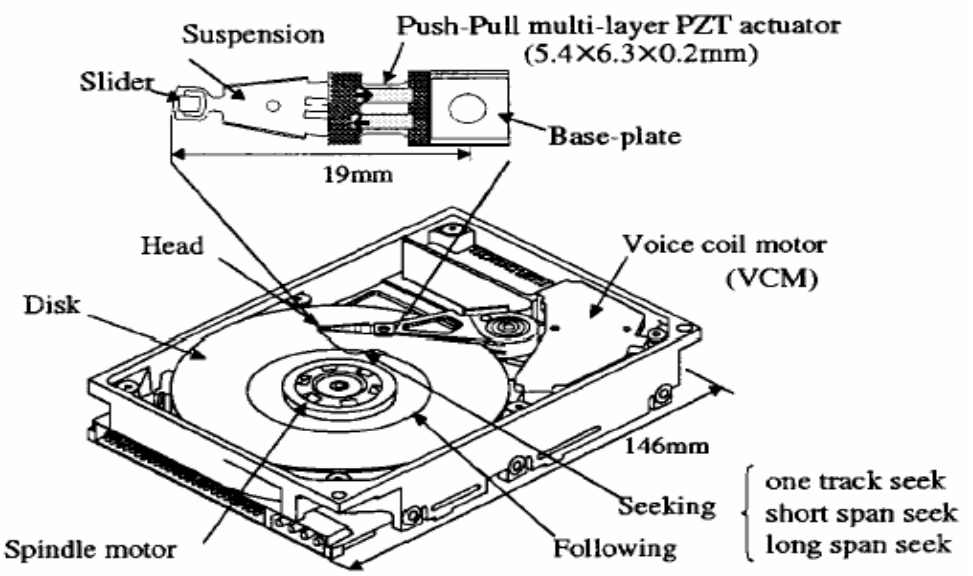

Figure 7.4: A push-pull multi-layer piggy piggyback piezoelectric actuator for dual stage servo in a hard disk drive.

Table 7.1: Lifetime corresponding to different driving voltage of a piggyback micro-actuator for hard disk drive dual stage system (Temperature 25°C).

Driving voltage, E_i (volts)	Lifetime, N_i (cycles)	log E_i	log N_i
6	1.9×10^{10}	0.778	10.279
7	3.5×10^{9}	0.854	9.544
8	5.0×10^{8}	0.903	8.699
9	9.6×10^{8}	0.954	8.982
10	7.3×10^{7}	1.000	7.863
11	1.1×10^{6}	1.041	6.041

7.5.1 Determination of *E-N* curve and *P-E-N* curve

Equation (7.1) can be used to fit the experimental data above. We write equation (7.1) as

$$Y = a + bX \tag{7.30}$$

where $Y = \log N$, $X = \log E$, the estimates of the coefficients a and b are

$$\hat{a} = \frac{1}{n}\sum_{1}^{n} Y_i - \frac{\hat{b}}{n}\sum_{1}^{n} X_i \tag{7.31}$$

$$\hat{b} = \frac{\sum_{1}^{n}\left[X_i - \overline{X}\right]\left[Y_i - \overline{Y}\right]}{\sum_{1}^{n}\left[X_i - \overline{X}\right]^2} \tag{7.32}$$

$$\overline{X} = \frac{1}{n}\sum_{1}^{n} X_i = \frac{1}{n}\sum_{1}^{n} \log E_i \tag{7.33}$$

$$\overline{Y} = \frac{1}{n}\sum_{1}^{n} Y = \sum_{1}^{n} \log N_i \tag{7.34}$$

n is the total number of the group test. By above formula and the data in Table 7., the mean *E-N* curve (corresponding to 50% survival probability) is obtained as

$$\log N = 21.4683 - 13.9967 \log E \tag{7.35}$$

The coefficient of the correlation *r* is calculated as

$$r = \frac{\sum_{i=1}^{n}(X_i - \overline{X})(Y_i - \overline{Y})}{\sqrt{\sum_{i=1}^{n}(X_i - \overline{X})^2 \sum_{i=1}^{n}(Y_i - \overline{Y})^2}} = 0.917$$

At the confidence level γ=100(1-α)%=95%, for n-2=4, the minimum value for *r* is 0.811. Therefore, the fitted equation is satisfactory.

Because there is no further fatigue data available to evaluate the randomness of the lifetime at a specified electric strength, *E*, we present an indirect approach to obtain the *P-E-N* curve. We let the difference of the lifetime between the experimental data and the same point at the fitted curve of equation (7.35), as equation (7.36). The data are listed in Table 7.2.

$$Y' = 21.4683 - 13.9967 \log E_i - \log N_i \tag{7.36}$$

Table 7.2: Lifetime difference between the experimental data and the fitted curve.

$\log E_i$	Log N_i	$21.4683 - 13.9967 \log E_i$	Y'_i
0.778	10.279	10.579	0.300
0.854	9.544	9.515	-0.029
0.903	8.699	8.829	0.130
0.954	8.982	8.115	-0.867
1.000	7.863	7.472	-0.391
1.041	6.041	6.898	0.857

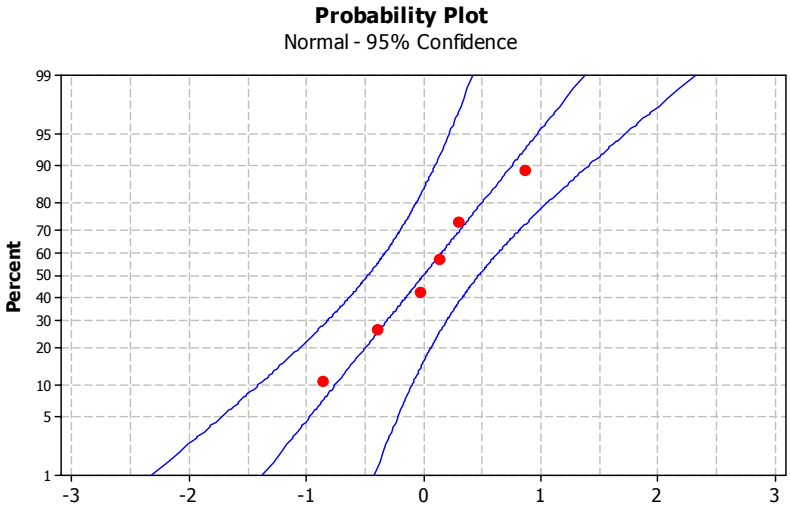

Figure 7.5: Normal probability plot of Y'.

A probability plot of Y' as shown in Figure 7.5 shows that Y' can be considered to be following a normal distribution $N(\mu_{Y'}, \sigma_{Y'}{}^2)$. The estimates of $\mu_{Y'}$, and $\sigma_{Y'}$ are respectively

$$\hat{\mu}_{Y'} = \overline{Y}' = \frac{1}{n}\sum_{1}^{n} Y'_i = 0 \tag{7.37}$$

$$\hat{\sigma}_{Y'} = \sqrt{\frac{\sum_{i=1}^{n}\left(Y'_i - \overline{Y}'\right)^2}{n-1}} = 0.5911 \tag{7.38}$$

Let, $X = (Y - \hat{\mu}_{Y'})/\hat{\sigma}_{Y'}$, then X follows the standard normal distribution $N(0,1)$. Therefore, for a specified survival probability p, we have

$$X_p = \frac{Y_p}{\hat{\sigma}_Y} = u_p \tag{7.39}$$

$$Y_p = u_p \hat{\sigma}_Y \tag{7.40}$$

The *P-E-N* curve equation corresponding to a specified survival probability p, can be written as

$$\log N_p = 21.4683 - 13.9967 \log E + u_p \hat{\sigma}_{Y'} \tag{7.41}$$

For *p*=99.9%, u_p=-3.09, then the *P-E-N* curve equation corresponding 99.9% survival probability can be written as

$$\log N_{99.9} = 19.6418 - 13.9967 \log E \tag{7.42}$$

Figure 7.6 shows the 50% and 99.9% probability *E-N* curves in logarithm coordinates.

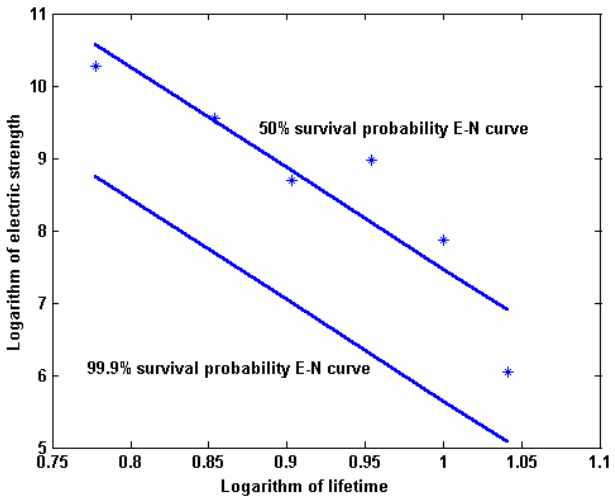

Figure 7.6: *E-N* curves for 50% and 99.9% survival probabilities of piggy back micro actuator for hard disk drive dual stage actuation system.

7.5.2 Determination of probability distribution of electric strength

By the obtained *E-N* curve and *P-E-N* curve, the logarithm of lifetime can be considered following a normal distribution. According to equations (7.26), (7.27), (7.35) and (7.42), we have,

$$u_{50} = \frac{\log N_{50} - \mu(E)}{\sigma(E)} = 0$$

$$u_{99.9} = \frac{\log N_{99.9} - \mu(E)}{\sigma(E)} = -3.09$$

Therefore,

$$\mu(E) = 21.4683 - 13.9967 \log E$$

$$\sigma(E) = 0.5911$$

and

$$\mu'(E) = -6.0657 / E$$

$$\sigma'(E) = 0$$

By equation (7.19), the probability density function of electric strength at a specified lifetime is

$$g(E|N) = \frac{10.2617}{\sqrt{2\pi}E} \exp\left\{ - \frac{\left[\log N - 21.4638 + 13.9667 \log E\right]^2}{2 \times 0.5911^2} \right\} \tag{7.43}$$

For $N = 10^8$, then we have the probability density function of electric strength at 10^8 life cycles as,

$$g(E) = \frac{4.0970}{E} \exp\left\{ - \frac{\left[13.9667 \log E - 13.4638\right]^2}{2 \times 0.5911^2} \right\} \tag{7.44}$$

The plot of the probability density function of electric strength $g(E)$ at 10^8 life cycles is shown in Figure 7.7.

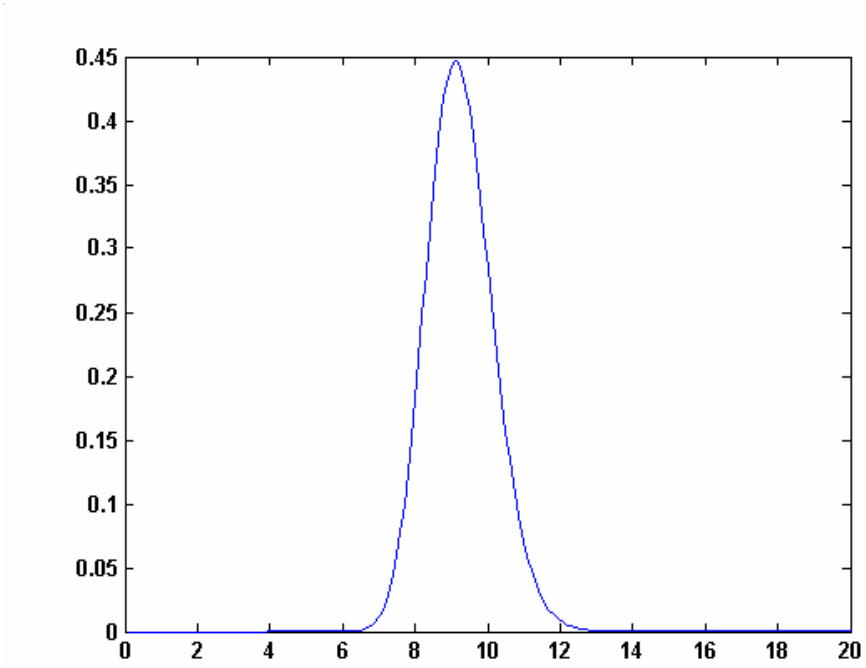

Figure 7.7: Probability distribution of electric strength of a piggy back piezoelectric micro actuator at 10^8 life cycles for hard disk drive dual stage head positioning.

7.5.3 Reliability evaluation of the piggy back piezoelectric micro-actuator in respect to a certain kind of load spectrum

A dual stage control system of hard disk drive is shown in Figure 7.8. The input voltage signals of a piezoelectric micro actuator (Tokuyama, et al., 2001) for the track following are recorded. We evaluate the probability distribution of the electric load according to the measured random electric load spectrum. A two-parameter Weibull distribution can be used to describe the probability distribution of the electric load. The probability density function is as,

$$w(e) = \frac{2.019}{2.67}\left(\frac{e}{2.67}\right)^{1.019} \exp\left[-\left(\frac{e}{2.67}\right)^{2.019}\right] \tag{7.45}$$

It is plotted in Figure 7.9. We post this electric load spectrum to the piggyback piezoelectric micro actuator. By equations (7.6), (7.43), and (7.45), the relationship between the reliability and life cycles of the piezoelectric micro actuator is as (7.46).

For different life cycles, by numerical integration, we can compute the reliability values. They are listed in Table 7.3 and plotted in Figure 7.10. It can be seen that with the progression in life cycles, the reliability drops.

$$R = \int_0^{\infty} \left\{ \frac{2.019}{2.67} \left(\frac{e}{2.67} \right)^{1.019} \exp\left[-\left(\frac{e}{2.67} \right)^{2.019} \right] \right\} \cdot \left[\int_e^{\infty} \frac{10.2617}{\sqrt{2\pi}E} \exp\left\{ -\frac{[\log N - 21.4638 + 13.9667 \log E]^2}{2 \times 0.5911^2} \right\} dE \right] de \tag{7.46}$$

According to design requirement, the piezoelectric micro actuators need to be used for 5 years, which corresponds to 4.7×10^{11} life cycles based on 3 kHz drive. We can calculate the reliability as 96.7%.

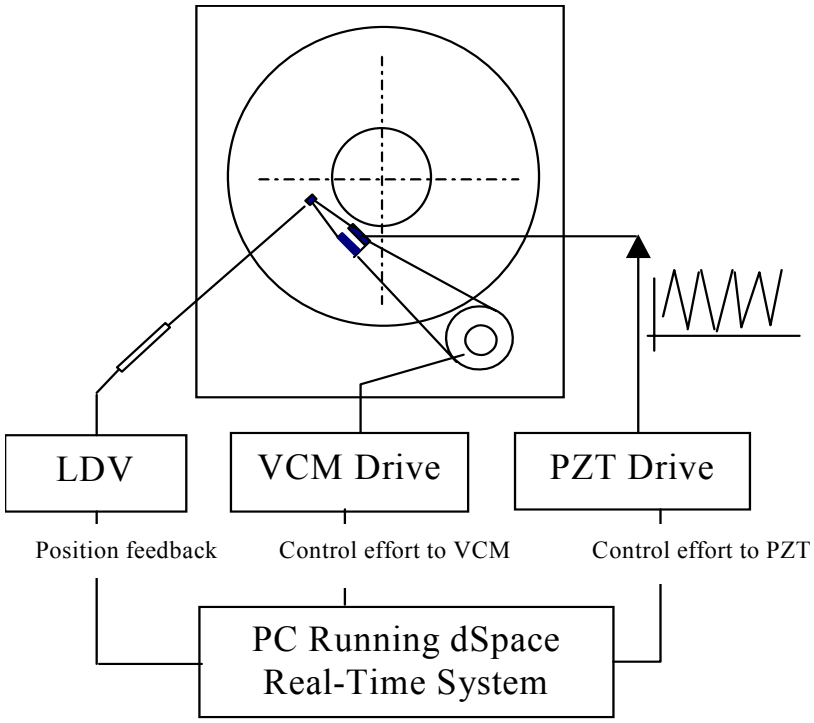

Figure 7.8: Schematic of dual –stage control system.

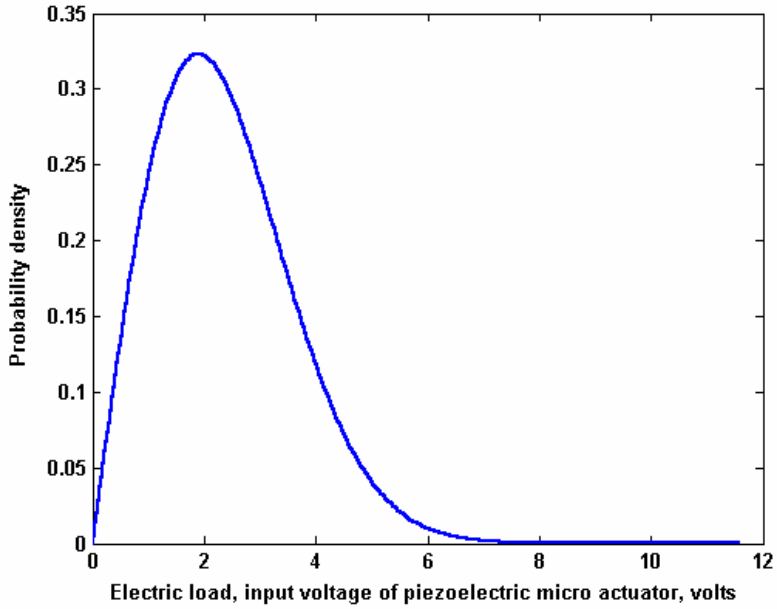

Figure 7.9: Probability density function of electric load, input voltage.

Table 7.3: Calculated results of *R-N*.

N (Number of cycles)	R
10^5	1.0000
10^6	1.0000
10^7	1.0000
10^8	1.0000
10^9	0.9996
10^{10}	0.9967
10^{11}	0.9853
10^{12}	0.9544
10^{13}	0.8945
10^{14}	0.8043
10^{15}	0.6926

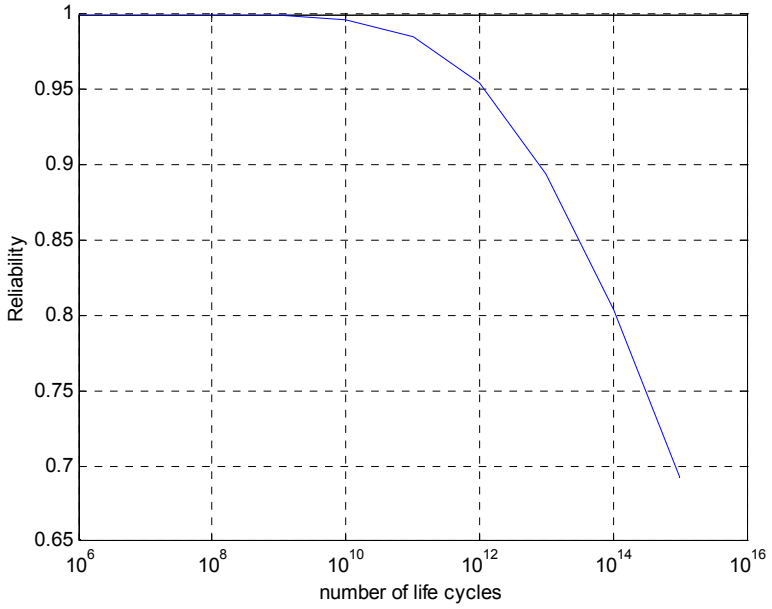

Figure 7.10: Relationship between reliability and life cycles of the piggy back piezoelectric micro actuators.

7.6 Summary

This chapter describes a probabilistic approach to evaluate the reliability of piezoelectric micro actuators, conceptually proposing the electric strength, which is the driving voltage, as a characteristic of piezoelectric micro actuators. According to the relationship between the electric strength and the lifetime (number of cycles to failure), *E-N* curve and *P-E-N* curve are presented. For the reliability analysis, an interference model using probabilistic approach in mechanical reliability is adopted here for the reliability evaluation of piezoelectric micro actuators. With this interference model, the relationship between the reliability (survival probability) and the life cycles can be established.

The approaches to determine the probability distributions of the electric strength and electric load are presented. It is mathematically proven that there exists equivalence

between the failure probability of electric strength at a specified lifetime and that of the lifetime at a given electric strength. Based on this equivalence, the probability of electric strength can be derived according to the probability distribution of lifetime. In the practice of fatigue reliability evaluation, the probability distributions of the lifetime are determined by experiment. Generally the logarithm of lifetime follows a normal distribution or lifetime follows a Weibull distribution. The probability of electric load can be characterized by stochastic process and statistical evaluation of a load spectrum of a certain period of time.

A case of piezoelectric micro actuator in magnetic disk drive dual stage servo system is studied to demonstrate the application of the probabilistic approach. In this case, the experimental data reveals that the logarithm of lifetime of the selected piggyback piezoelectric actuator can be considered following a normal distribution. The probability distribution of electric strength of the piggyback piezoelectric actuator is obtained using the method described with the known probability distribution of the lifetime. The reliability of the piezoelectric actuator is evaluated using the reliability model. Essentially, the reliability drops with the progression of the life cycles.

In this chapter the temperature effects are not considered in this model. In practical operation, temperature significantly affects the lifetime of piezoelectric micro actuator. To take account of the temperature effects, a proposed two-dimensional reliability model is presented in next chapter.

CHAPTER 8

A TWO-DIMENSIONAL PROBABILITY MODEL FOR EVALUATING RELIABILITY OF PIEZOELECTRIC MICRO-ACTUATORS

In this chapter, a probabilistic design approach is presented to evaluate the reliability of piezoelectric micro-actuators with the effects of both driving voltage and temperature. Based on the relationships between the lifetime and degradation mechanism of piezoelectric actuators and the electric field strength, as well as the actuator working temperature, a two-dimensional probability model for evaluating reliability of piezoelectric micro-actuators is described. A concept of two-dimensional strength is proposed to indicate the electric driving voltage and the working temperature of the piezoelectric actuators at a specified lifetime. The lifetime (number of cycles to failure) of piezoelectric actuator, electric load and temperature are considered as random variables and their probability distributions are discussed. A two-dimensional strength probability distribution function is derived according to statistical principles. A two-dimensional interference model between the two-dimensional strength and load is proposed to calculate the reliability of piezoelectric micro-actuators. By this approach, the relationship among the reliability, life cycles, driving voltage and temperature are analytically described. The relationship between reliability and the usage life cycles of piezoelectric actuator can be given. A case study of a piezoelectric micro-actuator used for head positioning in a disk drive demonstrates the application of the approach.

8.1 Introduction

According to previous research (Thongrueng, et al., 1998; Nakamura et al, 2001; Yoshikawa and Farrell, 2000), the performances and lifetime of piezoelectric actuators are sensitive to the operation environment and external mechanical and electric loads. The reliability model, *P-E-N* curve and electric load-strength interference described in Chapter 7, does not take into account temperature effects. Temperature fluctuation is actually only considered as a noise factor in the model.

In practice, temperature plays a significant role in fatigue failure of piezoelectric micro-actuators. In general, increasing temperature decreases the lifetime of piezoelectric micro-actuators. Also temperature changes unpredictably in the daily operation of piezoelectric actuators. In order to address the temperature effects in the reliability model of piezoelectric actuators, we consider both the electric driving voltage and the temperature as random variables. A two-dimensional reliability model is presented for evaluating the reliability of piezoelectric actuators. The *P-N-E-T* surface, which describes the relationship among the reliability, life cycles, electric driving voltage, and temperature, is presented. Based on the fact that the logarithm of lifetime usually follows a normal distribution or lifetime follows a Weibull distribution (Gao, 1986; Ni and Mahadevan, 2004; He, et al., 2005; Shi and Mahadevan, 2003; Xie, et al., 2004; Gope, 1999), a two-dimensional strength probability distribution function is derived. A two-dimensional load-strength interference model is proposed to map the relationship between reliability and the life cycles. We apply the model with temperature effects to the piezoelectric micro-actuator described in Chapter 7 and obtain the relationship curve between the reliability and the life cycles (He et al., 2007).

8.2 *N-E-T* surface and *P-N-E-T* surface

In multi-layer ceramic actuators, it has been observed that the logarithm of the lifetime has a linear relationship with the logarithm of the electric field with a constant temperature (Thongrueng, et al., 1998), which is expressed as

$$\log N = B \log E + C \tag{8.1}$$

where B and C are constants, and E is the applied electric driving voltage, and N is the life cycles. For a constant driving voltage, it is also observed that a linear relationship exists between the logarithm of lifetime and the reciprocal of absolute temperature [8], that is

$$N = A \exp(W /(k \times T)) \tag{8.2}$$

where, W is activation energy (J), k is Boltzmann's constant (=1.38×10^{-23} J/K), T is absolute temperature (K), A is a constant. Based on experiments, Nakamura et al. (2001) derived an equation to formulate the relationship among the lifetime, electric driving voltage, and working temperature of piezoelectric micro-actuator as,

$$\log N = B \log E + Q/(k \times T) + C \tag{8.3}$$

where Q is a constant. The plot of equation (3) can be termed as *N-E-T* surface, which corresponds to a survival probability of 50%. Considering the variation of material properties and uncertainties of the environment, we take *N, E* and *T* as random variables. Therefore the lifetime N at a given electric driving voltage and a given temperature will follow a certain probability distribution and similarly the electric strength and temperature (*E, T*) will also follow a certain probability distribution at a specified lifetime. Therefore, we define (*E, T*) as **two-dimensional strength vector**, which indicates a combination of the actuator driving voltage and working temperature corresponding to a specified lifetime. The *N-E-T* surface with a certain probability P is

termed as *P-N-E-T* surface. A schematic plot of *N-E-T* surface and *P-N-E-T* surface is shown in Figure 8.1. The *N-E-T* surface and *P-N-E-T* surface can be used for the lifetime estimation and reliability evaluation of piezoelectric actuators by taking into account both electric driving voltage and working temperature, the most significant factors affecting the performance and lifetime of piezoelectric actuators.

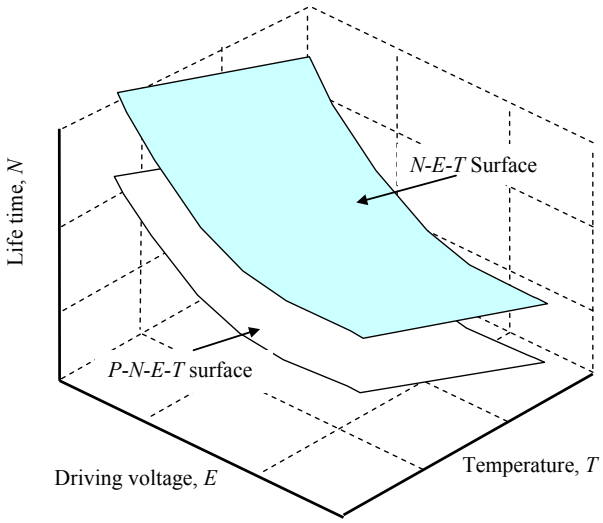

Figure 8.1: A Schematic plot of *N-E-T* surface and *P-N-E-T* surface.

8.3 Two-dimensional probability distribution of strength for piezoelectric micro-actuators

According to the *N-E-T* curve and *P-N-E-T* curve, two-dimensional strength for piezoelectric micro-actuator is expressed as (*E, T*) and for an arbitrary (E_0, T_0) on the *N-E-T* surface, the probability distribution can be expressed as

$$P(E_0,T_0)=P(E_{\min}\le E\le E_0, T_{\min}\le T\le T_0) \tag{8.4}$$

where $E_{\min}$ and $T_{\min}$ are the minimum value of E and T respectively.

According to the equivalence between the failure probability of electric strength at a specified lifetime and that of lifetime at a given electric strength (He, et al., 2005), there is,

$$\int_{N_{\min}}^{N} f(x|E)dx = \int_{E_{\min}}^{E} g(y|N)dy \tag{8.5}$$

By

$$P(N_{\min} \le N \le N_0) = \int_{N_{\min}}^{N_0} f(N|E_0)dN \tag{8.6}$$

We have

$$P(E_{\min} \le E \le E_0) = \int_{N_{\min}}^{N_0} f(N|E_0)dN \tag{8.7}$$

Assume (N_0, E_0, T_0) is a point at $N-E-T$ surface. From the derivation above, the equation above can be written as,

$$P(E_{\min} \le E \le E_0 / T_0) = \int_{N_{\min}}^{N_0} f(N|E_0)dN = \int_{N_{\min}}^{N_0} f(N|(E_0, T_0))dN \tag{8.8}$$

where $f(N|(E_0, T_0))$ is the probability density function of lifetime N at a given two-dimensional strength (E_0, T_0).

Similar derivation approach is applied to the temperature T, we have

$$P(T_{\min} \le T \le T_0 / E_0) = \int_{N_{\min}}^{N_0} f(N|T_0)dN = \int_{N_{\min}}^{N_0} f(N|(E_0, T_0))dN \tag{8.9}$$

Therefore,

$$P(E_{\min} \le E \le E_0|T_0) = P(T_{\min} \le T \le T_0|E_0) \tag{8.10}$$

If the lifetime of every individual (E, T) which belongs to the population ($E_{\min} \le E \le E_0$, $T_{\min} \le T \le T_0$) is N, there will be certainly an individual (E' T_0) ($E' \le E_0$) which

corresponds to the lifetime of N. Therefore every individual (E, T) which belongs to the population ($E_{\min} \le E \le E_0$, $T_{\min} \le T \le T_0$) also belongs to the region ($E_{\min} \le E \le E_0 | T_0$), on the condition $T=T_0$. Therefore the occurrence of the event ($E_{\min} \le E \le E_0$, $T_{\min} \le T \le T_0$) will cause the occurrence of the event ($E_{\min} \le E \le E_0 | T_0$). Hence

$$P(E_{\min} \le E \le E_0, T_{\min} \le T \le T_0) \le P(E_{\min} \le E \le E_0 | T_0) \tag{8.11}$$

In the other aspect, the region ($E_{\min} \le E \le E_0 | T_0$) is a sub-assembly of the region ($E_{\min} \le E \le E_0$, $T_{\min} \le T \le T_0$). Therefore the occurrence of the event ($E_{\min} \le E \le E_0 | T_0$) will cause the occurrence of the event ($E_{\min} \le E \le E_0$, $T_{\min} \le T \le T_0$). Hence,

$$P(E_{\min} \le E \le E_0, T_{\min} \le T \le T_0) \ge P(E_{\min} \le E \le E_0 | T_0) \tag{8.12}$$

Therefore,

$$P(E_{\min} \le E \le E_0, T_{\min} \le T \le T_0) = P(E_{\min} \le E \le E_0 | T_0) = P(T_{\min} \le T \le T_0 | E_0) \tag{8.13}$$

By equations (8.8), (8.9) and (8.13),

$$P(E_0, T_0) = P(E_{\min} \le E \le E_0, T_{\min} \le T \le T_0) = \int_{N_{\min}}^{N_0} f(N | (E_0, T_0)) dN \tag{8.14}$$

When choose any point (N, E, T) at the curved N-E-T surface instead of (N_0, E_0, T_0), we can obtain the probability distribution function of two-dimensional strength (E, T) as

$$P(E, T) = \int_{N_{\min}}^{N} f(z | (E, T)) dz \tag{8.15}$$

where $f(N | (E, T))$ is the probability density function of lifetime N at a given two-dimensional strength (E, T) and z is the integration variable. A lot of research has revealed that the logarithm of lifetime of material failure follows a normal or lifetime

follows a Weibull distribution (Ni and Mahadevan, 2004; He, et al., 2005; Shi and Mahadevan, 2003; Xie, et al., 2004; Gope, 1999). We will elaborate on the two cases.

8.3.1 The case of logarithm of lifetime following a normal distribution

In this case, the logarithm of lifetime follows a normal distribution, i.e., the probability density function of the logarithm of lifetime can be written as

$$f(\log N|E,T)=\frac{1}{\sqrt{2\pi}\sigma(E,T)}\exp\left\{-\frac{[\log N-\mu(E,T)]^2}{2\sigma^2(E,T)}\right\} \tag{8.16}$$

where $\mu(E, T)$ and $\sigma(E, T)$ are the mean and standard deviation of the logarithm of lifetime at a given two-dimensional strength (E, T). They are the functions of the electric driving voltage E and the temperature T and can be obtained by the regression of experimental data.

By equations (8.15) and (8.16), we have

$$P(E,T)=\int_{\log N_{\min}}^{\log N}\frac{1}{\sqrt{2\pi}\sigma(E,T)}\exp\left\{-\frac{[z-\mu(E,T)]^2}{2\sigma^2(E,T)}\right\}dz \tag{8.17}$$

By introducing u, where

$$u=\frac{\log N-\mu(E,T)}{\sigma(E,T)} \tag{8.18}$$

$$d(\log N)=\sigma(E,T)du \tag{8.19}$$

and let $\log N = -\infty$

Then, equation (8.17) becomes,

$$P(E,T)=\int_{-\infty}^{\frac{\log N-\mu(E,T)}{\sigma(E,T)}}\frac{1}{\sqrt{2\pi}}e^{-u^2/2}du \tag{8.20}$$

or

$$u_p = \frac{\log N - \mu(E,T)}{\sigma(E,T)} \tag{8.21}$$

Where u_p is the standard normal deviate, corresponding to the survival probability

$$p = 1 - P(E,T)$$

i.e.,

$$p = \int_{u_p}^{+\infty} \frac{1}{\sqrt{2\pi}} e^{-u^2/2} du \tag{8.22}$$

8.3.2 The case of lifetime following a Weibull distribution

While the lifetime follows a Weibull distribution, i.e., the probability density function can be written as:

$$f(N|E,T) = \frac{b(E,T)}{N_a(E,T) - N_0(E,T)} \left[\frac{N - N_0(E,T)}{N_a - N_0(E,T)} \right]^{b(E,T)-1} \exp\left\{ -\left[\frac{N - N_0(E,T)}{N_a(E,T) - N_0(E,T)} \right] \right\}^{b(E,T)} \tag{8.23}$$

where, $N_0(E, T)$, $N_a(E, T)$ and $b(E, T)$ are the minimal lifetime, characteristic lifetime and Weibull shape parameter respectively. The three parameters in the Weibull distribution can be estimated by maximum likelihood method (Hirose, 1996) etc. They are the functions of the two-dimensional strength (E, T).

According to equations (8.15) and (8.23) and let $N_{min}=N_0(E, T)$, the probability distribution function can be written as:

$$P(E,T) = \int_{N_0(E,T)}^{N} \frac{b(E,E)}{N_a(E,T) - N_0(E,T)} \left[\frac{N - N_0(E,T)}{N_a(E,T) - N_0(E,T)} \right]^{b(E,T)-1} \exp\left\{ -\left[\frac{N - N_0(E,T)}{N_a(E,T) - N_0(E,T)} \right] \right\}^{b(E,T)} dN \tag{8.24}$$

By introducing Z, where

$$Z = \left[\frac{N - N_0(E,T)}{N_a(E,T) - N_0(E,T)} \right]^{b(E,T)} \tag{8.25}$$

Then equation (8.24) becomes

$$P(E,T) = \int_0^{\left[\frac{N - N_0(E,T)}{N_a(E,T) - N_0(E,T)} \right]^{b(E,T)}} e^{-Z} dZ \tag{8.26}$$

Equation (8.26) can be further written as

$$P(E,T) = 1 - \exp\left\{ -\left[\frac{N - N_0(E,T)}{N_a(E,T) - N_0(E,T)} \right]^{b(E,T)} \right\} \tag{8.27}$$

Therefore the survival probability p can be written as

$$p = 1 - P(E,T) = \exp\left\{ -\left[\frac{N - N_0(E,T)}{N_a(E,T) - N_0(E,T)} \right]^{b(E,T)} \right\} \tag{8.28}$$

Equation (8.15) describes the general relationship among the lifecycles N, the two-dimensional strength (E, T) and the failure probability P. When the load level is fixed, equation (8.15) represents for the probability distribution function of lifetime. When the lifetime is fixed, the equation is the probability distribution function of the two-dimensional strength (E, T). While the temperature is fixed, it becomes the *P-N-E* curve. When the driving voltage is a constant, the equation describes the relationship between the lifetime and temperature corresponding to a certain temperature value.

8.4 Determination of $\mu(E, T)$, $\sigma(E, T)$, $N_0(E, T)$, $N_a(E, T)$, and $b(E, T)$

8.4.1 Determination of $\mu(E, T)$ and $\sigma(E, T)$

While the logarithm of lifetime follows a normal distribution, $\mu(E, T)$ and $\sigma(E, T)$ are respectively the mean and the standard deviation of the logarithm of lifetime at a

specified two-dimensional strength (*E, T)*. According to *P-E-T-N* surface, for normal distribution, the survival probability p is as

$$p = \int_{u_p}^{\infty} \frac{1}{\sqrt{2\pi}} e^{-\frac{u^2}{2}} du \tag{8.29}$$

$$u_p = \frac{\log N_p - \mu(E,T)}{\sigma(E,T)} \tag{8.30}$$

where u_p is the standard normal deviate, obtained from the standard normal distribution table. N_p is the corresponding value of logarithm of lifetime. For two selected survive probabilities p_1, p_2 and corresponding two *P-N-E-T* surfaces,

$$u_{p_1} = \frac{\log N_{p_1} - \mu(E,T)}{\sigma(E,T)} \tag{8.31}$$

$$u_{p_2} = \frac{\log N_{p_2} - \mu(E,T)}{\sigma(E,T)} \tag{8.32}$$

By equations (8.31) and (8.32), μ (*E, T*) and σ (*E, T*) can be solved. *P-E-T-N* surfaces can be obtained by experimental data.

8.4.2 Determination of N_0 (*E, T*), N_a (*E, T*), and b (*E, T*)

N_0 (*E, T*), N_a (*E, T*), and b (*E, T*) can be determined by experimental data. For a series of given electric strength E_i(i=1,· · ·, n), T_j (j=1, · · ·, k) we can obtain the corresponding minimum lifetime N_0 (E_i, T_j), the characteristic lifetime N_a (E_i, T_j) and Weibull shape parameter b (E_i, T_j). Then by regression analysis, the expression formula N_0 (*E, T*), N_a (*E, T*), and b (*E, T*) can be obtained.

8.5 Interference model for two-dimensional load (*e, t*) and two-dimensional strength (*E, T*)

Letting the probability density function of two-dimensional load (*e, t*) be *w*(*e*, *t*), according to the probability distribution of two-dimensional strength, in (8.15), the survival probability of piezoelectric micro-actuators can be written as

$$dR = \left(1 - P\left(e, t \middle| N\right)\right) \cdot w(e, t) \cdot de \cdot dt \tag{8.33}$$

By the integration of the above for every possible (*e*, *t*), i.e. Ω, the reliability can be written as

$$R(N) = \iint_{\Omega} dR = \iint_{\Omega} \left(1 - P\left(e, t \middle| N\right)\right) \cdot w(e, t) \cdot de \cdot dt \tag{8.34}$$

i.e.

$$\begin{aligned} R(N) &= 1 - \iint_{\Omega} P\left(e, t \middle| N\right) \cdot w(e, t) \cdot de \cdot dt \\ &= 1 - \iint_{\Omega} w(e, t) \cdot de \cdot dt \cdot \int_{N_{\min}}^{N} f\left(z \middle| (e,t)\right) dz \end{aligned} \tag{8.35}$$

This is the interference model of two-dimensional load and two-dimensional strength, which gives the relationship between the reliability and the usage life cycles.

When the logarithm of lifetime follows normal distribution, by equations (8.20) and (8.35), the relationship between the reliability and the usage life cycles can be written as

$$R(N) = \iint_{\Omega} w(e, t) \cdot de \cdot dt \int_{\frac{\log N - \mu(e,t)}{\sigma(e,t)}}^{\infty} \frac{1}{\sqrt{2\pi}} \exp\left(-\frac{u^2}{2}\right) \cdot du \tag{8.36}$$

When the lifetime follows Weibull distribution, by equations (8.28) and (8.35), the relationship between the reliability and the usage life can be written as

$$R(N) = \iint_{\Omega} w(e,t) \cdot \exp\left\{ -\left[\frac{N - N_0(e,t)}{N_a(e,t) - N_0(e,t)} \right]^{b(e,t)} \right\} de \cdot dt \tag{8.37}$$

8.6 Reliability evaluation of a piezoelectric micro-actuator for disk drive head positioning system with accounting temperature effect

The case study described in this section is the application of a piezoelectric micro-actuator in magnetic recording head positioning system as described in Chapter 7. Figure 8.2 shows a disk drive assembly with a piggyback piezoelectric micro-actuator. From the experimental results (Nakamura, et al., 2001), the lifetime of the piezoelectric micro-actuator at different driving voltage and temperature are listed in Table 8.1.

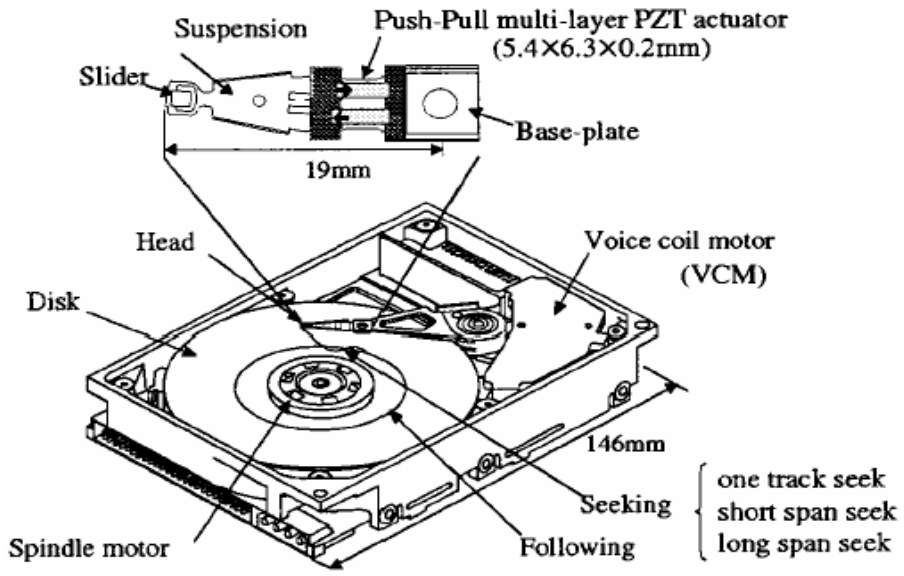

Figure 8.2: A push-pull multi-layer piggy piggyback piezoelectric actuator for dual stage servo in a hard disk drive.

Table 8.1: Lifetime of the piggyback piezoelectric micro-actuators hard disk drive dual- stage system.

Observations	Temperature (K)	Driving voltage, E_i, (volts)	Lifetime, N_i (cycles)	log E_i	log N_i
1	298	6	1.9×10^{10}	0.778	10.279
2	298	7	3.5×10^{9}	0.845	9.544
3	298	9	9.6×10^{8}	0.954	8.982
4	298	10	7.3×10^{7}	1.000	7.863
5	298	11	1.1×10^{6}	1.041	6.041
6	348	5	1.1×10^{9}	0.699	9.041
7	348	6	0.9×10^{9}	0.778	8.954
8	348	7	0.6×10^{6}	0.845	5.778
9	373	5	1.1×10^{7}	0.699	7.041
10	373	6	5.5×10^{5}	0.778	5.740
11	373	7	1.0×10^{5}	0.845	5.000

8.6.1 Determination of *N-E-T* surface and *P-N-E-T* surface

Based on the proposed equation (8.3) to describe the relationship among the lifetime, driving voltage and temperature, the least square method is used for the multiple linear regression. Equation (8.3) can be written in the general form,

$$Y = \beta_0 + \beta_1 x_1 + \beta_2 x_2 \tag{8.38}$$

where Y=log N, x_1=log E and x_2=1/(kT). As described early, k is Boltzmann's constant (=1.38×10^{-23} J/K). The estimates of β_0, β_1 and β_2 can be determined from following equations (Montgomery, 2003):

$$\left.\begin{aligned} n\hat{\beta}_0 + \hat{\beta}_1 \sum_{i=1}^{n} x_{1i} + \hat{\beta}_2 \sum_{i=1}^{n} x_{2i} &= \sum_{i}^{n} y_i \\ \hat{\beta}_0 \sum_{i}^{n} x_{1i} + \hat{\beta}_1 \sum_{i=1}^{n} x_{1i}^{\,2} + \hat{\beta}_2 \sum_{i=1}^{n} x_{1i}x_{2i} &= \sum_{i=1}^{n} x_{1i}y_i \\ \hat{\beta}_0 \sum_{i}^{n} x_{2i} + \hat{\beta}_1 \sum_{i=1}^{n} x_{1i}x_{2i} + \hat{\beta}_2 \sum_{i=1}^{n} x_{2i}^{\,2} &= \sum_{i=1}^{n} x_{2i}y_i \end{aligned}\right\} \tag{8.39}$$

Where n is the number of total observations. According to the data listed in Table 8.1, the estimates of β_0, β_1 and β_2 can be obtained as:

$$\hat{\beta}_0 = -0.582 \qquad \hat{\beta}_1 = -15.776 \qquad \hat{\beta}_2 = 9.7704\times10^{-20} \tag{8.40}$$

Therefore the regression equation describe the relation among the lifetime, electric driving voltage and temperature is written as

$$\log N = -0.582 - 15.776 \log E + \frac{9.7704 \times 10^{-20}}{kT} \tag{8.41}$$

The coefficient of determination of the regression is calculated as

$$R^2 = 1 - \frac{SS_E}{SS_T} = 0.853 \qquad \text{and} \qquad R = 0.9236 \tag{8.42}$$

where,

$$\left.\begin{aligned} SS_E &= \sum_{i=1}^{n} (y_i - \hat{y}_i)^2 \\ SS_T &= \sum_{i=1}^{n} (y_i - \bar{y}_i)^2 \end{aligned}\right\} \tag{8.43}$$

At the confidence level γ=95%, for n-2=9, the minimum value of R is 0.602. Therefore, the fitted equation is satisfactory.

To get the *P-E-T-N* relationship, we use the similar indirect approach as described in Chapter 7. We list the difference of the lifetime between the experimental data and the same point at the fitted curve in Table 8.2. y'_i is calculated as

$$y_i' = -0.582 - 15.776 \log E_i + \frac{9.7704 \times 10^{-20}}{kT} - \log N_i \tag{8.44}$$

Table 8.2: Lifetime difference between the experiment and the estimation.

Temperature (K)	log E_i	log N_i	-0.582-15.776log E_i+9.7704×10^{-20}/(kT)	y_i'
298	0.778	10.279	10.9027	0.6237
298	0.845	9.544	9.8457	0.3017
298	0.954	8.982	8.1261	-0.8559
298	1.000	7.863	7.4004	-0.4626
298	1.041	6.041	6.7536	0.7126
348	0.699	9.041	8.7425	-0.2985
348	0.778	8.954	7.4962	-1.4578
348	0.845	5.778	6.4392	0.6612
373	0.699	7.041	7.3718	0.3308
373	0.778	5.740	6.1255	0.3855
373	0.845	5.000	5.0685	0.0685

A probability plot of y' is shown in Figure 8.3. We can see that y' can be considered following a normal distribution $N(\mu_{y'}, \sigma_{y'})$. The estimates of $\mu_{y'}, \sigma_{y'}$ are

$$\hat{\mu}_{y'} = \frac{1}{n}\sum_{1}^{n} y_i' = 0 \tag{8.45}$$

$$\hat{\sigma}_{y'} = \sqrt{\frac{\sum_{i=1}^{n}\left(y_i' - \bar{y}'\right)^2}{n-1}} = 0.6963 \tag{8.46}$$

Let, $x = (y_i' - \hat{\mu}_{y'})/\hat{\sigma}_{y'}$, then x follows the standard normal distribution $N(0,1)$. Therefore, for a specified survival probability p, we have

$$x_p = \frac{y'_p - \hat{\mu}_{y'}}{\hat{\sigma}_{y'}} = u_p \tag{8.47}$$

$$y_p = u_p \hat{\sigma}_{y'} \tag{8.48}$$

The *P-E-T-N* curve equation corresponding to a specified survival probability p, can be written as

$$\log N_p = -0.582 - 15.776 \log E + \frac{9.7704 \times 10^{-20}}{kT} + u_p \hat{\sigma}_{y'} \tag{8.49}$$

For the survival probability p=99.9%, the normal standard deviate u_p=-3.09, then the *P-E-T-N* curve equation corresponding to 99.9% survival probability can be written as

$$\log N_{99.9} = -2.7336 - 15.776 \log E + \frac{9.7704 \times 10^{-20}}{kT} \tag{8.50}$$

Figure 8.4 shows the 50% and 99.9% probability *E-T-N* surface. Figure 8.5 shows that *P-E-T* curve at a specified lifetime N=10^{10} cycles. The *E-T-N* curve can be used to determine the driving voltage and working temperature according to specified reliability and lifetime requirements.

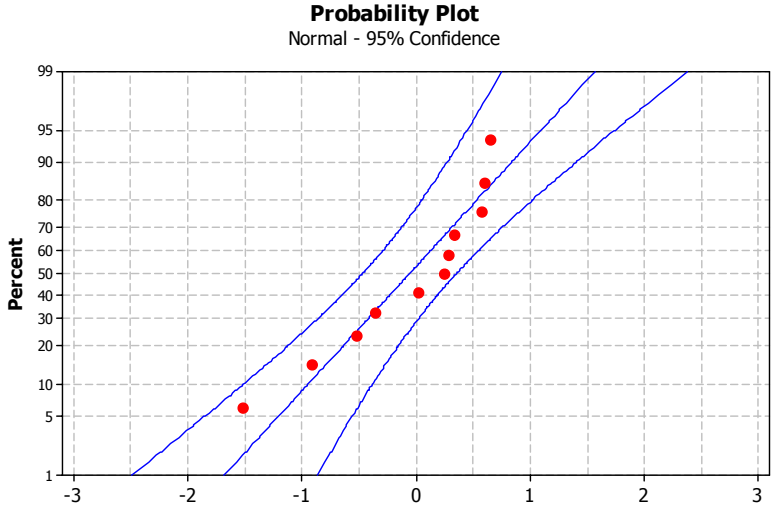

Figure 8.3: Normal probability plot of y'_i, the difference between the experimental data and the estimated values.

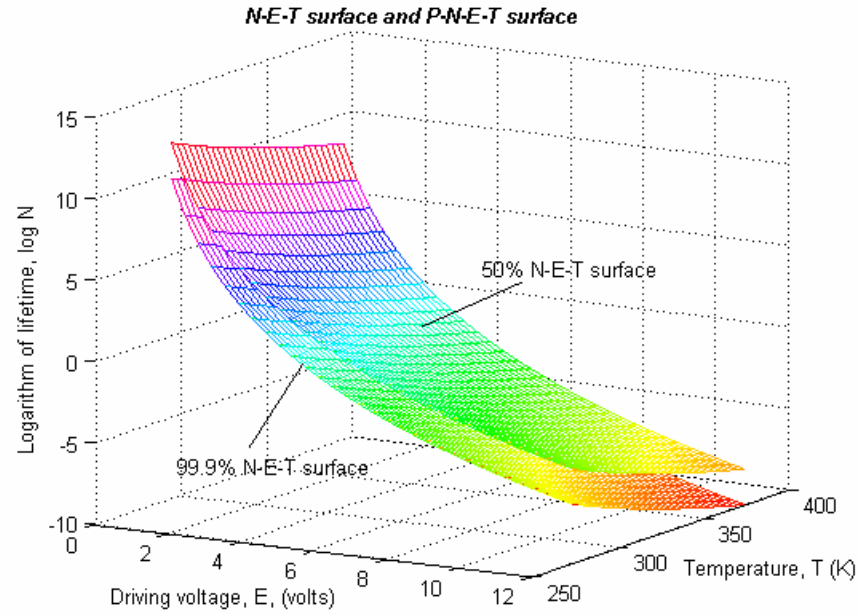

Figure 8.4: *N-E-T* surface and *P-N-E-T* surface of the piggy back piezoelectric actuators.

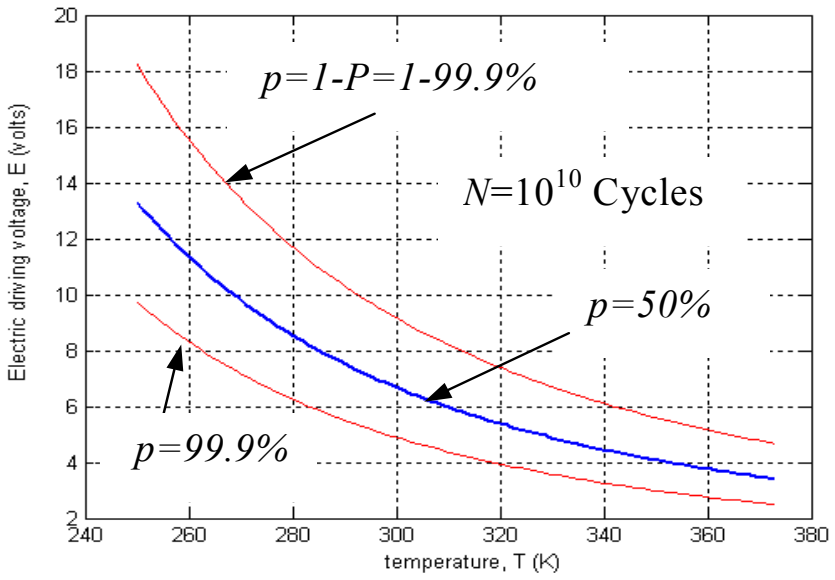

Figure 8.5: *P-E-T* curve at lifetime $N=10^{10}$ cycles.

8.6.2 Determination of probability distribution function of two-dimensional strength

According to the *E-T-N* and *P-E-T-N* surface equations, the logarithm of lifetime can be considered following a normal distribution. According to equations (8.31) and (8.32),

$$u_{50} = 0$$
$$u_{99.9} = -3.09$$

We have,

$$\left.\begin{aligned}\mu(E,T) &= -0.582 - 15.776\log E + \frac{9.7704\times10^{-20}}{kT}\\ \sigma(E,T) &= 0.6963\end{aligned}\right\} \tag{8.51}$$

Therefore, the probability density function of the logarithm lifetime, log N can be written as

$$f\left(\log N \middle| E, T\right) = \frac{1}{\sqrt{2\pi}\times 0.6963} \cdot \exp\left\{-\frac{\left[\log N + 0.582 + 15.776\log E - 9.7704\times10^{-20}/(kT)\right]^2}{2\times 0.6963^{\,2}}\right\} \tag{8.52}$$

The probability distribution function of the two-dimensional strength (E, T) can be written as

$$P(E,T) = \int_{\log N_{\min}}^{\log N} \frac{1}{\sqrt{2\pi}\times 0.6963} \cdot \exp\left\{-\frac{\left[z + 0.582 + 15.776\log E - 9.7704\times10^{-20}/(kT)\right]^2}{2\times 0.6963^{\,2}}\right\} dz \tag{8.53}$$

8.6.3 Reliability evaluation

As reported in Chapter 7, the input voltage of a piggy-back piezoelectric micro-actuator for the dual stage control of hard disk drive actuator follows a Weibull distribution. The probability density function is as

$$w_e(e) = \frac{2.019}{2.67}\left(\frac{e}{2.67}\right)^{1.019} \cdot \exp\left[-\left(\frac{e}{2.67}\right)^{2.019}\right] \tag{8.54}$$

In general practice, the design temperature for a hard disk drive is from 5~55°C (278~328 *K*) (IBM storage products), therefore, we assume the temperature follows a normal distribution with the mean μ=303 *K* and six sigama 6σ=328-278 = 50 *K*. The probability density function of temperature in a hard disk drive is written as

$$w_t(t) = \frac{1}{\sqrt{2\pi}\times 8.33} \cdot \exp\left[-\frac{(t-303)^2}{2\times 8.33^2}\right] \tag{8.55}$$

Further, the driving voltage *e*, and temperature *t* are considered as independent random variables, the joint probability density function of (*e*, *t*) can be written as

$$w(e,t) = \frac{2.019}{2.67}\left(\frac{e}{2.67}\right)^{1.019} \exp\left[-\left(\frac{e}{2.67}\right)^{2.019}\right] \cdot \frac{1}{\sqrt{2\pi}\times 8.33} \cdot \exp\left[-\frac{(t-303)^2}{2\times 8.33^2}\right] \tag{8.56}$$

By equations (8.35), (8.53), and (8.56), the relationship between the reliability and the lifetime is expressed as:

$$R(N) = 1 - \iint_{\Omega} \frac{2.019}{2.67}\left(\frac{e}{2.67}\right)^{1.019} \exp\left[-\left(\frac{e}{2.67}\right)^{2.019}\right] \cdot \frac{1}{\sqrt{2\pi}\times 8.33} \cdot \exp\left[-\frac{(t-303)^2}{2\times 8.33^2}\right] de \cdot dt$$
$$\cdot \int_{\log N_{\min}}^{\log N} \frac{1}{\sqrt{2\pi}\times 0.6963} \cdot \exp\left\{-\frac{\left[z + 0.582 + 15.776\log e - 9.7704\times 10^{-20}/(kt)\right]^2}{2\times 0.6963^2}\right\} dz \tag{8.57}$$

The integration range is selected as $0 < e < \infty$, $0 < t < \infty$, $\log(N_{\min}) = -\infty$. The calculated reliabilities at different number of life cycles are listed in Table 8.3 and plotted in

Figure 8.6. It is similar to the result obtained in Chapter 7 that with the progression of life cycles, the reliability drops. Generally the piezoelectric actuators are designed for 5 years use according to hard disk drive design requirement. It corresponds to 4.7×10^{11} cycles at 3 kHz driving. The calculated reliability is 96.32%.

Commercial hard disk drives are speculated to have an annual failure rate 0.3 to 3%, with nominal being close to 1% (Hughes et al., 2002). This reflects on a reliability of 95% of the commercial hard disk drives for 5 years operation. Therefore, the described piezoelectric micro-actuators, with the projected reliability 96.32% for 5 years at 3 kHz driving, can be considered to have a satisfactory reliability when compared with the commercial hard disk drives.

Table 8.3: Calculated results of life cycles and reliability.

N (number of cycles)	Reliability, $R(N)$
10^5	1.0000
10^6	1.0000
10^7	1.0000
10^8	0.9998
10^9	0.9987
10^{10}	0.9944
10^{11}	0.9819
10^{12}	0.9541
10^{13}	0.9049
10^{14}	0.8330
10^{15}	0.7422

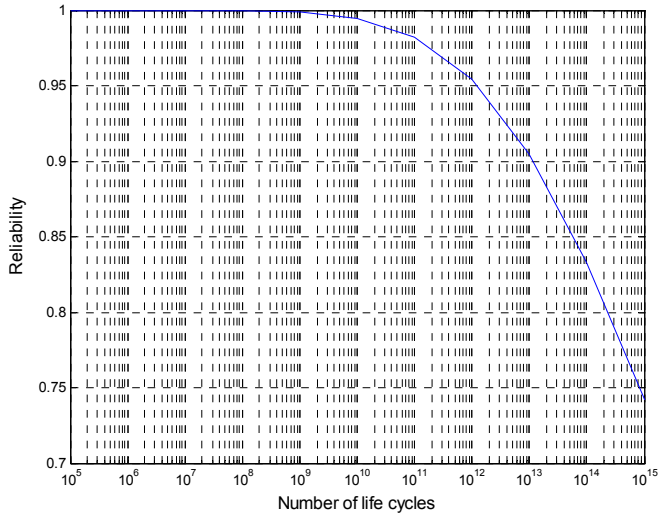

Figure 8.6: Relationship between reliability and the number of life cycles of the piggy back piezoelectric micro-actuators.

8.7 Summary

This chapter describes a probability approach to evaluate the reliability of piezoelectric micro-actuators with consideration of temperature effects. A concept of two-dimensional strength (electric driving voltage and temperature) is proposed. According to the relationship among the electric driving voltage, the working temperature, and the lifetime (number of cycles to failure), *N-E-T* surface and *P-N-E-T* surface are presented. The probability distribution function of the two-dimensional strength is derived. For the reliability analysis, a two-dimensional interference model using probabilistic approach is proposed here for the reliability evaluation of piezoelectric micro-actuators. With this interference model, the relationship between the reliability (survival probability) and the life cycles can be established.

This chapter also presents the approaches to determine the probability distribution of the two-dimensional strength. It is mathematically proven that there exists equivalence

between the failure probability of electric driving voltage, temperature at a specified lifetime and that of the lifetime at a given electric driving voltage or temperature. Based on this equivalence, the probability distribution of two-dimensional strength can be derived according to the probability distribution of lifetime. In the practice of fatigue reliability evaluation, the probability distribution of the lifetime is determined by experiment. Generally the logarithm of lifetime follows a normal distribution or lifetime follows a Weibull distribution. The probability of two-dimensional load is characterized by stochastic process and statistical evaluation of a load spectrum of a certain period of time.

A case of piezoelectric micro-actuator in magnetic disk drive dual stage servo system is studied to demonstrate the application of the probabilistic approach. In this case, the logarithm of lifetime of the selected piggyback piezoelectric actuator is considered following a normal distribution. The probability distribution of the two-dimensional strength of the piggyback piezoelectric actuator is obtained using the method described with the known probability distribution of the lifetime.

CHAPTER 9

SUMMARY AND RECONMMENDATIONS

The present study addresses the dynamics and reliability problems in the access systems of high density magnetic recording. A survey on the previous researches and improvements in disk drive servo mechanical systems has been conducted. Based on previous efforts in studying the disk drive servo mechanical systems, further improvements in the dynamic performances of the disk drive access systems through several novel structure designs are motivated. The structural dynamic performances of these structures are evaluated via modeling, optimization and experimental investigations.

A probability approach used to evaluate the reliability of piezoelectric actuators or general mechatronics devices has been proposed. This reliability model is further expanded to the two-dimensional case to take into account the effects of both the electric field and temperature. These reliability models are employed for the reliability evaluation and lifetime estimation of the hard disk drive dual-stage head positioning systems with piezoelectric micro-actuators. The relationship between the life cycles and the reliability are obtained.

9.1 Concluding Remarks

(1) The dynamics of a disk drive access system can be viewed as a spring-damping-mass system coupled with structural deformation. The structural dynamics can be characterized using structural finite element modeling and experimental dynamic

measurement approaches. Finite element modeling is generally employed to analyze the modal shapes of the designed structure and to simulate the frequency responses of the head actuator assembly along the tracking direction while experimental dynamic analysis is employed to measure the frequency response of head actuator assembly and characterize the pivot bearing stiffness.

(2) The proposed disk drive actuator assembly with forced coupled actuation significantly suppresses the actuator lateral translational motion mode. With the structural design innovation, the reaction force on the pivot bearing due to the voice coil motor (VCM) excitation is minimized. As the lateral translational vibration mode is not excited, the first dominant resonant mode to affect the achievable track density is the structural arm in-plane bending mode. It is 11. 5 kHz, 2 to 3 times higher than the lateral translational mode at 3~5 kHz. Therefore the servo control bandwidth can be significantly increased due to the enhancement of the structural improvement. Finite element analysis results agree well with experimental results measured on a prototype of the design.

(3) The flexural pivot proposed here for use in disk drive actuator aims to achieve a friction free actuation for disk drive servo mechanical system. By finite element modeling and experimental measurement of actuator assembly with the flexural pivot, the flexural pivot was shown to have a comparable translational stiffness and lower tilt stiffness compared with the conventional bearings. By lifetime test, thermal analysis, and control implementation, the proposed flexural pivot demonstrates good fatigue performance and low thermal stresses, as well as a satisfactory control performance.

(4) An actuator assembly with small skew actuation is presented in the fulfillment of reduction of skew angle in the conventional head actuator assembly. The head skew angle variation can be minimized by optimize the length ratio (the ratio of the distance between the pivot center and the head to that between pivot center and the disk center). The absolute skew angle reduction can be achieved by slanting the suspension an angle to the actuator arm. With the existing structure combination for a 3.5" disk drive, the optimized length ratio is 1.11 and the minimal skew angle can be achieved is ± 2°. Because the arm length ration is increased compare to that the existing arm length ratio, 0.93, the arm resonant frequency drops 20~30%. However, from both finite element modeling and experimental measurement, there is no significant change in the dynamic performance for the actuator with a slant suspension.

(5) Dynamics analysis and structural optimization are conducted on a split-electrodes piezoelectric micro-actuator and the piezoelctrically actuated head suspension structure. Finite element modeling is employed to simulate the piezoelectric behavior in terms of both static and dynamic performance. From analytical, numerical and experimental investigations, a triangular actuator demonstrates the best dynamic performances in term of the resonant frequency and a static stroke compared to the rectangular and the trapezoidal split-electrodes piezoelectric actuators. However, for the piezoelectrically actuated suspension structure, a trapezoidal actuator demonstrates the best dynamic performance while a triangular actuator demonstrates the largest static deflection. An optimized structure is proposed in terms of dynamic performance.

(6) A probability approach is proposed for the reliability evaluation of piezoelectric actuators. *P-E-N* curve can describe the relationship among the probability, electric strength and lifetime of piezoelectric actuators. The electric driving voltage and life cycles can be taken as the random variables. Generally the logarithm of lifetime follows a normal distribution or lifetime follows a Weibull distribution. The probability distribution of the electric strength is derived from the probability of lifetime according to the equivalence between the probability distribution of lifetime and that of the electric strength. The load-strength interference model is established according to the probability distributions of both electric load and electric strength. The reliability-life cycles relationship is given according to the interference model. This approach is employed to evaluate the reliability of piezoelectric actuators in a disk drive head positioning system.

(7) The probability model for the piezoelectric actuators is further expanded to two-dimensional case to take into account both the electric field and temperature effects. In this case, the concept of a two-dimensional strength vector, which respectively represents the electric strength and temperature strength, is introduced. The relationship among the probability, electric strength, temperature strength, and lifetime, i.e., *P-E-T-N* surface can be conveniently used for the reliability evaluation and lifetime estimation. The two-dimensional probability function is determined according to the *P-E-T-N* surface. The two-dimensional load-strength interference model is established according to the probability distributions of both two-dimensional load and strength. This gives the relationship between the reliability and the life cycles. The application of this model in the disk drive head position system using a piezoelectric micro-actuator

shows that it can conveniently be used for reliability analysis, gives a reasonable result.

9.2 Original contributions of the research

The present project aims to study and improve the dynamics of disk drive access systems via several novel structural designs and address the reliability of piezoelectric micro-actuators in magnetic recording dual-stage servo mechanical system. The contributions of this research can be summarized as:

(1) Fulfilled the mechanical design, structural simulation and experimental investigation of a proposed actuator structure to suppress the disk drive actuator lateral translational resonant mode to enhance the disk drive actuator servo bandwidth.

(2) Proposed a flexural pivot for use in disk drive actuator, revealed the dynamic performance of the disk drive actuator assembly with the flexural pivot.

(3) Proposed and optimized the actuator assembly with a small skew actuation. With this actuator assembly, the skew angle change can be reduced to ±2º from the existing 30º for a head actuator assembly. Revealed and compared the dynamic performance of the actuator design with the existing head actuator assembly.

(4) Completed the structural simulation and optimization of the split-electrodes piezoelectric actuator and the piezoelectric suspension structure. Presented an optimized structure of the piezoelectric suspension.

(5) Proposed a probability approach for the reliability evaluation and lifetime estimation of piezoelectric micro actuators. The reliability model can be used to evaluate the reliability of general mechatronics devices. Piezoelectric actuators in disk drive micro positioning systems show the typical application of the model.

(6) Expanded the reliability model above to a two-dimensional case to address the effects from both the electric driving voltage and temperature. Therefore, the expanded model describes the relationship between the reliability and life cycles more accurately.

9.3 Recommendations for further study

The magnetic recording density keeps growing and the size of magnetic hard disk drives keeps getting smaller. These pose extremely high magnetic recording areal density and track density and thus more stringent requirements to the dynamics and reliability of disk drive track access system. The dual-stage head position control using piezoelectric actuators is being utilized in commercial hard disk drives. Besides the continuous efforts in increasing the servo control bandwidth by improving the mechanical structure and control schemes, the identification of the other TMR (track-misregistration) sources, such as flow induced vibration of head actuator assembly, disk vibration and the reduction will still be the popular research topics in magnetic recording servo mechanical systems.

Thermal management of micro hard drives will be the hot topic with the wide application of small form hard disk drives. The application of piezoelectric micro

actuator in micro drives will boost the research of the lifecycles of piezoelectric actuators. Though the present study has addressed the reliability issues using the probability approach to take account of the effects of driving voltage and temperature, the case study presented in this research describes only this kind of multi-layer piezoelectric actuators. For other types of piezoelectric actuators utilized in disk drive head positioning system or the other devices, more fundamental study on the life cycles degradation mechanism could be explored.

The present study on the reliability of piezoelectric actuators proposed a probability model to evaluate the reliability of piezoelectric actuators. The model has a general application scope in mechatronics devices. With this research, it is believed the probability methods and statistical tools can be incorporated with engineering principles in reliability evaluation, failure analysis and quality control for mechatronics devices.

REFERENCES

1. **Abrahamson, S.D., Eaton, J.K., and Koga, D.J. (1989),** "The flow between shrouded corotating disks, "Phys. Fluids A, Vol. 1, No. 2, pp. 241-251.

2. **Adley, J., Jones, M., Stole, S., Perettie, D., and Fox, R. (1998),** "Design and material synergy for high-performance actuator components" 9th International Symposium on Information Storage and Processing Systems, Vol. 4, pp. 1-7.

3. **Aruga, K., Kuroba Y., Koganezawa S., Yamada T., Nagasawa Y., and Komura Y. (1996)**, "High-speed orthogonal power effective actuator for recording at over 10,000 TPI", IEEE Transactions on Magnetics, Vol. 32, No. 3, pp. 1756-1761.

4. **Arya, S. ; Lee, Y.S., Lu, W.M., Staudenmann, M., and Hatchett, M. (2001),** "Piezo-based milliactuator on a partially etched suspension", IEEE Transactions on Magnetics, Vol. 37, No. 2, pp. 934-939.

5. **Bittner H., and Shen, I.Y. (1999),** "Taming disk/spindle vibrations through aerodynamic bearings and acoustically tuned-mass dampers," IEEE Transactions on Magnetic, Vol. 35, no. 2, pp. 827-832.

6. **Budinger, M., Rouchon, J.F., and Nogarede, B. (2004),** "Analytical modeling for the design of a piezoelectric rotating-mode motor", IEEE-ASME Transactions on Mechatronics 9(1), pp.1-9.

7. **Carter, A.D.S. (1997),** "Mechanical Reliability and Design", Macmillan Press Ltd.

8. **Chainer, T.J., Sohn, W.J., and Sri-Jayantha, M. (1991),** "A flexural in-line actuator for magnetic recording disk drives", IEEE Transactions on Magnetics, Vol. 27, No. 6, pp. 5295-5297.

9. **Chang, C.J., Humphrey, J.A.C., and Greif, R. (1990),** "Calculation of turbulent convection between corotating disks in axisymmetric enclosures," Int. J. Heat Mass Transfer, vol. 33, no. 12, pp. 2701-2719.

10. **Chen, F., Xie, H., Fedder, G.K. (2001),** "A MEMS-based monolithic electrostatic microactuator for ultra-low magnetic disk head fly height control", IEEE Transactions on Magnetics, Vol. 37, No. 4, Part 1, pp.1915-1918.

11. **Chen, S.X., Li, Q.H., Mah, Y., Mannan, M., Ong E.H., Zheng, H., and Weerasooriya, S., and Wood, R. (1997),** " A High-Bandwidth Moving Magnets Actuator for Hard Disk drives", IEEE Transactions on Magnetics, Vol. 33, No. 5, pp. 2632-2634.

12. **Dausch, D.E., and Hooker, M.W. (1997),** "Low-field and high-field fatigue in PZT-based rainbow actuators", Journal of Intelligent Material Systems and Structures, 8 (12), pp. 1044-1051.

13. **Dahl, P. R. (1968), "**A solid friction model", Technical report Tor-158, Aerospace Corporation, El Segundo, CA. USA.

14. **Eddy, K., Steele, J., and Messner, W. (1997),** "Bias in Disk Drive Rotary Actuators: Characterization, Prediction, and Compensation", IEEE Transactions on Magnetics, Vol. 33, pp. 2424-2436.

15. **Fan L.S. (1996),** "Design and Fabrication of microactuator for high density data storage", IEEE Transactions on Magnetics, Vol. 32, No. 3, pp. 1855-1862.

16. **Fan, L.S., Ottesen, H.H., Reiley, T.C., and Wood, R. (1995),** "Magnetic Recording Head Positioning at Very High Track Densities Using a Microactuator-based Two-Stage Servo Systems", IEEE Transactions on Industrial Electronics, Vol. 42. No. 3, pp. 222-233.

17. **Fan, L.S. et al., (1999),** "Electrostatic microactuator and design considerations for HDD applications", IEEE Transactions on Magnetics, Volume 35, Issue 2, pp.1000-1005.

18. **Fu, H. and Gao, Z.T. (1985),** "Probability density function of fatigue strength", Proceedings of the international conference on structural safety and reliability, Kobe, Japan, pp. 765-774.

19. **Gao, Z. T., (1986),** Applied Fatigue Statistics, National Defense Industry Press (in Chinese).

20. **Girard, J., Abrahamson, S., and Uznanski, K. (1995),** "The effect of rotary arms on corotating disk flow," Journal of Fluids Engineering, Vol. 117, pp. 259-262.

21. **Gope, P.C. (1999),** "Determination of sample size for estimation of fatigue life by using Weibull or Log-normal distribution", International Journal of Fatigue, (21), pp. 745-752.

22. **Guo, G.X., Hao, Q. and Low, T.S. (2001),** "A Dual Stage Control Design for High Track Per Inch Hard Disk Drives", IEEE Transactions on Magnetics, Vol. 37, No. 2, pp. 860-865.

23. **Guo, W., Weerasooriya, S., Goh, T.B., Li, Q.H., Bi, C., Chang, K.T., and Low, T.S. (1998),** "Dual Stage Actuators for high density rotating memory devices", IEEE Transactions on Magnetics, Vol. 34, No. 2, pp. 450-455.

24. **He, Z.M., Guo, W., Li, Q.H., Ong, E.H., and Huang, T. (1999),** "Finite element simulation and optimization of piezoelectric suspensions", Proc. of SPIE Smart Structures and Materials, Vol. 3668, pp. 1036-1043.

25. **He, Z.M., Ong, E.H., and Guo, G.X. (2001),** "Design of a Magnetic Disk Drive Actuator with Small Skew Actuation", Abstract of 46th Conference on Magnetism and Magnetic Materials, Seattle, Washington, November 12-16, pp. 363.

26. **He, Z.M., Ong, E.H., and Guo, G.X., (2002),** "Optimization of a magnetic disk drive actuator with small skew actuation", Journal of Applied Physics, AIP, Vol. 91, No. 10, pp. 8709-8711.

27. **He, Z.M., Qian, H. Wu, D.W., Wang W.L., Liu, X., and Liu, J. C. (2003),** "Design of flexural pivot for use in hard disc drive actuator", Journal of Microsystem Technologies, Vol. 9, No. 6-7, pp. 453-460.

28. **He Z.M., Guo G.X., Feng L., and Wong W.E. (2003),** "Head carrying cartridge with micro actuation for high density magnetic recording", Proc. of Second International conference on Computational Intelligence, Robotics and Autonomous Systems, 16-18 Dec., Singapore, PS05-3.

29. **He, Z.M., Loh, H.T., and Ong, E.H. (2005),** "A probability approach to evaluating the reliability of piezoelectric micro-actuators", IEEE Transactions on Reliability, Vol. 54, No. 1, 2005, pp. 83-91.

30. **He, Z.M., Loh, H.T., and Xie, M. (2007),** "A two-dimensional probability model to evaluate the reliability of piezoelectric micro-actuators", International Journal of Fatigue, Vol. 29, No. 2, pp. 245-253.

31. **Health, J.S., (2000),** "Boosting servo bandwidth", Proc. Of Asia-Pacific magnetic Recording Conference, APMRC, MP 20/1-MP 20/2, Japan.

32. **Hirano, T. et al., (1999),** "High bandwidth HDD tracking servo by a moving-slider micro-actuator", IEEE Transactions on Magnetics, Vol. 35, No. 5, pp. 3670-3672.

33. **Hirose, H. (1996),** "Maximum likelihood estimation in the 3-parameter Weibull distribution. A look through the generalized extreme-value distribution", IEEE Transactions on Dielectrics and Electrical Insulation, Vol. 3, No. 1, pp. 43 – 55.

34. **Horsley, D.A., Wongkomet, N., Horowitz, R. and Pisano, A.P. (1999),** "Precision positioning using a microfabricated electrostatic actuator, IEEE Transactions on Magnetics, Vol. 35, No. 2, pp. 993-999.

35. **Hu, S.B., Liu, B., and Low, T.S., (1997),** "Skew angle and read/write off-track asymmetry of MR heads", IEEE Transactions on Magnetics, Vol. 33, No. 5, pp. 2695-2697.

36. **Huang, F-Y, Semba, T., Imaino, W., and Lee, F. (2001),** "Active damping in hard disk drive actuator", IEEE Transactions on Magnetics, Vol. 37, No. 2, pp. 847-849.

37. **Huang, Y.H., Banther, M., Mathur, P.D., and Messner, W.C. (1999),** "Design and analysis of a high bandwidth disk drive servo system using an instrumented suspension", IEEE/ASME Transactions on Mechatronics, Vol. 4, No. 2, pp. 196-206.

38. **Hughes, G.F., Murray, J.F., Kenneth, K.D., and Elkan, C.,** "Improved disk-drive failure warnings", IEEE Transactions on Magnetics, Vol. 51, No. 3, 2002, pp. 350-357.

39. **Hurst, T., and Henze, D. (1997),** "Understand ball bearing pre-rolling behavior using the restoring force surface method", Adv. Info. Storage Syst. 7, pp. 269-279.

40. **Hutchinson Technology Inc. (1995),** Suspension Product Summary-Type 850.

41. **IBM storage products**, www.ibm.com/harddrive.

42. **Imai, S., Mori, K., and Okazaki, T. (1997),** "Flutter reduction by centrifugal airflow for high-rotation-speed disks," Proc. International Conference on Micromechatronics for Information and Precision Equipment, Tokyo, pp. 32-37.

43. **Jayson, E.M.,; Smith, P.W., Talke, F.E., (2003a),** "Shock modeling of the head-media interface in an operational hard disk drive", IEEE Transactions on Magnetics, Vol. 39, No. 5, pp. 2429-2431.

44. **Jayson, E.M., Murphy, J., Smith, P.W., Talke, F.E. (2003b),** "Effects of air bearing stiffness on a hard disk drive subject to shock and vibration", Transactions of the ASME. Journal of Tribology, Vol. 125, Issue 2, pp. 343-349.

45. **Jeans, A.H. (1992),** "Analysis of the dynamics of a type 4 suspension", Transactions of the ASME, Journal of Vibration and Acoustics, Vol. 114, pp. 74-78.

46. **Kim B.H., and Chun, K. (2001),** "Fabrication of an electrostatic track-following microactuator for hard disk drives using SOI wafer", Journal of Micromechanics and Microengineering, Vol.11, No. 1, pp. 1-6.

47. **Koganezawa, S., Takaishi, K., Mizoshita, Y., Uematsu, Y., Yamada, T., Hasegawa, S., and Ueno T. (1996),** "A flexural piggyback milli-actuator for over 100 Gbit/in^2 density magnetic recording", IEEE Transactions on Magnetics. Vol. 32, No. 5, pp. 3908-3910.

48. **Kryder, M.H., and Gustafson, R.W. (2004),** "High-density perpendicular recording-advances, issues, and extensibility", Journal of magnetism and Magnetic Materials, in press.

49. **Kuwajima, H., Uchiyama, H., Ogawa, Y., and Kita, H. (2002),** "Manufacturing process of piezoelectric thin-film dual-stage actuator and its reliability for HDD", IEEE Transactions on Magnetics, 38 (5), pp. 2156-2158

50. **Lambert, S.E., Lairson, B.M., Nguy, H., Nguyen, L., and Huang, T. (2001),** "Driving integration challenges for perpendicular recording", Journal of Magnetism and Magnetic Materials, (253), pp. 245-252.

51. **Lampman, S. (1989)** "Fatigue and fracture properties of stainless steels", ASM Handbook, pp.712-731.

52. **Lee, S.J., Hong, S.K., and Lee, J.M. (2001),** "Study of Shock-Resistance Design of Suspension Subjected to Impulsive Excitation", IEEE Transactions on Magnetics, Vol. 37, No. 2, pp. 826-830.

53. **Li, Q. (1997),** "Analysis of the dynamics of 3.5" hard disk drive actuators", Technical Report, Data Storage Institute.

54. **Li, Q., Weerasooriya, S., and Low, T.S. (1999),** "Finite element analysis of the dynamics of a high bandwidth actuator for a hard disk drive", The International Journal for Computation and Mathematics in Electrical and Electronics Engineering, Volume 18, No. 2, pp.120-131.

55. **Li, Y. M. (1994),** "General linear-regression analysis applied to the 3-parameter Weibull distribution IEEE Transactions on Reliability, Vol. 43, No. 2, pp. 255-263.

56. **Liang L., and Miles R.N., (1999),** "A passive damping for the vibration modes of the head actuator in hard disk drives", Journal of sound and Vibration, 220 (4), pp. 683-694.

57. **Lin, H., Li. Q.H., He, Z.M., and Chen, S.X. (2001),** "Development of a single coil coupled force VCM actuator for high TPI magnetic recording", IEEE Transactions on Magnetics, Vol. 37, No. 2, pp. 850-854.

58. **Liu, B. and Soh, S.H. (1996),** "Effects of seeking velocity on air bearing skew angle, air flow speed and flying performance of sliders with different ABS designs", IEEE Transactions on Magnetics, Vol. 32, No. 5, pp. 3693-3695.

59. **Liu, X. and Liu, J.C. (2000),** "Analysis of Pivot Bearing Friction torque for High Density Drive Applications", J. Info. Storage Proc. Syst., Vol. 2, pp. 41-46.

60. **Low, T.S. (1998)**, "magnetic Recording Beyond 10 Gigabits Per Square Inch-The Challenges in the Mechatronics", Professional Lectures for Technology Month 98, National University of Singapore, pp. 45-75.

61. **Mah, Y.A., Lin, H., Li, Q.H., and Chen, S.X. (1999),** "Design of A High Bandwidth Moving Coil Actuator with Force Couple Actuation", IEEE Trans. Magn., Vol. 35, No. 2, pp. 874-878.

62. **Mall, S. and Hsu, T.L. (2000),** "Electromechanical fatigue behavior of graphite/epoxy laminate embedded with piezoelectric actuator", Smart Materials and Structures, 9 (1), pp. 78-84.

63. **Mitrovic, M. ; Carman, G.P.; Straub, F.K. (2000)** "Durability properties of piezoelectric stack actuators under combined electro-mechanical loading", Proceedings of the SPIE – The International Society for Optical Engineering, Vol. 3992, pp. 217-232.

64. **Montgomery, D.C. (2003),** Applied Statistics and Probability for Engineers, Third Edition, John Wiley & Son, Inc.

65. **Mori, K., Munemoto, T., Otsuki, H., Yamaguchi, Y., and Akagi, K. (1991),** "A dual –stage magnetic disk drive actuator using a piezoelectric device for a high track density", IEEE Transactions on Magnetics, Vol. 27, pp. 5298-5300.

66. **Morita, T. (2003),** "Miniature piezoelectric motors", Sensors and Actuators A 103, pp. 291-300.

67. **Nakamura, S., Naniwa, I., Sato, K., Yasuna, K., and Saegusa, S. (2001),** "Life prediction method for piggyback PZT actuator", IEEE Transactions on Magnetics, 37 (2), pp. 940-943.

68. **Nakamura, S., Numasato, H., Sato, K., Kobayashi, M., and Naniwa, I. (2002),** "A push-pull multi-layer piggy PZT actuator", Microsystem Technologies, 8, pp. 149-154.

69. **Ni, K., and Mahadevan, S. (2004),** "Strain-based probabilistic fatigue life prediction of spot-welded joints", International Journal of Fatigue, 26, pp. 763-772.

70. **Niu, Y., Guo, W., Guo, G.X., Ong, E.H., Sivadasan, K.K., and Huang, T. (2000),** "A PZT Micro-Actuated Suspension for High TPI hard Disk Servo Systems", IEEE Transactions on Magnetics, Vol. 36, No. 5, pp. 2241-2243.

71. **Ong, E.H., He, Z.M., Chen, R.F., Qian, H., and Guo, G.X. (2000),** "A Low-Turbulence-High-Bandwidth Actuator for 3.5" Hard Disk Drives", IEEE Transactions on Magnetics, Vol. 36, No. 5, pp. 2235-2237.

72. **Prater, W. (1995),** "Ball bearing design influence on disc drive track mis-registration", Adv. Info. Proc. Syst., ASME, pp. 213-220.

73. **Pritchard, J., Bowen, C.R., Lowrie, F. (2001),** "Multilayer actuators: review", British Ceramic Transactions, Vol. 100, No. 6, pp. 265-273.

74. **Ratliff, R.T., Pagilla, P.R., (2004),** "Design and seek control of a disc drive actuator with nonlinear magnetic bias", Proceedings - 2004 IEEE International Conference on Robotics and Automation; Vol. 2004, No. 4, pp. 3640-3646.

75. **Reddy, J.N. (1999),** "Theory and Analysis of Elastic Plates", Philadelphia, Pa.: Taylor & Francis.

76. **Schmid, U. (1997),** "Percentile estimators for the three-parameter Weibull distribution for use when all parameters are unknown", Communications in Statistics Theory and Methods, Vol. 26, No. 3, pp. 765-785.

77. **Schuler, C.A., Usry, W., Weber, B., Humphrey, J.A.C., and Greif, R. (1991),** "On the flow in the unobstructed space between shrouded corotating disks," Phys. Fluids A, Vol. 2, no. 10, pp. 1760-1770.

78. **Shi, P., and Mahadevan, S. (2003),** "Corrosion fatigue and multiple site damage reliability analysis", International Journal of Fatigue, (25), pp. 457-469.

79. **Sobczyk K, and Spencer, J.B.F. (1992),** "Random Fatigue: from data to theory", Academic Press, Inc.

80. **Sri-Jayantha, M., Chainer T. J., and Brown, D.H. (1991),** "Digital servo control of a Novel Disk Actuator", IEEE Transactions on Magnetics, Vol. 27, No. 6, pp. 4476-4483.

81. **Takaishi, K., Imamura, T., Mizoshita, Y., Hasegawa, S., Uneo, T., and Yamada, T. (1996),** "Microactuator Control for disk Drive", IEEE Transactions on Magnetics, Vol. 32, pp.1863-1866.

82. **Temesvary, V., Wu, S., Hsieh, W.H., Tai, Y.C., and Miu, D.K. (1995),** "Design, fabrication, and testing of silicon microgimbals for super-compact rigid disk drives", J. of Micro-electromechanical System. Vol. 4, No. 1, pp. 18-27.

83. **Thongrueng, J. et al (1998),** "Lifetime and degradation mechanism of multilayer ceramic actuator", Jpn. J Appl. Phys. 37, pp. 5306-5310.

84. **Tokuyama, M. et al (2001),** "Development of a Φ-shaped actuated suspension for 100-kTPI hard disk drives", IEEE Transactions on Magnetics, Vol. 37, No. 4, Part 1, pp. 1884-1886.

85. **Tzeng, H.M., and Munce, A.C. (1991),** "Flows between shrouded corotating disks with radial and oblique obstructions," IBM Research Report, RJ7523.

86. **Uchino, K. (1998),** "Materials issues in design and performance of piezoelectric actuators: an overview", Acta mater. 46 (11), pp. 3745-3753.

87. **US Patent 6, 021,024, Feb. 1 (2000).**

88. **Usry, W.R., Schuler, C.A., Humphrey, J.A.C., and Greif, R. (1990),** "Unsteady flow between corotaitng disks in an enclosure with an obstruction," Proc. 5th Int. Symp. On Application of Laser Techniques to fluid Mechanics, Lisbon, Portugal.

89. **Wang, D., Carman, G.P. (1998),** "Combined electrical and mechanical fatigue of piezoelectric ceramics undergoing polarization switching for large displacement actuation", Proceedings of the SPIE - The International Society for Optical Engineering, Vol. 3329, Part 1-2, 1998, pp. 210-221.

90. **Wang Z.H. (1997),** "Split Electrode In-plane Bending Piezoelectric Actuator (IV)-Dynamics Response", Technical Report of Electronic Materials Research Laboratory, Xi'an Jiaotong University.

91. **Wang, Z., Zhu, W., Zhao, C.; and Yao, X. (2001),** "Deflection characteristics of a trapezoidal multilayer in-plane bending piezoelectric actuator, IEEE Transactions on Ultrasonics, Ferroelectrics, and Frequency Control, Vol. 48, No. 4, pp. 1103-1110.

92. **Watanabe, T., Ohwe, T., Yoneoka, S., and Mizoshita, Y. (1997),** "An Optimization Method for Precision Positioning of Pico-CAPS", IEEE Transactions on Magnetics, Vol. 32, No. 5, pp. 2644-2646.

93. **Wei D., and Liu, B., (1997),** "Track edge Asymmetry and Low-Density Noise in Thin Film Disk Media with Skew Angles", IEEE Transactions on Magnetics, 33(5), 2722.

94. **Wei, D., He, L.N., and Liu, B., (1998),** "Isolated pulse distortion and medium noise analysis for submicrometer-width narrow-track recording" IEEE transactions on Magnetics, Vol. 34, No. 5, pp. 3794-3798.

95. **Wiesen, K., Lansky, R.M., and Sobey, C. (1993), "**Recording asymmetries at large skew angles", IEEE Transactions on Magnetics, Vol. 29, No. 6, pp. 4002-4004.

96. **Wood, R. (2000),** "The Feasibility of Magnetic Recording at 1 Terabit Per Square Inch", IEEE Transactions on Magnetics, Vol. 36, No. 1, pp. 36-42.

97. **Wood, R. (2001),** International conference on Materials for Advanced Technology, Singapore, pp. 165.

98. **Xie, M., Goh, T.N., and Tang, Y. (2004),** "On changing points of mean residual life and failure rate function for some generalized Weibull distributions", Reliability Engineering and System Safety (84), pp. 293-299.

99. **Xu, L.M., and Guo, N. (2003), "Modal testing and finite element modeling of subsystem in hard disk drive",** Mechanical Systems and Signal Processing, 17(4), pp. 747-764.

100. **Yamaguchi, T., and Nakagawa, S. (2000),** "Recent Control technologies for Fast & precise Servo System of Hard Disk Drives", Proceedings of 6th International Workshop on Advanced Motion control, Nagoya, Japan, pp. 69-73.

101. **Yoshikawa, S. and Farrell, M. (2000),** "Actuator environmental stability", Proc. of SPIE Smart Structures and Materials, 3985, pp. 652-659.

102. **Zeng, S., Xu, L.M., and Lin, R.M. (2000),** "Dynamics Improvement of the Head Actuator Assembly in Hard Disk Drives with Passive Damping", Journal of Information Storage and Processing Systems, Vol. 2, pp. 303-306.

APPENDICES

A1. Matlab program for optimizing the actuator arm length and calculation the skew angle

```
% calculates skew angle

%Given oa, ob fixed,
%the actual angle is alpha+90, then we have oa^2 = ab^2+ob^2
+2*ab*ob*cos(alpha+90)

clear; close all

% data measured from data storage magazine march 2001, page 11, not a
real drive.\

oa =57.8,
ob0=51;
id=16.5;
od=47;

oa =57.8,
ob0=51;
id=16.5;
od=47;


aba=[];
skewangle=[]
bendangle=[];

for jj=1:30;

  ob=ob0+ id*1.0*jj/30; % extended length from 4.7 to another 2/3 of id length
  oba(jj)=ob;
  l_ratio(jj)=ob/oa;

  alpha=[];
        ab=[];

        for ii=1:40;

          ab(ii)=id+ii*(od-id)/40;
        alpha(ii) = acos((-oa^2+ab(ii)^2+ob^2)/(2*ab(ii)*ob))*180/pi-90;

        end

        figure(jj)
```

```
        plot(ab, alpha);

        skewangle(jj)=max(alpha)-min(alpha);
  %bendangle(jj)=mean(alpha);

        S = sprintf('Max skew angle variation is %4.1f deg.',skewangle(jj));

        xlabel('distance to spindle center in cm')
        ylabel('skew angle in degree')
        title(S)
end

figure(jj+1)
plot(oba, skewangle, 'r-', ...
  oba, skewangle, 'x');
xlabel('length of actuator in cm')
ylabel('skew angle range x')

figure(jj+2)
plot(l_ratio, skewangle, 'r-', ...
  l_ratio, skewangle, 'o');
xlabel('length ratio of actuator arm to the distance between pivot to spindle
center')
ylabel('skew angle range o')

disp('actuator length increased to ')
max(oba)/min(oba)

disp('skew angle reduced to')
min(skewangle)/max(skewangle)


% calculates skew angle and band angle
clear; close all

L1=64.3,  %L1 is the optimized arm length (from pivot center to head)
Ls=18.05; % suspension length
D1=57.8   % distance from pivot center to spindle center
id=16.5   % inner radius of disk
od=47     % outer radius of disk

alpha=[]  % initially determined skew angle at a particular position
Larm=[]   % initailly determined arm length (from pivot to ball swaging center)
temp=1:30; % defined array to skew angle change

alpha=acos(D1/L1)*180/pi
Larm=sqrt(L1^2+Ls^2-2*L1*Ls*cos(alpha*pi/180))

bendangle=[]
skewchange=[];
```

```
for jj=1:30

  bendangle(jj)=45*jj/30; % peta is the slant angle, change from 1 to 45 in
degree
  bendangle1(jj)=180-bendangle(jj)
  LL(jj)=sqrt(Larm^2+Ls^2-2*Larm*Ls*cos(bendangle1(jj)*pi/180))    %distance
from pivot center to head after the suspension bent

E=[];         %distance from head to spindle center
skewchange=[]; %skew angle range at a particular bend angle

  for ii=1:40

      E(ii)=id+ii*(od-id)/40;
      peta1(ii)=acos((LL(jj)^2+E(ii)^2-D1^2)/2/LL(jj)/E(ii))*180/pi;
      peta2(ii)=90-peta1(ii);

      skewangle(ii)=acos((Ls^2+LL(jj)^2-Larm^2)/2/LL(jj)/Ls)*180/pi-peta2(ii);

      end

figure(jj)
plot(E, skewangle);

skewchange(jj)=max(skewangle)-min(skewangle);

S = sprintf('Max skew angle variation is %4.1f deg.',skewchange(jj));
temp(jj)= skewchange(jj);
xlabel('distance to spindle center in mm')
ylabel('skew angle in degree')
title(S)
end

figure(jj+1)


  plot(bendangle, temp, 'r-',...
    bendangle, temp, 'o');

xlabel('suspension slant angle in deg')
ylabel('skew angle change in deg.')
```

A2. Matlab program for plotting the response responses of an actuator

```
load zero-slant;
YY10     = o2i1;
X_Bgn10  = o2i1x0;
X_End10  = X_Bgn10 * exp(log(o2i1xl)*(length(YY10)-1));
XX10     = logspace(log10(X_Bgn10),log10(X_End10),length(YY10))';

phase10 = (angle(YY10))*180/pi;
mag10   = 20*log10(abs(YY10));

load zero-unslnat;
YY20     = o2i1;
X_Bgn20  = o2i1x0;
X_End20  = X_Bgn20 * exp(log(o2i1xl)*(length(YY20)-1));
XX20     = logspace(log10(X_Bgn20),log10(X_End20),length(YY20))*0.99;

phase20 = (angle(YY20))*180/pi;
mag20   = 20*log10(abs(YY20));

%X_End10 = 1.e4;

figure(1);
clf;
subplot(211);
semilogx(XX10, phase10, '-',XX20, phase20, '--');%semilogx(XX20, phase20,
'r-');
axis([X_Bgn10,                X_End10,                floor(min(phase10)/10)*10,
ceil(max(phase10)/10)*10]);
%axis([X_Bgn10, X_End10, -180, 180]);
grid on;
ylabel('Phase (deg)');

subplot(212);
semilogx(XX10,mag10, 'k-'); hold on;
semilogx(XX20,mag20, 'k--'); hold off;
axis([X_Bgn10, X_End10, floor(min(mag10)/10)*10, ceil(max(mag10)/10)*10]);
grid on;
ylabel('Mag (dB)');
xlabel('Frequency (Hz)');

break;
```

A3. Derivation of the equivalence of the probability distributions between the electric strength and lifetime

Referred in Figure 6.3, we assume that (N_0, E_0) is an arbitrary point in the *E-N* curve. Let the event A (EA) stands for the assembly of that the lifetime is less than N_0, at a specified electric strength, E_0, then the probability of that the event A occurs is written as:

$$P(EA) = P(N_{\min} < N < N_0) \tag{A.1}$$

where, $N_{\min}$ is the minimum lifetime. Similarly, let the event B (EB) stands for the assembly of that of the electric strength is less than E_0, at a specified lifetime N_0, then the probability of event B occurring is as:

$$P(EB) = P(E_{\min} < E < E_0) \tag{A.2}$$

where $E_{\min}$ is the minimum electric strength. In the assembly A, every individual *N* should be less than N_0, at the specified electric load E_0. According to a basic principle for material failure, under the same conditions, a lower electric load level corresponds to a higher lifetime, and vice versa. Therefore, if we increase the all the lifetime in assembly A to the number N_0, the electric load level should be reduced to below E_0. Hence, we can think the event A is a sub-assembly of event B. The occurrence of event A will result in the occurrence of B. Therefore, we have

$$EB \supseteq EA \tag{A.3}$$

$$P(EB) \geq P(EA) \tag{A.4}$$

In the other side, in the assembly B, every individual electric strength E should be less than E_0, at the specified lifetime, N_0. Therefore, under E_0, all the lifetime should be lower than N_0. Hence, the assembly B can be taken as a sub-assembly of A. We have,

$$EB \subseteq EA \tag{A.5}$$

$$P(EB) \leq P(EA) \tag{A.6}$$

Compare equations (A.4) and (A.6), we have

$$P(EA) = P(EB) \tag{A.7}$$

Therefore,

$$P(N_{\min} < N < N_0) = P(E_{\min} < E < E_0) \tag{A.8}$$

$$\int_{N_{\min}}^{N_0} f(N|E_0)dN = \int_{E_{\min}}^{E_0} g(E|N_0)dE \tag{A.9}$$

Using any point (N, E) to replace (N_0, E_0), we obtained,

$$\int_{N_{\min}}^{N} f(N|E)dN = \int_{E_{\min}}^{E} g(E|N)dE \tag{A.10}$$

A4. Matlab program for plotting the electric load signals, curve fitting, and reliability computation

```
% This program is used for plotting the input voltage signals of a piezoelectric
micro actuators

clear all,
load pzt01.mat;    %pzt micro actuator imput voltage during the track following
yy=c1(263:512);    %512 points, 263 corresponds to zero point
xx=c1(263:-1:1);   %before 263, the value is negative, we want to flip it.
yy=[yy; zeros(13,1)]; %?
zz=xx+yy;          %?flip it
cof=22.588/512;

S = sum(zz*cof); %normalize to the real voltage unit
xx1=[0:cof:262*cof]';
zz2=zz/S;       %normalize to probability density

plot(xx1, zz2);

aa_c = 0;
   for aa = 1:0.1:3,
      aa_c = aa_c + 1;
      bb_c = 0;
      for bb=0.5:0.5:10,
         bb_c = bb_c + 1;
         zz4 = (aa/bb)*((xx1/bb).^(aa-1)).*exp(-(xx1./bb).^aa);
         qq(aa_c, bb_c) = sum((zz4-zz2).^2);
         disp(['aa = ' num2str(aa) ', ' 'bb = ' num2str(bb)]);
      end
   end

%plot3(aa, bb, qq);


% program for curve fitting of electric input voltage
aa=2.019;
bb=2.67;
cof=22.588/512;
xx1=[0:cof:262*cof]';
zz4 = (aa/bb)*((xx1/bb).^(aa-1)).*exp(-(xx1./bb).^aa);
plot(xx1, zz4, 'k');
%plot(xx1, zz4, 'r');


% probability plot of electric strength
x=[0.1:0.1:20];
for i=1:1:200
a(i)=-(13.9667*LOG10(x(i))-13.4638)^2/(2*0.5911^2);
```

```
y(i)=(4.0970/x(i))*exp(a(i));
end
plot(x,y)


% compute reliability and plot of reliability versus lifetime (one dimensional
model)
clear all;
for xx=5:1:13;
   tt=10^xx;
   aa=1;
   bb=20;
   ff1=inline('-10.2617/sqrt(2*pi)/ee');
   ff2=inline('exp(-(log10(tt)-21.4638+13.9667*log10(ee))/(2*0.5911^2))');
   ff3=inline('exp(-(ee/2.67)^2.019)');
   ff4=inline('ff1*ff2*ff3');
   qq = quad(ff4,1,20);
   rr=1-qq;
end
plot(tt, rr);
```

PUBLICLICATIONS RELATED TO THIS THESIS

Publications:

1. He Zhimin, Loh Han Tong, and Xie Min, "A two-dimensional probability model to evaluate the reliability of piezoelectric micro actuators", International Journal of Fatigue, Vol. 29, No. 2, 2007, pp. 245-253.

2. He Zhimin, Loh Han Tong, and Ong Eng Hong, "A probability model to evaluate the reliability of piezoelectric micro actuators", IEEE Transactions on Reliability, Vol. 54, No. 1, 2005, pp. 83-91.

3. He Zhimin, Loh Han Tong, Xie Min and Guo Guoxiao, "A reliability model for piezoelectric micro-actuators", International Power Engineering Conference, 29 November-2 December 2005, Singapore.

4. He Zhimin et al., "Design of Flexural Pivot for Use in Hard Disc Drive Actuator", Journal of Microsystem Technologies, Vol. 9, No. 6-7, 2003. pp. 453~460.

5. He Zhimin, Ong Eng Hong, and Guo. Guo, "Optimization of a magnetic disk drive actuator with small skew actuation," Journal of Applied Physics, American Institute of Physics, Vol. 91, No. 10, 2002, pp. 8709-8711.

6. Huai Lin, Qinghua Li, Zhimin He, and Shixin Chen, "Development of a Single Coil Coupled Forced VCM Actuator for High TPI Magnetic Recording", IEEE Transactions on Magnetics, Vol. 37. No. 2, 2001, pp. 850-854.

Patents:

1. He Zhimin; Guo Guoxiao; Qian Hua; and Ong Eng Hong; "Flexural pivot for rotary disk actuator", US patent, 6,963472 B2, November 8, 2005.

2. Lin Huai, Low Teck Seng, Zhimin He, Chen, Shixin and Li, Qinghua, "An actuator assembly for orthogonal force generation", US patent 6,633,457 B2 25 July 2003.